UNIVERSITY
of York

Raman Spectroscopy as a Diagnostic Method for Prostate Cancer Cell Lines on a Graphene Substrate.

Author:
Lucy Elizabeth Faulkner

Supervisor:
Dr. Y. Hancock

ABSTRACT

Raman Spectroscopy is an technique that can characterize samples using a non-invasive, label-free method. It has revolutionized the scientific research field identifying everything from pharmaceuticals, geology, and even biological applications. These biological applications include a deeper understanding of bone structure, drug and cell interactions and even advancements in the field of cancer diagnostics. This thesis uses this pioneering technique to first characterise graphene sheets that have been obtained through chemical vapour desposition. Raman interactions can achieve a fingerprint signal, allowing a greater understanding of graphene's defects and composition. Using the peak's locations, full width at half maximum and intensity ratios will allow a comparison to literature, and lead to an in-depth understanding of the quality of graphene. Secondly, characterisation of the prostate cancer cell line P4E6 will be completed. Various statistical analyses are performed to understand the prostate cell line's interactions with graphene and the potential biological applications of graphene.

DECLARATION

I declare that this thesis is a presentation of original work and I am the sole author. This work has not previously been presented for an award at this, or any other, University. All sources are acknowledged as References.

Contents

1 Introduction

1.1 Graphene

1.1.1 Properties of Graphene

Graphene is a singular layer of graphite which consists of a honeycomb lattice of carbon atoms, in a flat monolayer [1]. It is two-dimensional, and is the base material of fullerenes or rolled into 1D nanotubes. Graphite is the 3D stacked version of graphene. Graphene is its two-dimensional existence [1]. Graphene's structure is demonstrated in figure 1.
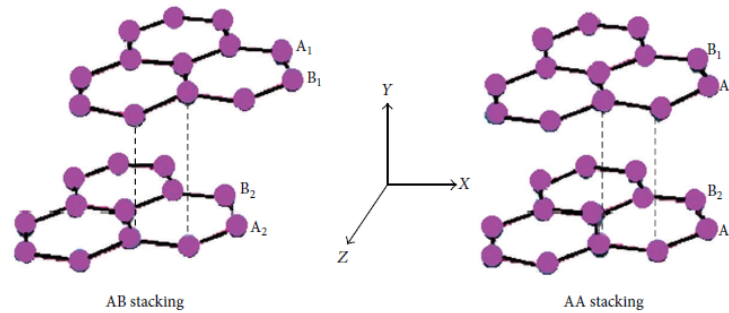

Figure 1: An image to represent the AB stacking of graphene layers (left) and AA stacking of graphene layers (right) [2].

Graphene is now used in many different areas of research due to its breakthrough isolated discovery in 2004 by Novoselov et. al [3], from industrial applications in solar cells [4] to biomedical research [5]. This is due to its unique structure and properties [3]. There are many methods in which to extract single layers of graphene, with the most popular choice being mechanical exfoliation of highly oriented pyrolytic graphite, which can be used to produce 5mm x 5mm x 1mm sized samples [6]. Although it is the most common, it is not useful in cases where a large area film is needed, such as materials in devices. This is because this method can only give a sample with dimensions on the millimetre scale.

Graphene can be produced on a larger scale of centimeters, via several different tech-

niques such as chemical vapour desposition [7, 8, 9], reduction of oxidized graphite oxide [10], and graphitization under high vacuum of SiC wafers [11]. This is easily available to purchase online [12].

1.1.2 Raman Spectroscopy of Graphene

The Raman spectroscopy profile of graphene has been researched largely by the science community since its 2004 discovery, with leaders in the field including Ferrari [13, 14] and Dresselhaus [15], who have contributed massively to the understanding of the structure and interactions that happen in graphene's complex system.

The Raman spectra of graphene can be used to understand the interactions involved within graphene, showing strain and unintentional doping in differences of peak position, width and peak intensity ratios (PIR) [16].

Graphene has two atoms of the unit cell that are inequivalent [13]. Single layer graphene is easily identified by its two common peaks known as the G peak, located at 1580cm^{-1} [16] and the G' peak located at 2700cm^{-1} [16].

The G-peak is responsible for in-plane scattering of zone centre phonons. This comes from the high frequency E_{2g} mode of the sp^2 rings and chains (figure 3(a)) [13]. It comes from the Raman fundamental selection rule, where the phonon has q = 0 and no disorder meaning energy conservation.

The G' peak is due to the 2nd order double resonance scattering [17]. It comes from the satisfaction of momentum conservation by two opposite wave vectors [13].

There is also another peak that can appear around 1350cm^{-1} [16], known as the D peak. The D peak arises from the defects in the graphene layer and is used to measure the quality of the graphene [16]. The D peak comes from the breathing modes of the six-atom rings [13]. It is due to the transverse optical phonons around the Brillouin zone corner K [13].

The D + D" band, referred to as G* band in this paper is a combination of a D phonon

and a phonon from the longitudinal acoustic branch from a defected sample that is measured with visible light.
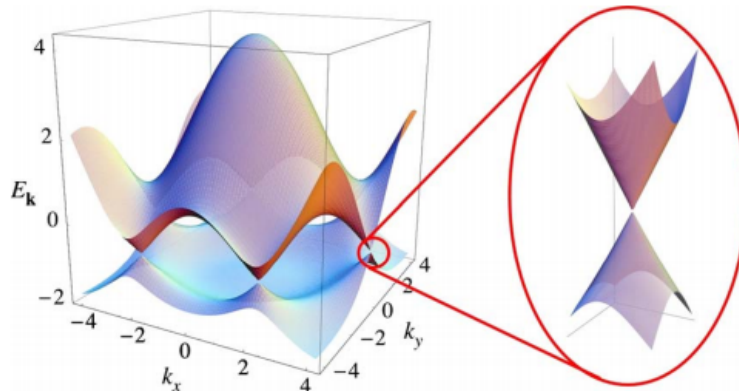

Figure 2: A figure to show electronic dispersion in the honeycomb lattice of graphene [18].

These peaks are due to graphene's unique electronic dispersion, which is shown in figure 2. This leads to the individual phonon processes which result in difference peaks, outlined in figure 3.

1.2 Prostate Cancer

1.2.1 Prostate Cancer and its Significance.

Cancer is a disease that causes abnormal cellular growth. It can spread to and damage other cells. Cancer comes from the mutation and damage of cells, as they are extremely fragile. Every cancer is caused by a different set of mutations. One of the best ways to improve mortality rates within cancer is early detection so that the cancer can be treated and managed in its earliest stages [19].

The prostate is a gland that sits between the bladder and urethra. The gland is responsible for producing fluid that washes and keeps sperm healthy. It can often have no symptoms but it can cause a change in a man's usual urinary patterns. Prostate
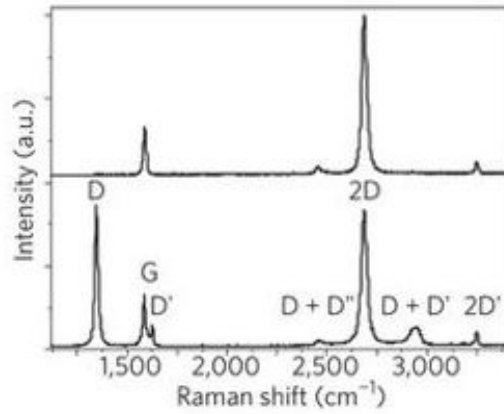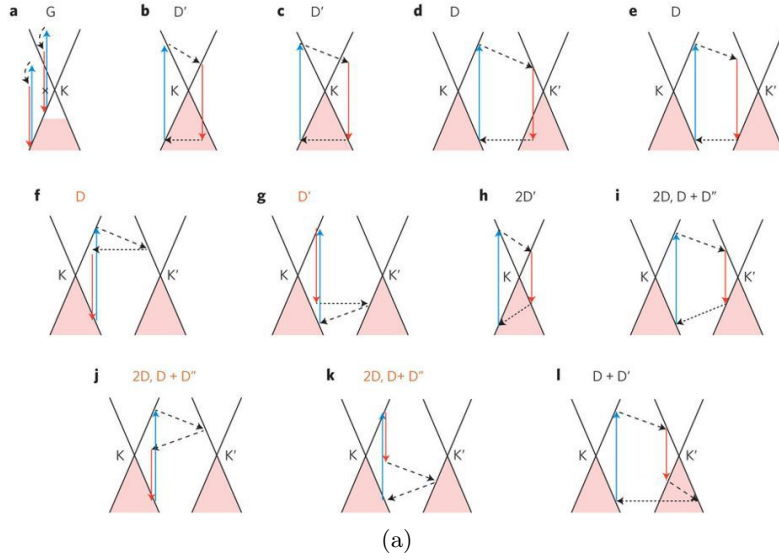
(a)

(b)

Figure 3: Figure (a) shows the phonon processes responsible for the relative peaks with electron dispersion as solid black lines, occupied states as the shaded areas, interband transitions neglecting the photon momentum, accompanied by photon absorption as blue arrows and emission as red arrows, intraband transitions accompanied by phonon emission as dashed arrows, and electron scattering on a defect as horizontal dotted arrows [13], with figure (b), showing the spectra with the peaks responsible for scattering [13]. The D + D" peak is referenced as the G* peak in this thesis.

Cancer is the number one cancer found among men in the United Kingdom (figure 4), with 47,740 new cases in the UK between 2014–2016 [20].
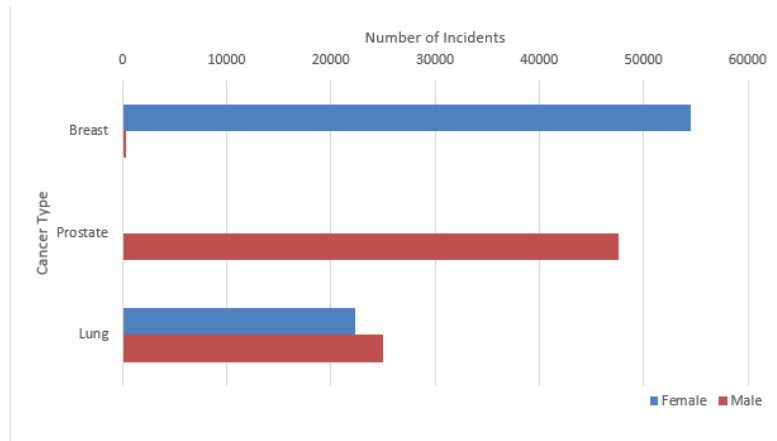

Figure 4: A graph to illustrate the top 3 most common cancer diagnosis' in the UK, diagnosed in 2016 [21].

There are currently many different methods used for the diagnosis of prostate cancer such as prostate specific antigen (PSA) blood tests and medical imaging. PSA testing is a simple blood test that measures the level of prostate specific antigens within the blood sample.

An article by Bartsch et. al [22] discusses the improvement of mortality rates, when mass PSA screening of men is offered to men between 45 to 75 years old in Tyrol, Austria. 32.3% of men between this age range took part in the PSA screening. Those who took part in the study with a PSA level higher that 10 ng/ml were advises to undergo a biopsy. From this mass screening of PSA scores, stage III extraprostatic disease decrease, as did stage IV metastatic disease. The mortality rate from prostate cancer related death also fell between 1993 and 1999 (Figure 5).
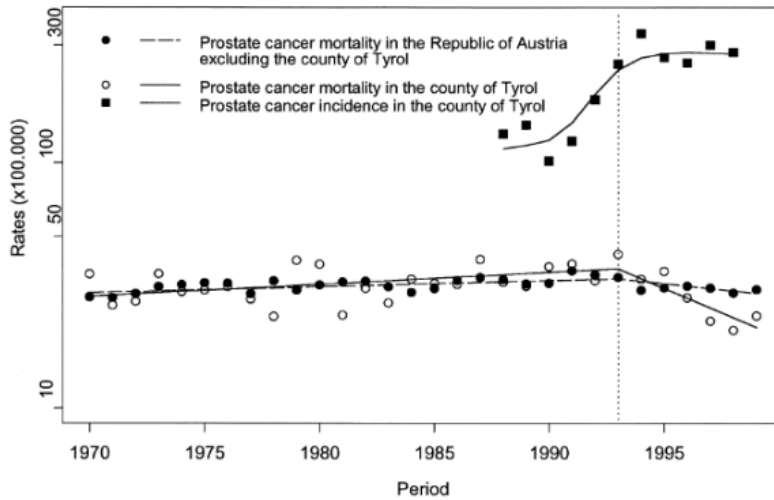
Figure 5: Prostate cancer mortality rates in Tyrol compared with the remaining republic of Austria population, and prostate cancer incidence rates in Tyrol in men aged 40 to 79 [22].

Although these results are both positive and encouraging results for mass early detection of prostate cancer, it is not always efficient. There are cases of prostate cancer that have low PSA levels, such as small cell carcinoma of the prostate which would go undetected in this screening case [23].

High PSA levels can lead to further medical investigation, such as through MRI or CT scanning. MRI scans can be used to detect tumours and understand staging [24, 25]. However, MRI scans cannot be performed on patients who have previous had metallic implants such as hip replacements, or pacemakers [26]. It is also expensive and does not work for real-time imaging [27].

Alternatively to this method, is the use of CT to diagnosis prostate cancer [28]. CT images are often fused with other images such a PET, to help identify tumours more efficiently [29]. PET scans can clearly show primary and secondary lesions but offers a very low spatial resolution, which is why it is often fused with CT [27]. PET and CT both use radiation so must be used with great care to not give unnecessary excessive

6

radiation to the patient [30].

A way of understanding the severity of prostate cancer's aggressiveness is quantified using the ′Gleason Score,′ with cancerous cells having a score between 6 and 10. These cells are obtained via a biopsy and are inspected and graded. Tumours with a primary score of 3 and a secondary score of 4 have a fairly good outlook, whereas cancers with a primary Gleason Score of 4 and a secondary score of 3, are more likely to grow and spread. [31]. This current method of grading is flawed, as a score of $3 + 4$ is shown as 7, but so is $4 + 3$ and these results are not interchangeable, despite both equaling 7 [32]. A biopsy is vital for the fundamental understanding of the cells within the prostate to stage the patient and guide the best treatment for them [33].

This clearly outlines that there is a need to find a more efficient way of diagnosis prostate cancer. The cells used in this thesis are P4E6 prostate cell lines. These cells were first obtained in 2001 by Maitland et. al [34]. They have been immortalised using the e6 protein from the human papillomavirus (HPV). P4E6 has a Gleason score of $''3+4 = 7''$, meaning most of the tumor is a grade 3, with some of its more aggresive parts at grade 4.

1.2.2   Raman Spectroscopy for Prostate Cancer Characterisation.

In 1990, there was a breakthrough with Puppels et. al [35], where the use of a 514.5nm laser allowed the characterisation of chromosomes. Since, Raman Spectroscopy has made leaps and bounds in biomedical applications, with its uses becoming more and more important to rapid detection of disease. This is due to its non-invasive, label-free analytical nature.

Since this breakthrough, Raman Spectroscopy has been used to characterise various type of cancer cells. This method of spectroscopy has been used in the detection of cancer [36]. This is currently a large area of interest with research in diagnosing the skin [37], breast [38], colorectal [39], cervix [40], and brain [41]. This is important, as the best

prognosis for a cancer patient is early detection. Spectral differences have been detected in tumor and healthy tissues.

Liu et. al. [42] use Raman spectroscopy to detect breast cancer. They found that breast cancer patients had a stronger peak in 1156, 1521, 2854 and 3013cm^{-1} in non-cancerous breast tissue when using resonance Raman, a technique in which can enhance the intensity of the Raman signal. The range of wavenumber in which results were taken was $500 - 4000\text{cm}^{-1}$.

Mavarani et. al [43] investigated colon cancer tissues using Raman spectroscopy.

There is extensive research into Raman spectroscopy used to better understand the protein and lipid contents of prostate cancer cells. This can be shown in figure 6, taken from a paper by Crow et. al, [44] which demonstrates a Raman spectra taken of a prostate cell with its major peaks labelled. This paper looks at various human prostate cell lines including LNCaP, PC 3, DU145 and PCA 2b but only looks into the fingerprint region $(400 - 1800\text{cm}^{-1})$ of its spectral signature. There is no discussion of the high wavenumber region in this paper.

Another paper by Potcoava et. al [45] shows again that Raman spectra can be taken of prostate cancer cell lines, taking data in both the fingerprint and high wavenumber region $(850 - 1800\text{cm}^{-1}, 2750 - 3050\text{cm}^{-1})$. They specifically analyzed LNCaP prostate cancer cells where they identified significant prostate cancer peaks.

1.3 Project Motivation

Raman has changed diagnostics within medicine due to its non-destructive and non-contacting nature [46], meaning it is possible to analyse biological samples with a Raman Spectrometer and take multiple data sets with no damage to the sample. It can give high spatial resolution images, which can study a range of biological samples such as cells, organisms and tissue.

There are many advantages to using Raman Spectroscopy as a biological tool. Using

8

vibrational spectroscopy such as Raman spectroscopy give minimal to no damage when studying a biological sample. There is no need to pre-treat the sample with any chemical or mechanical procedures, such as dyeing the sample. Another great advantage of using Raman spectroscopy as a biological tool is that it does not require an *in vitro* method to prepare the samples. The samples can be from an *in vivo* setting, meaning they are obtained in conditions that mirror how the biological sample would be found within its natural organism. There is a demand for *in vivo* diagnostic tools, as it solves the lengthy delays caused by the *in vitro* method and is non-invasive.

There is a lack of literature that analyses the P4E6 cell lines using Raman Spectroscopy. LNCaP is a metastatic prostate cell [47] and therefore, is a more advanced stage of prostate cancer and hence, a higher Gleason score. Therefore, P4E6 is best for this thesis investigation to understand earlier staged prostate cancer cells.
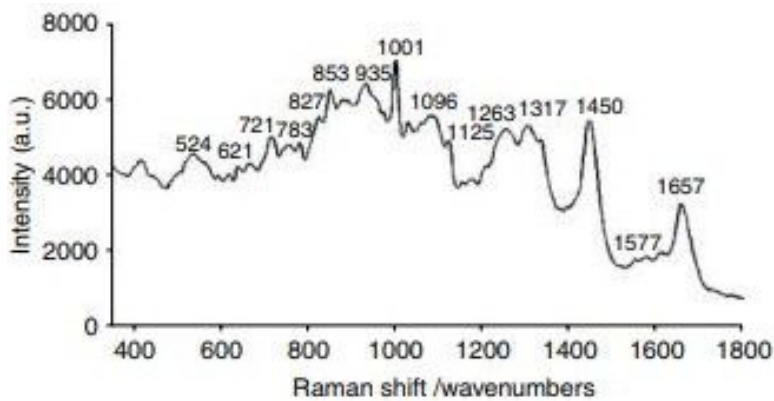

Figure 6: A Raman Spectra taken of a prostate cell line [44].

Seperately, Graphene has been shown to suppress cell growth of the bacteria E. Coli [48] and shown to that graphene oxide nanowalls can cause cell membrane damage [49]. It has shown antibacterial traits but the extent of its cytotoxicity to cells is still unknown. A study by Zhang et. al [50] shows graphene sheets are toxic to cells taken from rat

cells, measuring changes in the lactate dehydrogenase levels, indicating cell membrane damage which is a sign of cell death.

This leaves many questions about graphene's role within biomedical applications. It is currently being used for surface enhanced Raman spectroscopy [51], especially within biology [52] and has been shown as a potential substrate for biological application [53], which claims CVD graphene has no toxicity on mesenchymal stromal cells. There are issues surround this, mainly with the inhomogenity of the samples and the understanding of the interactions between graphene and biology.

This leads to the aim of this thesis. This thesis aims to set out a new technique to aid with early diagnosis of prostate cancer. This will be investigated using Raman Spectroscopy to understand prostate cancer cell lines as well as the cell's interactions with graphene, to further question if graphene can be used as a method to enhance the P4E6 cell line's Raman signal. In this report, I will demonstrate how to characterise chemical vapour deposition graphene using a Raman spectrometer instrument with the appropriate statistical and peak analysis.

In the following chapter, the prostate cancer cells P4E6 will be characterized with the appropriate statistical and peak analyses. Following on from this, P4E6 cells that are cultured onto a CVD graphene substrate will then be characterised and statistically analysed. Comparison of the graphene, cell, and there after, cell on graphene substrate will be analysed and discussed.

2 Methods

2.1 Raman Spectroscopy Background

Discovered by Sir C. V. Raman [54], Raman spectroscopy is now used as a tool to identify different sample make ups in different disciplines of science.

Raman Spectroscopy is a technique that uses vibrations to detect a change in polarisability. This can be shown theoretically. An induced dipole moment, μ_i is proportional to field strength, ε with a proportionality constant, α with α representing the polarisabilty of the molecule,

$$\boldsymbol{\mu_i} = \alpha\boldsymbol{\varepsilon}. \tag{1}$$

Written in Cartesian coordinate form, equation 1 becomes

$$\mu_x = \alpha\varepsilon_x, \quad \mu_y = \alpha\varepsilon_y, \quad \mu_z = \alpha\varepsilon_z$$

which is only applicable to completely symmetrical systems. Most molecules have symmetrical structures with different polarisations, α in the x, y and z planes, therefore,

$$\mu_x = \alpha_{xx}\varepsilon_x + \alpha_{xy}\varepsilon_y + \alpha_{xz}\varepsilon_z,$$

$$\mu_y = \alpha_{yx}\varepsilon_x + \alpha_{yy}\varepsilon_y + \alpha_{yz}\varepsilon_z,$$

$$\mu_z = \alpha_{zx}\varepsilon_x + \alpha_{zy}\varepsilon_y + \alpha_{zz}\varepsilon_z.$$

As the polarisability tensor is a symmetric tensor then $\alpha_{xy} = \alpha_{yx}, \alpha_{yz} = \alpha_{zy}$ and $\alpha_{xz} = \alpha_{zx}$. A particular coordinate set can be chosen as (x', y', z'). This is due to its properties as a symmetric tensor that allow all terms involving $\alpha_{x'x'}, \alpha_{y'y'}$ and $\alpha_{z'z'}$ non-zero, and all terms involved with $\alpha_{x'y'}, \alpha_{x'z'}$ and $\alpha_{y'z'}$ equal to zero. This leads to

$$\mu_x = \alpha_{x'x'}\varepsilon_{x'}$$

$$\mu_y = \alpha_{y'y'}\varepsilon_{y'}$$

$$\mu_z = \alpha_{z'z'}\varepsilon_{z'}$$

known as the 'principle of polarisability' [55]. A fluctuation dipole moment with the same frequency will be produced by a fluctuating electromagnetic field shown by,

$$\varepsilon = \varepsilon_0 \cos(2\pi\nu_0 t), \tag{2}$$

where ε = the equilibrium field strength and ν_0 = angular frequency of radiation. Electromagnetic radiation induces a fluctuating of frequency, ν_0 in the molecule and will emit or scatter radiation of frequency ν_0. This is known as Rayleigh scattering, as the frequency that interacts with the molecule and is then scattered or emitted, is equal to the frequency that interacts with the molecule.

In a case of a diatomic molecule vibrating with frequency ν_v, there is simple harmonic motion vibrations. A coordinate, q_v along the vibrational axis at time, t is governed by,

$$q_v = q_0 \cos(2\pi\nu_v t). \tag{3}$$

The small vibrational amplitude, if there is a change in polarisability is given by,

$$\alpha = \alpha_0 + \left(\frac{\partial \alpha}{\partial q_v}\right) q_v. \tag{4}$$

Substitution of equation (3) into (4) gives,

$$\alpha = \alpha_0 + \left(\frac{\partial \alpha}{\partial q_v}\right) q_0 \cos(2\pi\nu_v t). \tag{5}$$

Using equation (1), equation (2) and that the incident radiation of frequency ν_v interacts with the molecule, then the induced dipole moment is,

$$\mu_i = \alpha\varepsilon = \alpha\varepsilon_0 \cos(2\pi\nu_0 t). \tag{6}$$

With a substitution of equation (5) into (6) then the induced dipole moment becomes,

$$\mu_i = \alpha_0 \varepsilon_0 \cos(2\pi\nu_0 t) + \left(\frac{\partial \alpha}{\partial q_v} \right) \varepsilon_0 q_0 \cos(2\pi\nu_v t)\cos(2\pi\nu_0 t). \tag{7}$$

Using the trigonometric identity,

$$\cos(x)\,\cos(y) = \frac{1}{2}\left[\cos(x - y) + \cos(x + y) \right], \tag{8}$$

equation (7) can be rewritten as

$$\mu_i = \alpha_0 \varepsilon_0 \cos(2\pi\nu_0 t) + \left(\frac{\partial \alpha}{\partial q_v} \right) \frac{\varepsilon_0 q_0}{2} \cos(2\pi[\nu_0 + \nu_v]t)\cos(2\pi[\nu_0 - \nu_v]t). \tag{9}$$

The earlier term of equation (9) refers to Rayleigh scattering, as there is no change in frequency. The later term refers to Stokes or anti-Stokes scattering, also known as Raman scattering, due to the change in frequency factor, shown by

$$\text{Raman scattering} \quad = \quad \nu_0 \pm \nu_v$$
$$\text{Rayleigh scattering} \quad = \quad \nu_0$$

From equation (9), it shows that in order for there to be Raman scattering then

$$\left(\frac{\partial \alpha}{\partial q_v} \right) \neq 0, \tag{10}$$

where molecular vibrations are responsible for a change in polarizability, which is needed for Raman scattering to be possible [56].

There is a quantum approach to understanding Raman Scattering. This approach recognizes that the vibration energy of the molecule is quantised. The following molecules have the corresponding normal vibrations of

$$\text{non-linear molecule} \qquad 3N - 6 \text{ normal vibrations}$$
$$\text{linear molecule} \qquad 3N - 5 \text{ normal vibrations}$$

where N = number of atoms in the molecule. The energy of each vibration is equal to

$$E_v = h\nu\left(v + \frac{1}{2}\right), \tag{11}$$

where ν = the frequency of vibration and v = vibrational quantum number, equal to 0, 1, 2, 3, ... etc. Quantisation is in the Raman scattering with the use of pertubation theory, by applying the theory to the ground state molecular wavefunctions until new wavefunctions are obtained describing the vibrational excited state. Pertubating the wavefunction gives an energy which allows an understanding of Raman scattering with vibrational transitions occuring via this virtual energy level, which can be shown in figure 7. It shows,

Stokes scattering	Energy transition starts on the ground state, $v = 0$ and finishes at a higher vibrational energy state.
Rayleigh scattering	Energy transition starts and finishes on same vibrational energy state.
Anti-Stokes scattering	Energy transition starts on a higher vibrational energy state and finishes at a lower vibrational energy state.
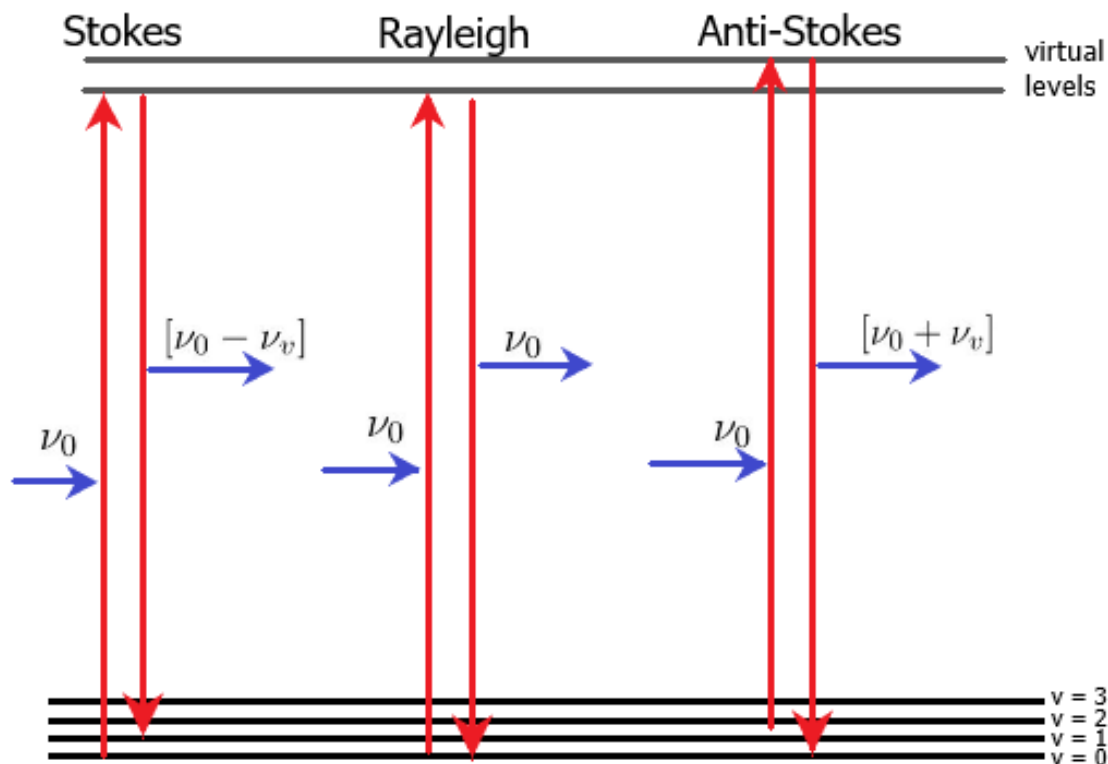
Figure 7: A model ideally representing how Stokes, Anti-Stokes and Rayleigh Scatterings occur from their corresponding vibrational energy states.

At room temperature, molecular vibrations are often in the ground state, $v = 0$ making Rayleigh scattering the most common to occur naturally. This also means that Stokes scatterings are more likely than anti-stokes and that Stokes scatterings will therefore have a more intense Raman signal [56].

Plotting a graph of $\alpha^{-\frac{1}{2}}$ in any direction forms locus points which produce a surface known as the polarisability ellipsoid, with axes of x', y' and z'.

For an anisotropic molecule, there are different values in different directions, ie. $\alpha_{x'x'} \neq \alpha_{y'y'} \neq \alpha_{z'z'}$ therefore, the ellipsoid has 3 axes of different lengths.

If 2 of 3 axes have equal values, ie. $\alpha_{x'x'} = \alpha_{y'y'} \neq \alpha_{z'z'}$, then the polarisability is equal in the x' and y' directions with a rotational ellipsoid.

15

For an isotropic molecule, ie. $\alpha_{x'x'} = \alpha_{y'y'} = \alpha_{z'z'}$, the molecule has equal polarisability in all directions.

If the polarisability ellipsoid changes in either size, shape or orientation, the Raman instrument will detect this. This change in ellipsoid is from either molecular vibration or rotational vibration and results in a Raman spectra [55].

The raman spectra contains information showing the magnitude of the change in polarisability during vibrations, which then leads to an understanding of the molecule's structure. We can use the derived tensor to understand polarisation effects, shown by

$$\alpha'_{ij} = \left(\frac{\partial \alpha_{ij}}{\partial q} \right) \tag{12}$$

with the expectation that the intensity of the Raman scattering is proportional to this. Due to rotational scattering, an average can be taken over all orientations,

$$\bar{\alpha}' = \frac{1}{3} \left(\alpha_{x'x} + \alpha_{y'y} + \alpha_{z'z} \right) \tag{13}$$

where $\bar{\alpha}'$ is the mean value. Anisotropy can be shown by

$$\gamma'^2 = \frac{1}{2} \left[(\alpha_{x'x} - \alpha_{y'y})^2 + (\alpha_{y'y} - \alpha_{z'z})^2 + (\alpha_{z'z} - \alpha_{x'x})^2 + 6(\alpha_{x'y}^2 + \alpha_{y'z}^2 + \alpha_{z'x}^2) \right] \tag{14}$$

these are the invariant quantities need to express the scattering intensity in terms of equation 12. Applying this to an incident unpolarised light propagating in the y-direction and scattering in the x-direction, we can redefine the polarisation to be

$$\rho_n = \frac{I_y}{I_z} \tag{15}$$

Then, taking an average over all molecular orientations, equation 15 can be

$$\rho_n = \frac{6(\gamma')^2}{45(\bar{\alpha}')^2 + 7(\gamma')^2} \tag{16}$$

For Raman scattering only (not Rayleigh). If using incident plane polarised light then,

$$\rho_p = \frac{3(\gamma')^2}{45(\bar{\alpha}')^2 + 4(\gamma')^2} \tag{17}$$

where subscript p = polarised incident light. The following values show the polarisation of light

$$\text{if } \rho_p \begin{array}{|c|} = 0.75 \\ < 0.75 \\ = 0 \end{array} \quad \text{light is} \begin{array}{|c} \text{depolarised} \\ \text{polarised} \\ \textbf{completely } \text{polarised} \end{array}$$

This depolarisation ration can be used to determine the symmetry of rotation by associating the polarisability with a spherical or isotropic part $\bar{\alpha}'$ and an anisotropic part, γ'. The anisotropic part is responsible for the change in size of the ellipsoid.

For any vibration that is symmetric the size of the ellipsoid changes, with its orientation remaining the same. Therefore, the diagonal elements of the polarisability ellipsoid change, meaning ther must be a change in $\bar{\alpha}'$, changing equation 13 and hence resulting in a change to equation 17, $\bar{\alpha}' \neq 0$ and the line must be polarised, therefore $\rho_p < 0.75$. For anti-symmetric vibrations, $\bar{\alpha}' = 0$ as there is no change in the polarisation tensor, therefore the Raman lines due to antisymmetric vibrations are depolarised, making it useful to determine the symmetry of vibrations [57].

2.2   Raman Spectroscopy's Instrumentation

This thesis uses a Horiba XploRA$^{\text{TM}}$ PLUS Raman Spectrometer, with a confocal Raman microscope and a 532nm laser [58], along with the use of LabSpec6 [59] for collecting spectra, where data was saved and later analysed using Igor Pro 8.
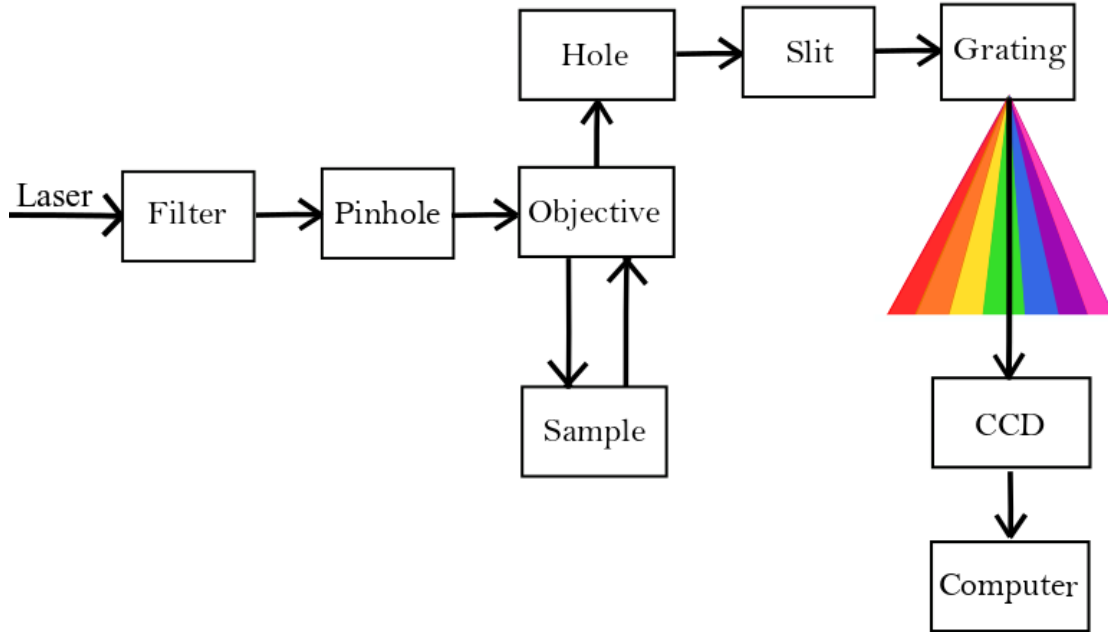
Figure 8: An schematic image representing the components and set-up of the Raman instrument used in the experiments within this thesis.

Figure 8 shows a simple schematic set-up of the Raman instrument used in this thesis, with components within the instrument. The black arrows represent the laser light travelling through the instrument. A more in-depth discussion of these components is outlined in this section.

2.2.1 Spot Size

The spot size of the laser can be determined using the following equation,

$$x = \frac{1.22\lambda}{NA} \tag{18}$$

where λ = the wavelength of the laser light, NA = the numerical aperture of the objective lens and x = the spot size. In the experiments that will be taken out in this thesis, the

following values apply $NA = 0.9$ from the 100x objective and $\lambda = 532nm$ therefore we can show the spot size is

$$x = \frac{1.22 \times 532nm}{0.9} = 721.16nm. \tag{19}$$

2.2.2 Spatial Resolution

Spatial resolution can be calculated by

$$sr = \frac{0.61\lambda}{NA}. \tag{20}$$

Substituting in the numerical values of 0.9, we can calulate spatial resolution to be

$$sr = \frac{0.61 \times 532nm}{0.9} = 360.57nm. \tag{21}$$

This equation can only be used for the $x - y$ spatial resolution, where the spatial resolution in the z direction is more complicated.

2.2.3 Confocal Microscopy

Confocal Microscopy works using the principle of florescence. Often, mercury lamps are used in florescent microscopy but confocal microscopy uses lasers as opposed to these mercury lamps. This is to stop the florescence that causes a blurry image. These blurs come from a lack of focus. When using confocal microscopy, the image is taken using a camera that has a pinhole. This pinhole only allows the light of one focal plane to be focused on the camera. The pinhole cancels out the light coming from above and below the focal plane. This pinhole also eliminates the noise interference of light that could be detected from elsewhere.

The laser is focused in a small region of the specimen. There are mirrors in the instrument

that rotate in the x and y direction, that allow focus in different regions across the sample. The laser scans the whole surface of the sample and captures images of each spot where a software can combine these dots to make one sharp image. This is known as *Confocal Laser Scanning Microscope*. This can be used to generate 3D images as the laser can capture across different focal planes. The set up of a confocal microscope can best be described in figure 9.
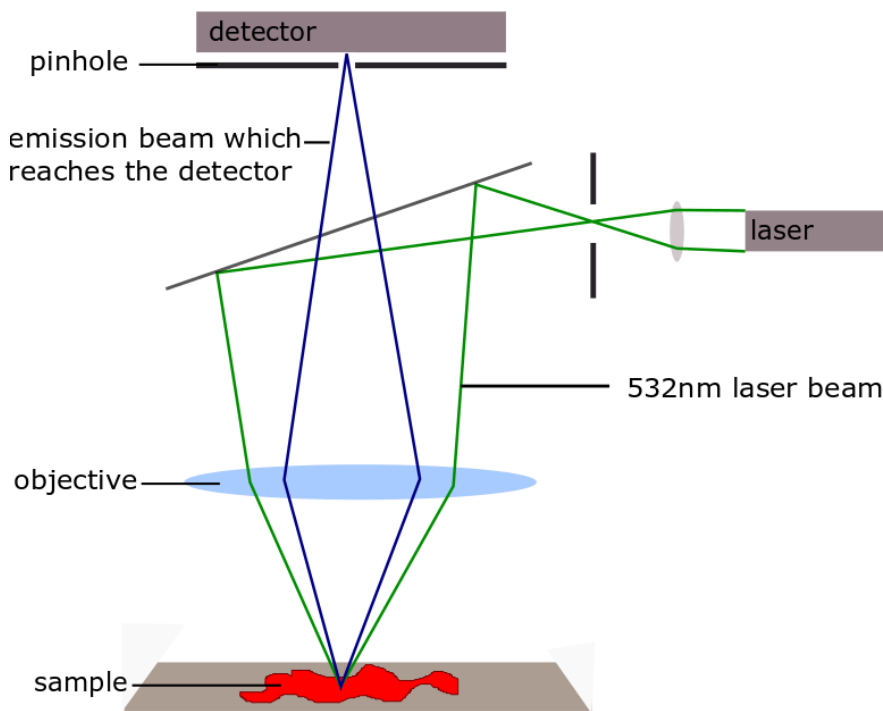
Figure 9: An image representing confocal microscopy.

2.2.4 Filters

Filters can be used to limit the allowed wavelengths of colour through. Their selectivity can be increased by stacking the filters, but this can decrease the intensity. A filter than can be used to block out other forms of radiation is called a interference filter.

For constructive interference, two layers of semi-transparent silver film are separated,

with a transparent dielectric film between both silver layers. The spacer film has a low refractive index, with a thickness, d which can determine the wavelength as a function given by

$$\lambda = f(d) \tag{22}$$

This method can be shown in figure 10.

transparent dielectric spacer film

Light travels in and reaches the second silver screen

Part of the light is refracted back, shown in red and part of the light is transmitted, shown in green

It is refracted again back to the second silver screen

It is transmitted again. If the waves are in phase with matching troughs, the wavelength of that wave will undergo constructive interference with all other wavelegths undergoing destructive interference

semi-transparent silver film

Figure 10: An image representing a how the use of two semi-transparent silver layers and a transparent dielectric spacer film can act as a filter in Raman spectroscopy.

The wavelengths undergoing constructive interference are given by

$$m\lambda = 2d\sin\theta. \tag{23}$$

As this is constructive interference, the waves are in phase therefore $\sin\theta = 1$. As $d =$ thickness of the spacer film and as shown in equation 22 it effects wavelength, λ we can show that for an order of interference where $m = 1$, wavelength is equal to double the distance between the spacer film.

There is also a prism monochromator. This uses a prism to disperse light according to the wavelength needed and a series of mirrors, which directs the desired wavelength of light to an exit hole. This is best shown in figure 11.
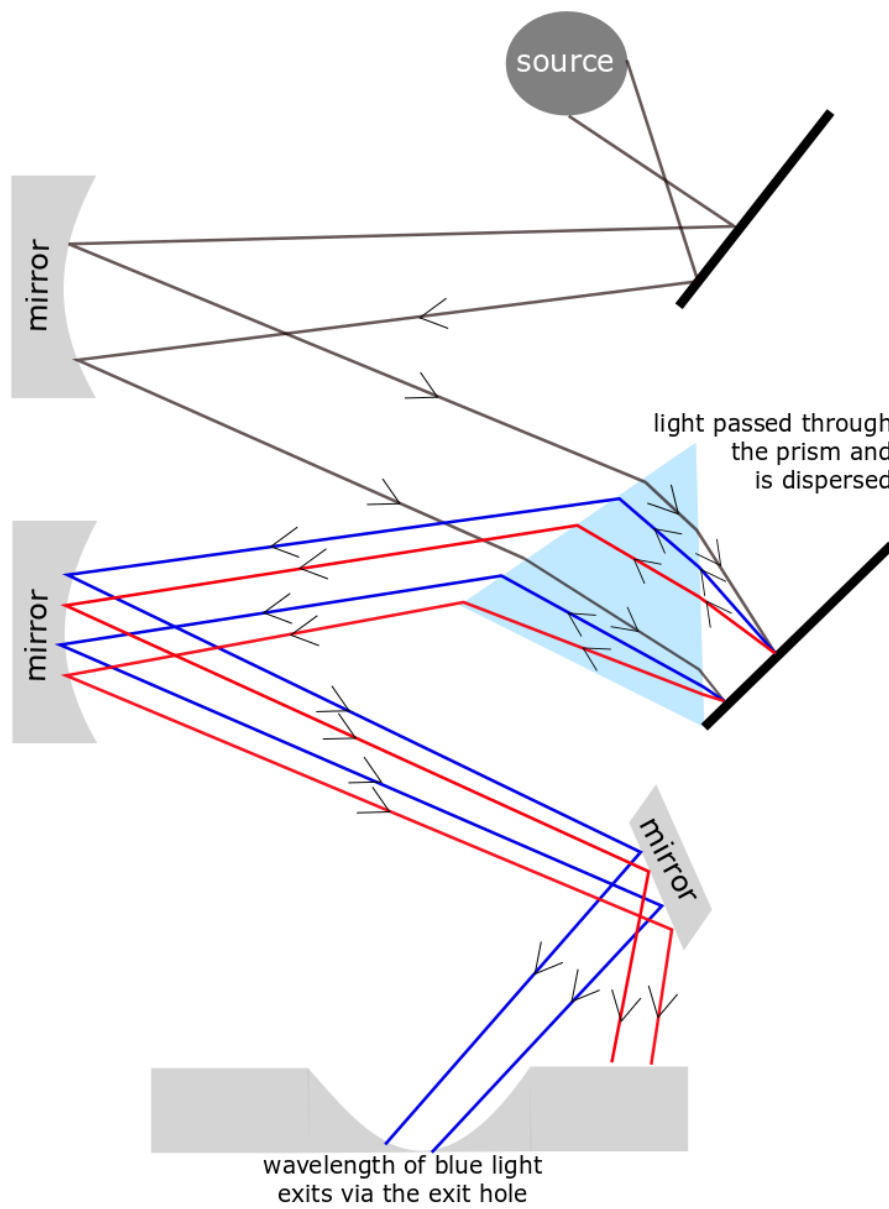
Figure 11: An image representing a prism monochromator.

2.2.5 Diffraction Gratings

A diffraction grating contains closely space grooves that are etched onto a reflective surface. When the light falls on this surface, it is diffracted. The diffracted light from

different grooves can overlap leading to inference. Certain wavelengths of light can be in and out of phase, leading to constructive or destructive interference. Due to this, there is an increase in accuracy as there is a high number of destructive and constructive interference.

Looking back at equation 23, we can show that the distance of the grooves is now represented by d, with $\lambda =$ wavelength of incident light. λ can be obtained by changing θ, which can be achieved by rotating the grooved surface.

There are different measurements of grating with more or less lines etched in them. For example, a grating of 1800T and 2400T. T is the unit for grooves per mm, so the higher the grating value, the more grooves per mm and the smaller the distance between them. If there are less lines, d between them will increase. Looking again at equation 23, we can say as d increases, so does λ. Looking at the equation for wavenumber,

$$\bar{\nu} = \frac{1}{\lambda} \tag{24}$$

it shows that a smaller number of grooves gives a lower range that the wavenumber data can be taken over. For a higher range of data the 2400T grating should be used. This allows a higher resolution.

2.3 Characterisation of Graphene

Four separate graphene samples were looked at during this report, supplied from graphene supermarket [12]. The graphene is abstracted using chemical vapour disposition (CVD) on a silicon oxide substrate. The graphene supplied is single layered CVD graphene films, which are transferred onto 285nm p-doped SiO_2/Si wafer which is 1cm x 1cm in size. Graphene supermarket state that the product is about 98% graphene coverage with minor holes and organic residues [12]. More than 95% of the product is single layered with less than 5% as a bi-layer [60]. Each film is polycrystalline (grains with different crystallographic orientation) with no A-B stacking order. They are randomly oriented with respect to eachother. A sheet resistance of 215-700 Ω/square is reported by graphene supermarket [12]. I am confident this is accurately reported by graphene supermarket due to the characterisation from the manufacturer being inline with what is expected for a single layer sheet of graphene.

All four samples were analysed using different parameters, firstly using graphene parameters similar to literature methods to understand their inhomogenities. They were then analysed biologically for comparison, before the cell samples were then grown on them.

2.3.1 Analysis of Graphene Samples Using Graphene Parameters.

In a paper by Ferrari et. al [14], where pristine graphene is analysed, power at the sample is kept between 0.04 to 4mW to avoid causing damage to the graphene sample. Therefore in the first part of this thesis, all spectral data is taken with a 100x objective, with a numerical aperture equal to 0.9. The sample is illuminated with a 532nm laser and with the use of confocal microscopy parameters for the purpose of the later biological analysis. Confocal microscopy parameters include a slit width equal to 200μm and hole equal to 100μm, with a grating of 2400T. These settings are important for obtaining results on one plane of focus. Slit width changes the spectral resolution achieved instrument. A low slit width is used, as the lower the slit width, the greater the spectral resolution.

The hole width changes the focal plane of the laser, with a larger pinhole resulting in more focal planes. This is kept as low as 100μm as many planes of focus could affect the results, adding unnecessarily large information from the substrate when trying to analyse cell data. For the characterisation of graphene prior to the biological analyses, graphene samples were analysed in the following way (Table 1).

Sample Number	Power at Sample (mW)	Filter (%)	Acquisition Time (s)	Accumulations	Slit Width (μm)	Hole (μm)	Grating (T)
1	0.75	10	2	10	200	100	2400
1	1.875	25	2	2	200	100	2400

Table 1: Table to summarise the Graphene Parameters used by the Raman spectrometer to analyse graphene sample 1 used within this thesis.

Only graphene sample 1 is analysed using the lesser powered graphene parameters.

2.3.2 Analysis of Graphene Samples Using Biology Parameters.

The graphene literature concludes that the laser power be kept between $0.4 - 4$mW, but the literature does not use graphene as an interface for biology. Biology signals have a weak signal. Due to this, it is best to use a laser power within the upper part of this range, rather than a weaker laser power at the lower part of this suggested range, hence this thesis has used a laser power of 3.75mW. This keeps the laser power within the suggested range, but is optimal for cell analysis.

The biology parameters used for this thesis are shown in table 2. A 50% filter is used, so that a strong enough signal can be obtained from the prostate cell lines to allow for peak analysis. Previous work within the group shows a trypan blue assay of the cells after these parameters does not damage the cells due to laser power [61]. Therefore, the 50% filter keeps the power at the sample low to prevent damage to the cells, whilst still using a high enough laser power to obtain a signal that has not been swamped by noise

and is hence, unable for analysis. From this previous work, it is known a laser power of 3.75mW at 45s acquisition time is optimal for cell analysis using Raman spectroscopy. This is important for the future analyses, when Raman spectra will be obtained after the prostate cells are grown on the graphene interface.

Replicates have also been taken at 3.75mW at 90s acquisition time to investigate the effect this will have on the analysis of graphene compared with the lower laser powers.

Sample Number	Power at Sample (mW)	Filter (%)	Acquisition Time (s)	Accumulations	Slit Width (μm)	Hole (μm)	Grating (T)
1, 2, 3, 4	3.75	50	45	2	200	100	2400
1, 2, 3	3.75	50	90	2	200	100	2400

Table 2: Table to summarise the Biological parameters used by the Raman spectrometer to analyse graphene samples used within this thesis.

2.3.3 Data Analysis of Graphene Spectra.

For all the above parameteres, there were 120 spectral measurements taken at random points across the sample for every parameter and sample, except for sample 4 under the biology parameters, which has 111 spectral measurements. An image of graphene under the 100x objective within the instrument can be shown in figure 12. Intensity is taken in arbitrary units on the y-axis, against wavenumber, cm^{-1} on the x-axis.
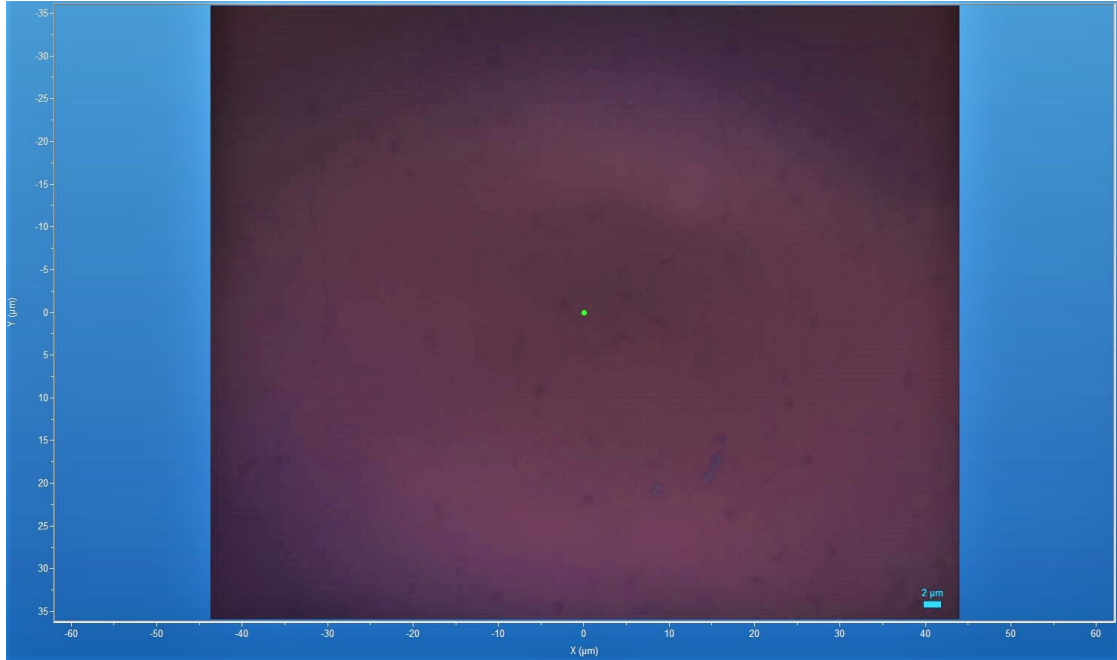
Figure 12: An image showing graphene at 90s under a 100x objective. This is graphene sample 1, spectra number 20. The green spot shows the laser reference spot, with the scale bar representing 2 μm.

Once collected, data undergoes various methods of analyses. All data is first baseline subtracted using the programme Raman Tool Set, via polynomial baseline subtraction. This data is then imported to Igor Pro 8, where various statistical analyses are performed. An average of all spectra of different parameters is calculated along with the standard error of the mean. Consulting with the literature, peaks could be fitted to the average to calculate their location, full width at half maximum (FWHM) and their amplitude. These fittings could also be applied to the average spectra with the standard error added and subtracted to calculate the error in the location, FWHM and amplitude. Convergence tests of the standard error of the mean and the second order standard deviation were ran at 10 spectra intervals, shown in figure 29. These spectra were chosen at random using a random number generator generated using a python code.

The error in the values of location, FWHM and amplitude were calculated by first creat-

ing two new waves. The standard error in the mean (SE) was added and subtracted from the average to make these two new waves, referred to as 1) *average + SE*, and 2) *average - SE*. Peaks were then fitted to these waves the same as the average and the values for location, FWHM and amplitude were extracted. The error is then simply calculated by the largest difference in the average of these values compared to either average + SE or average - SE. It should be noted that there is an instrumentation error associated with the wavenumber of 3cm^{-1} due to mechanical and alignment errors.

The error in the peak intensity ratio was then calculated using the error values in amplitude calculated by the following equation

$$error = I \cdot \sqrt{\left(\frac{\delta x}{x}\right)^2 + \left(\frac{\delta y}{y}\right)^2} \tag{25}$$

where I is the calculated peak intensity ratio, x is the amplitude of the first peak used in the ratio, δx is the calculated error in this value and y is the amplitude of the second peak used in the ratio, with δy being its calculated error.

2.4   Prostate Cancer Cell's Interactions with Graphene.

For this thesis, P4E6 cell lines were cultured in the Cancer Research Unit at the University of York's Biology Department. The cells are kept in the incubator at 37°C and fed with Keratinocyte Basal Medium II (K2) media when appropriate. The culture of the P4E6 cell lines is a three day process which all takes place in a sterile fume hood to prevent contamination of the cells.

 On day 1, the media is removed from the cells in the T25 flask using a suction pipette. The flask is then washed with 3ml of phosphate-buffered saline solution. This is then removed with the suction pipette and 1.5ml of trypsin is added to the flask. This is placed back in the incubator at 37°C until the cells are no longer attached to the flask. 6ml of R10 media is then added to the flask and transferred to a smaller test tube so

(a)   (b)
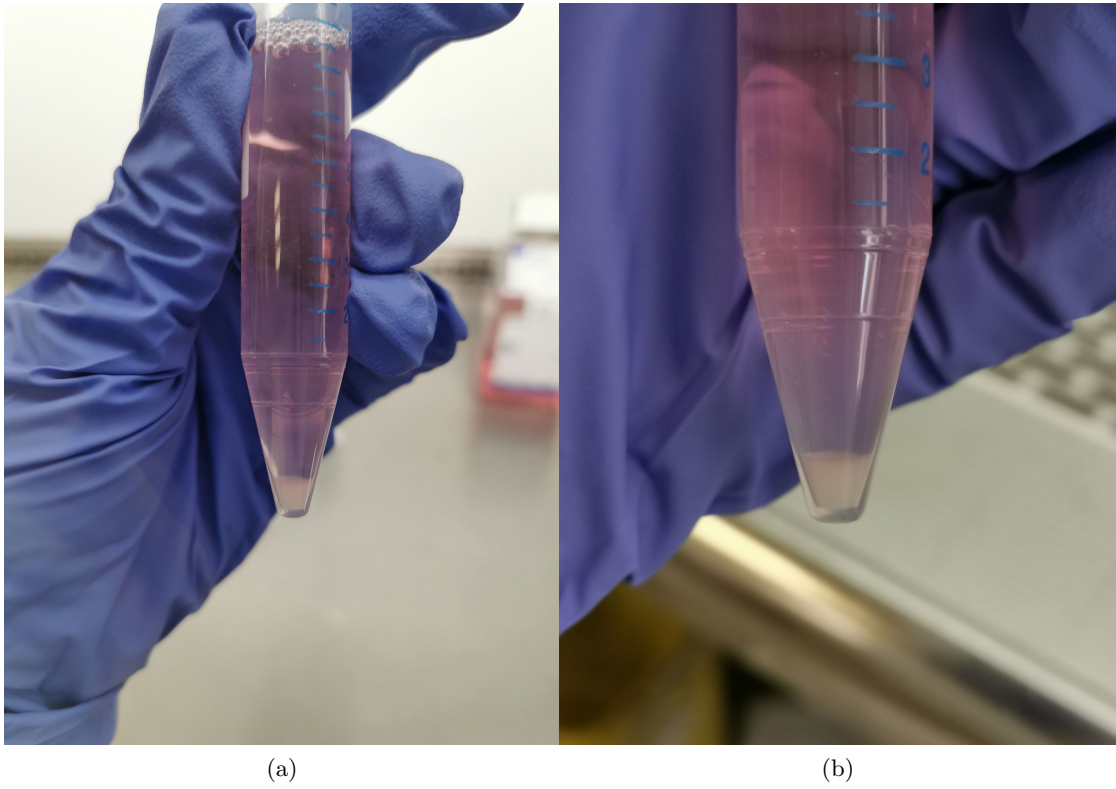
Figure 13: An image showing a P4E6 cell pellet in R5 media after being spun down in the centrifuge.

it can be spun down to form a cell pellet in the centrifuge. It is spun at 1500rpm for 5 minutes with the breaks equal to five. The remaining media is then suctioned off with care, making sure not to touch the pellet. The pellet in media can be shown in Figure 13, and the remaining pellet once the media has been pipetted off can be shown in Figure 14.
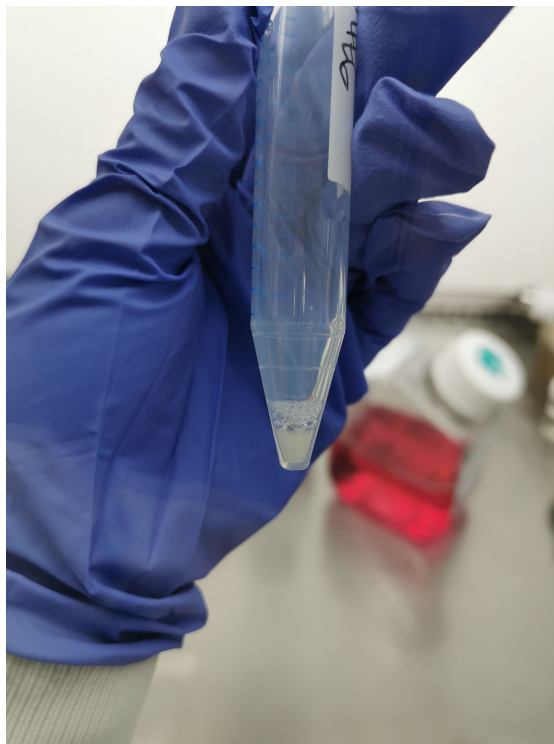
Figure 14: An image showing a P4E6 cell pellet after being spun down in the centrifuge and once the R5 media has been pipetted off the cell, leaving only a cell pellet within the test tube.

The cells were then resuspended in K2 [62] media making sure to break up the pellet and disperse the cells into the media, shown in Figure 15. $10\mu L$ of this cell-media mix is then placed onto a haemocytometer slide so that the cells can be counted. The number of cells needed for a dried sample is 10,000 so the appropriate volume needed for the substrate was calculated. The cells were plated onto the substrate inside a 35mm dish.

For the characterisation of the cells, three samples were plated onto calcium flouride slides along with three samples plated on graphene samples - which were previously characterised in the previous chapter.
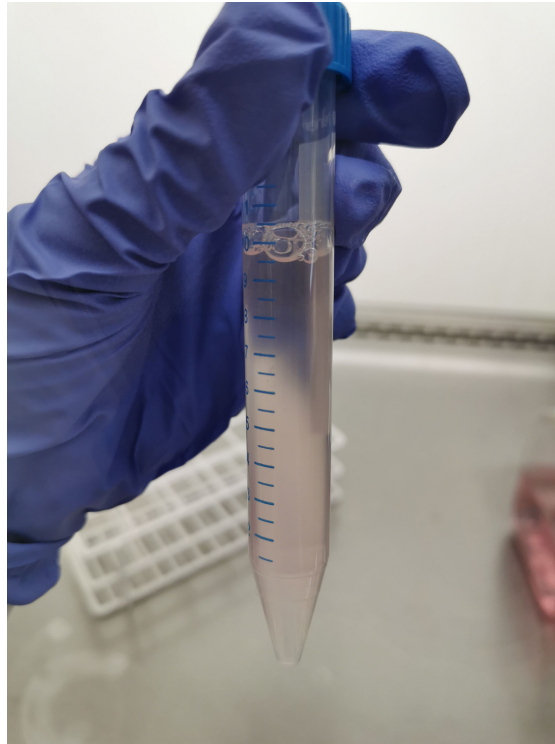
Figure 15: An image showing the cell pellet once it has been re-suspended in K2 media. This image shows how the cells have been completely dispersed back into the media and there is no remaining cell pellet left in the bottom of the test tube.

They were left to rest on the substrate for 10 minutes, shown in Figure 16 and then $25\mu L$ of antibiotic and antimycotic solution and 2.5ml of K2 media was added. This was then placed in the incubator at $37°C$ for 24 hours. The second day the media is changed to starvation media which has no serum in order to bring all the cells to the same cell cycle. First the old media is drained then $25\mu L$ of antibiotic and antimycotic solution is added along with 2.5ml of Keratinocyte-SFM media. This is then readded to the incubator at $37°C$ for a further 24 hours.
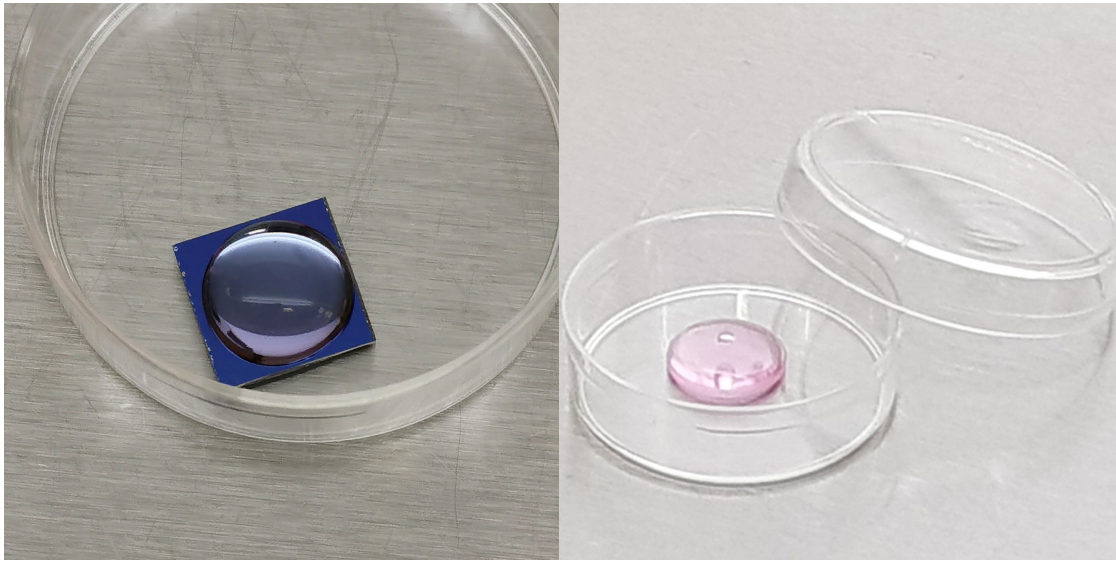
(a) P4E6 cells in media resting on a graphene sub-(b) P4E6 cells in media resting on a CaF_2 substrate.
strate.

Figure 16: An image showing P4E6 resting on the substrate required. This shows the volume required to have 10,000 cells on the substrate calculated the haemocytometer. This liquid is left on the substrate for 10 minutes to allow the cells to settle towards the substrate and then further media is added.

On the third day the cells were dried out and prepared for Raman imaging. Figure 17 shows the P4E6 cell lines dried onto graphene before they are analysed on the Raman instrument. First the media is drained and the disk is washed gently with Hank's Balanced Salt Solution. This is repeated again and the drained a final time. The disk is then left to dry in the fume hood, shown leaving to dry in figure 16, and after the drying is completed in figure 17. They are then taken to the Raman instrument for data collection.
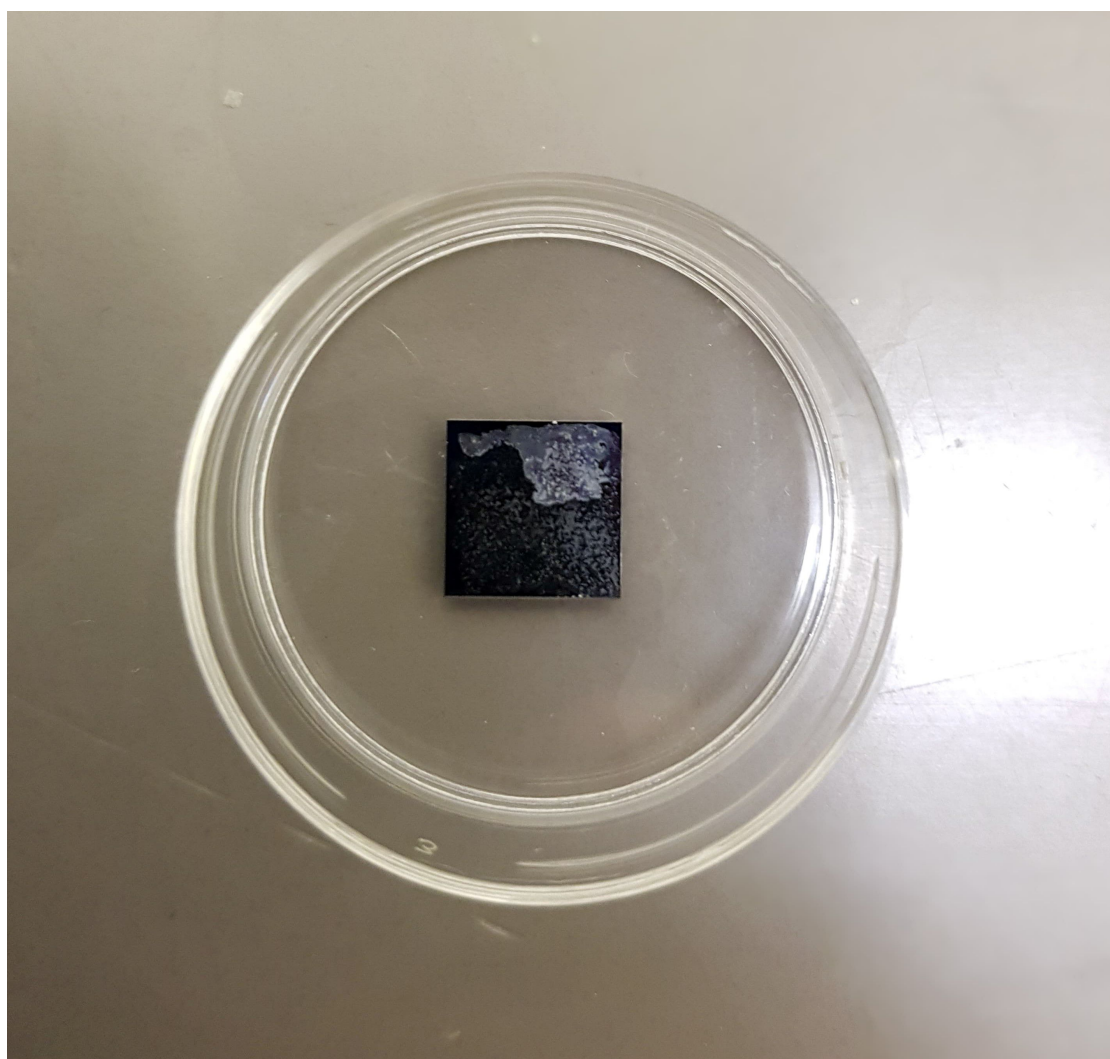
Figure 17: An image to show P4E6 cells that have been dried on a graphene substrate.

Calcium fluoride slides were used to carry out the characterisation of the P4E6 cell lines due to their signal raman signal peak at 320cm^{-1}, which is out the range of wavenumber investigated in this thesis. It is known to have a flat background which allows there to be little interference with the results. It allows the production of a good signal-to-noise ratio whilst preventing large result interference [63].
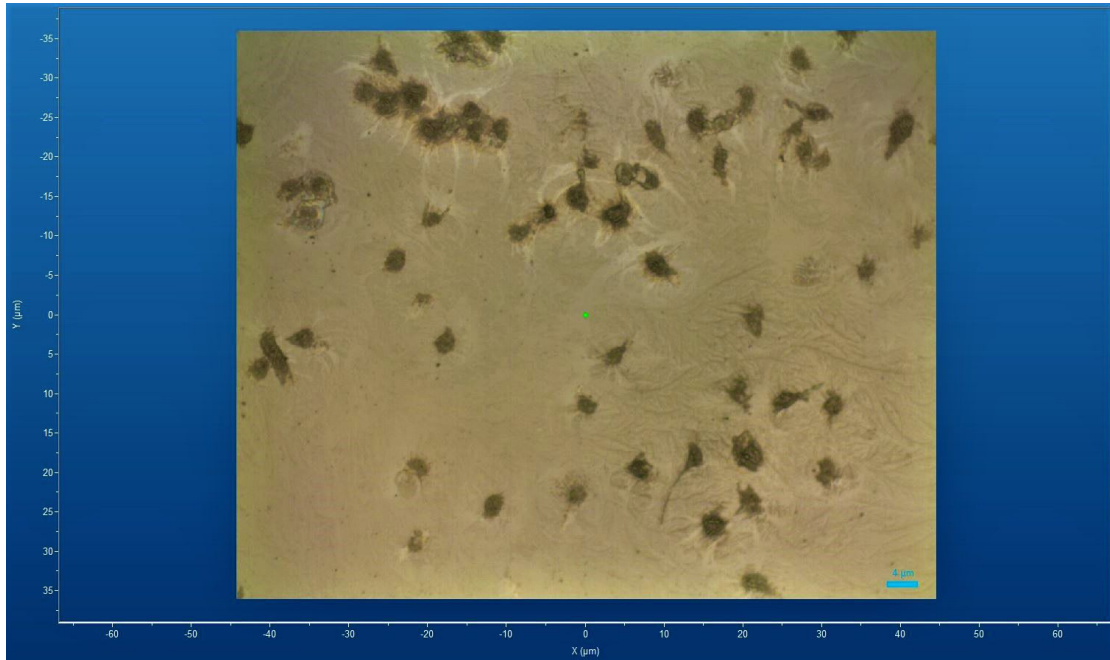
Figure 18: A figure to show the population of cells on a CaF_2 substrate under a 10x objective within the Raman instrument. The green spot shows the laser reference point and the scale bar represents 4 μm.

Figure 18 shows an image of the population of the P4E6 cells on calcium fluoride when cultured using this method at a 10x objective, with the bar representing 4 μm. 29 seperate cells were selected at random across four seperate samples, with a total of 145 spectra in total being obtained. An example of the cell under a 100x objective is shown in both figure 19 which is cultured on calcium fluoride and figure 20 shown cultured on graphene. The green dot is the laser reference point, with the red dotted circle highlighting the cell. The scale bar represents 2 μm. The green laser point is

35

placed at 5 random points across the cell to obtain different reference points across the cell.
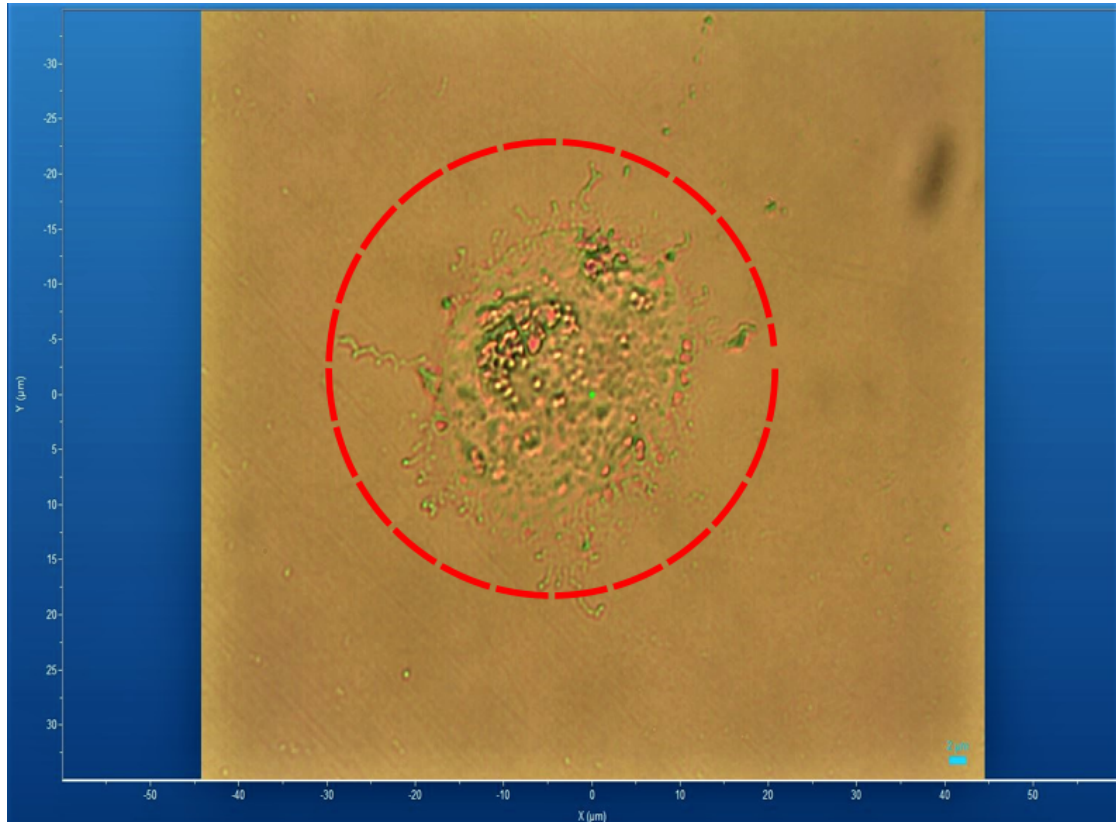
Figure 19: A figure to show cell 8, reference 1 cultured on CaF_2 slide taken from sample 1 under a 100x objective lens. The red circle highlights the cell, the green central dot shows the laser reference point and the scale bar represents 2 μm.
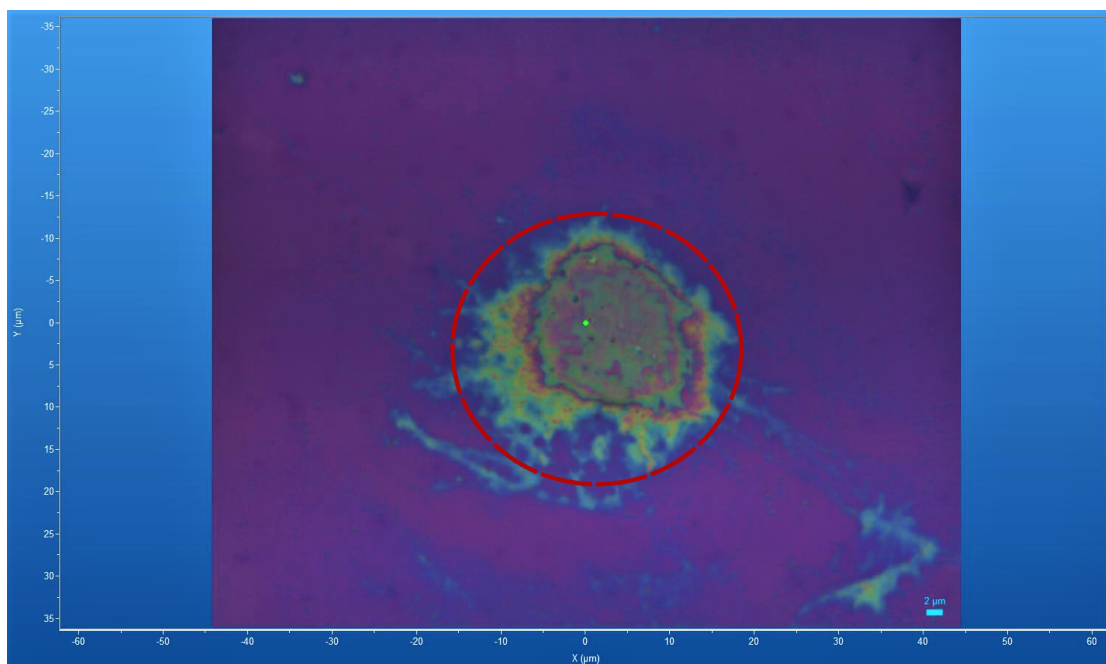
Figure 20: A figure to show cell 1, reference 1 cultured on graphene, under a 100x objective lens. The red circle highlights the cell, the green central dot shows the laser reference point and the scale bar represents 2 μm.

Once the data is collected, it undergoes various analyses and data preparation. It is treated similarly to that of the data taken of graphene to allow a fair comparison. Firstly undergoing the same polynomial baseline subtraction. Then it is imported to Igor Pro 8 and an average across all samples and all cells is calculated along with the standard error in the mean. Peak fittings are performed with a comparison to literature, allowing to obtain and compare values of FWHM, location and amplitude for Peak Intensity Ratio comparisons. Again, convergence tests are performed, this time at intervals of 5 due to the complex nature of spectra. These are calculated using the same python random number generator. The average, standard error in the mean and second order standard deviation is then calculated at each 5 spectra interval using the average wave feature within Igor Pro 8.

3 Results and Discussion

3.1 Raman Spectroscopy to Characterise Graphene

An expected result for graphene is shown in figure 21. This figure is taken from a paper by Lee et. al [64] where we can see the G peak, G* peak and G' peak.
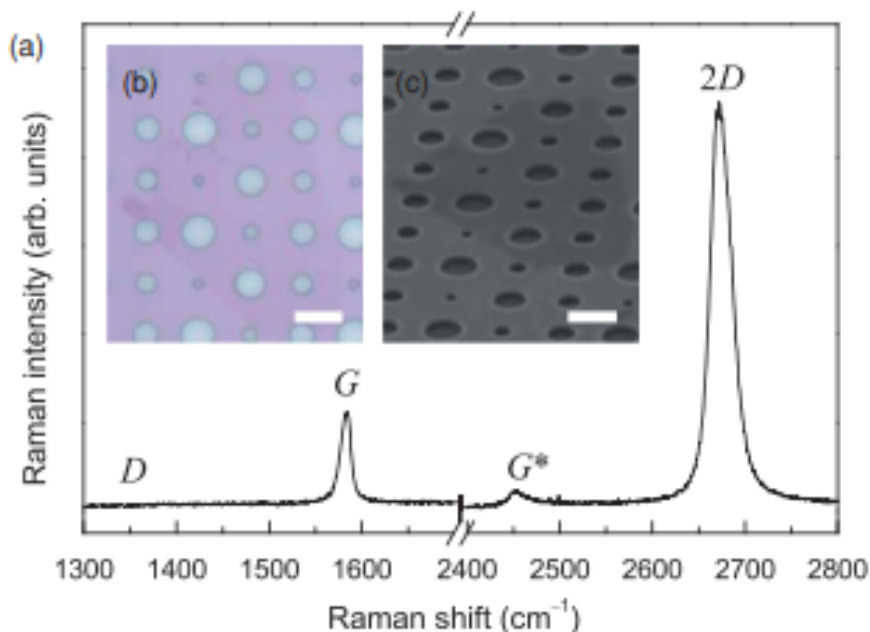
Figure 21: An image showing a graph of an expected spectra of pristine graphene, taken from a paper by Lee et. al [64].

The G* band is left out of the analyses in literature, therefore no analysis have been performed on this peak in this report. The D peak is also labelled, but shows no intensity as this graphene sample is pristine and therefore has no defects so hence the lack of D band. For CVD graphene, a D peak is expected at 1350cm^{-1}, a G peak at 1585cm^{-1}, and a G' band at 2693cm^{-1} [15]. Comparing this with figure 23, we can see that this spectra has been reproduced, except this time there is a D band present. This is because the sample analyzed in this thesis is CVD graphene and therefore has defects.
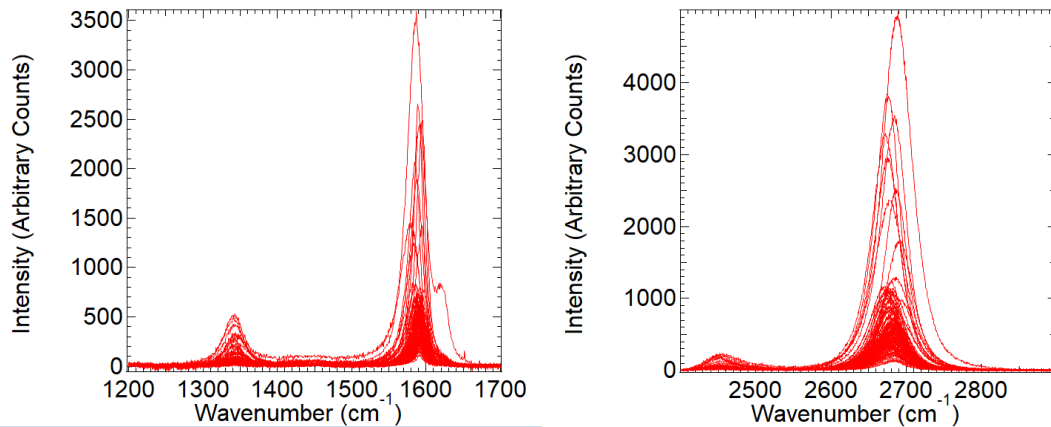
(a) All 120 Graphene Spectra Data for Sample 1.   (b) All 120 Graphene Spectra Data for Sample 1.

Figure 22: A figure to show all spectra taken across random points of each graphene sample at 45s acq. time, 50% filter.

Figure 22 shows all 120 spectra of graphene sample 1 taken using the biology parameters at 50% filter with a 45s acquisition time. The average of figure 22 was computed using the average graphs function in Igor (Figure 23). The standard errors in the mean were also calculated. The average with the standard error added and subtracted were calculated, and then added to figure 23, shown in the grey shaded area. Therefore it has been shown that the characterisation has been completed. This is not as expected by Lee et. al [64] but this is due to the graphene sample being obtained via CVD and therefore is not pristine. This is shown by the visible D band.
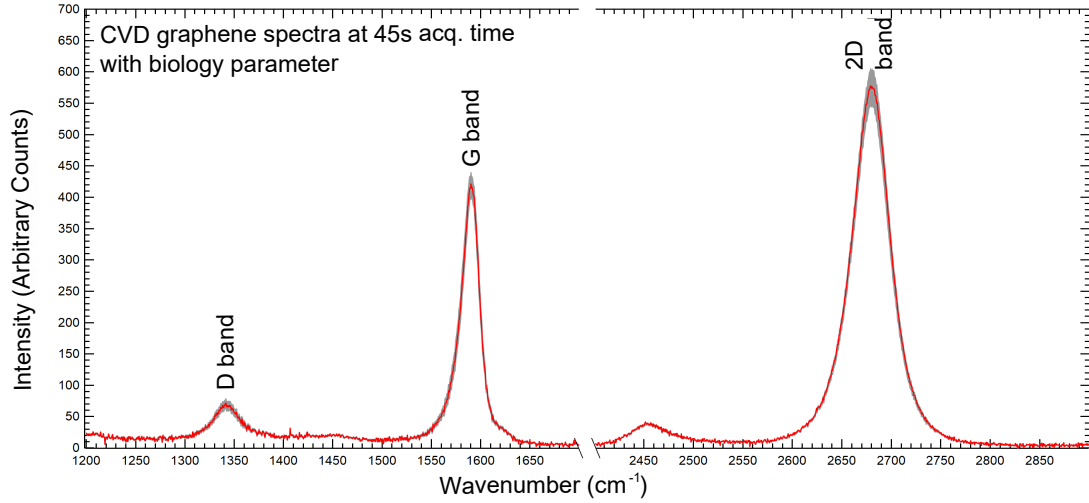
(a) Sample 1

Figure 23: Graph to show intensity in arbitrary counts plotted against wavenumber of the Raman spectra data taken using a 532nm laser to analyse three separate samples of graphene. 120 data points were chosen at random across each sample. The red line represents the average of 120 spectra taken from each sample. The grey shaded area shows the average spectra with the standard error added or subtracted. All data was baseline subtracted using Raman Tool Set before the average spectra was calculated. These measurements were taken using biology parameters with an acquisition time equal to 45s and a 50% filter.

Once the average was plotted, peaks could be fitted to the D band, G band and the G' band using the peak fitting function in Igor. Fitting peaks to these bands allows the extraction of data about their location, full width at half maximum and their amplitude which can be used to calculate peak intensity ratios. This data can then be compared to literature.

Papers by both Hussein [16] and Matsubayashi et. al [17] show that the G-band is best fitted with a double Lorentzian peak. A voigt fit was tried for the G-band, but this returned a higher Chi-Square value, so therefore, the double Lorentzian was used for the fit of the G-band in this thesis. Examples of these fits are shown in figure ??

The final fit for the G-band double Lorentzian is shown in figure 25. Peak 1 in figure 25
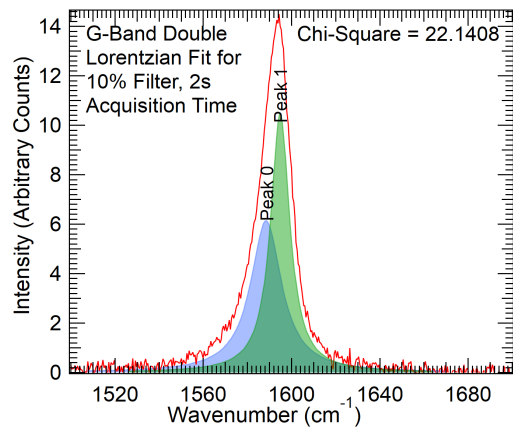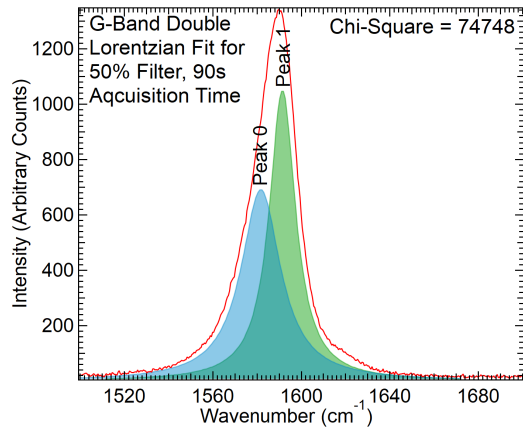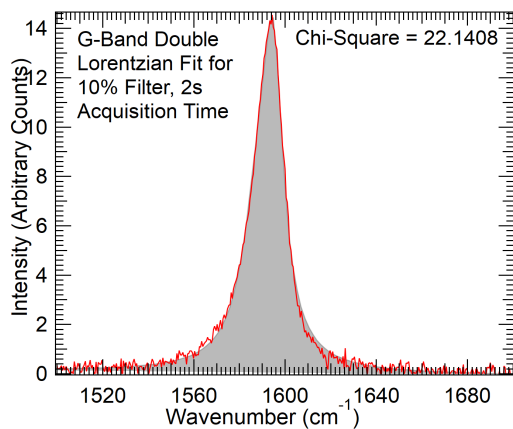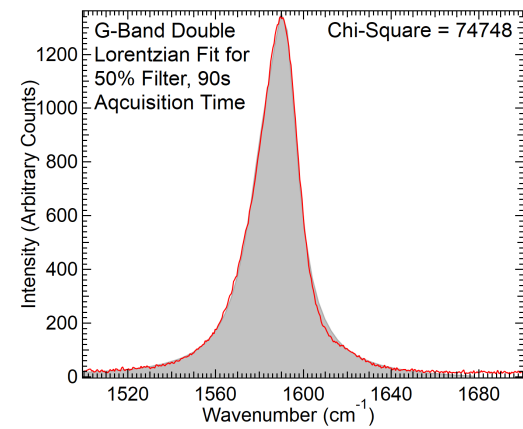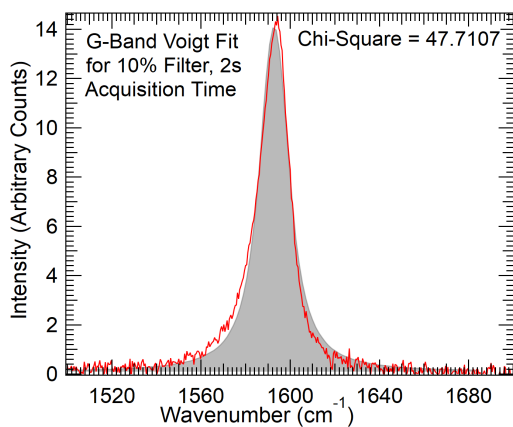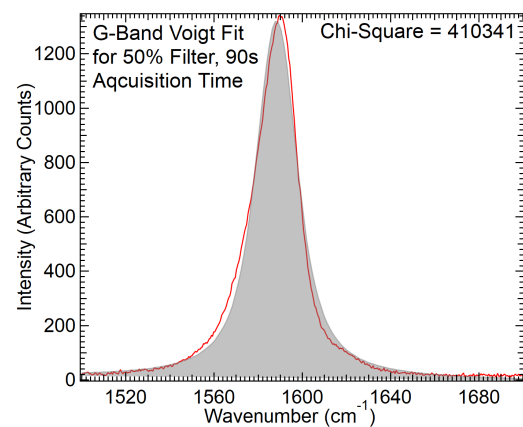
Figure 24: A figure to show various peak fitting methods of the G-band in graphene.

is what has been used as the G peak throughout this thesis as it is most represented by the literature and shown in the papers by Matsubayashi et. al [17] and Hussein [16].
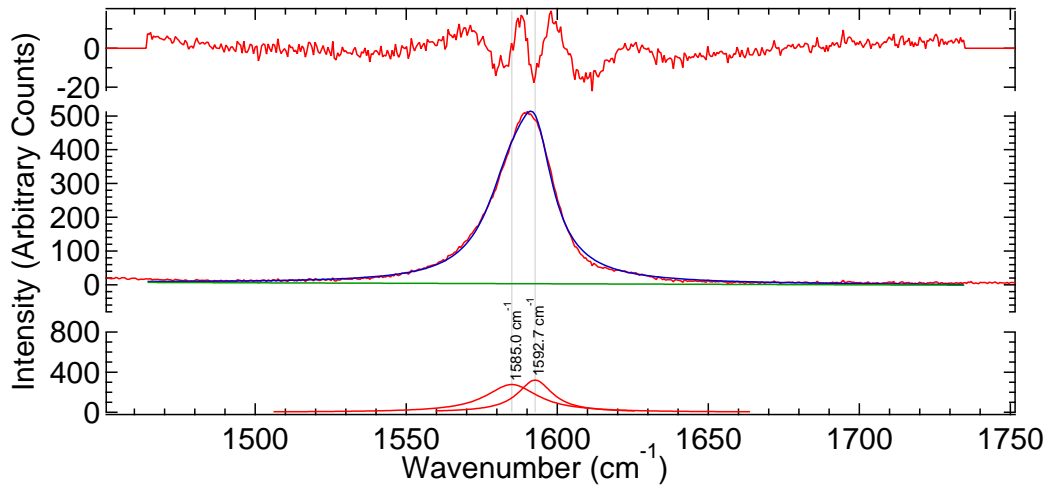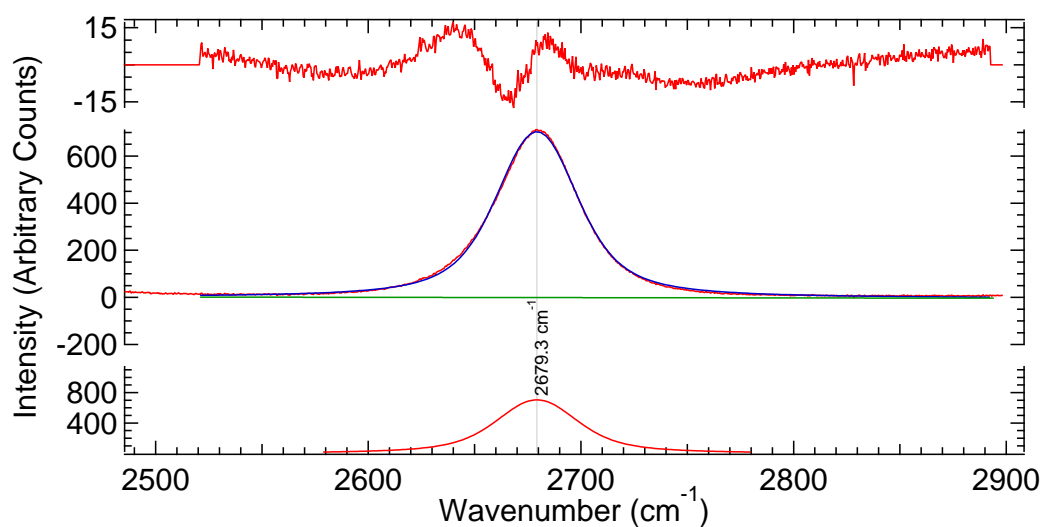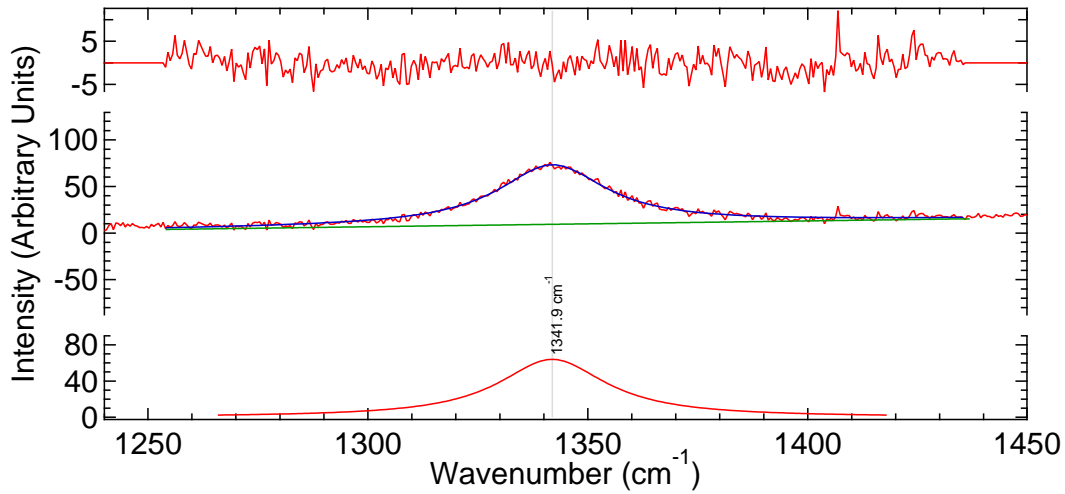

Figure 25: An image showing an example of the G band double Lorentzian fit for graphene sample 1 at 45s acq. time, 50% filter. The top red line shows the residuals of the fit. The red peak in the middle y-axis shows the average, where the blue shows the double Lorentzian fit and the bottom y-axis graph shows the two peak fits, with the location of each shown.

Hussein et. al [16] discuss that the G' band has a marginal improvement when fitted with a Voigt as apposed to a Lorentzian fit. Both fittings have been tried in this report, shown in figures 26.
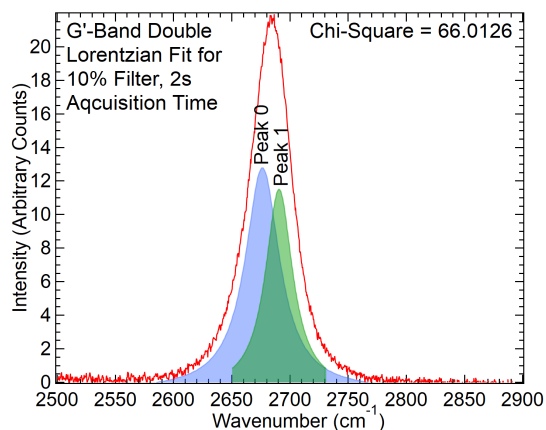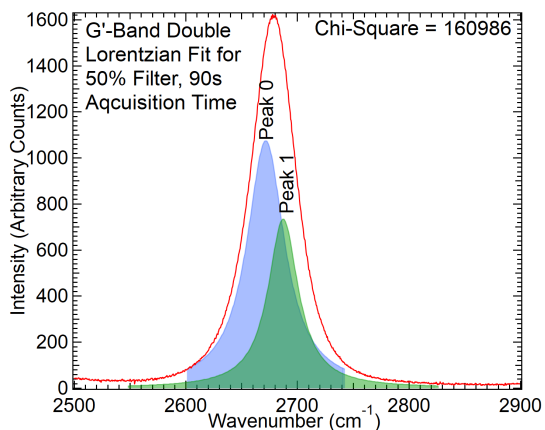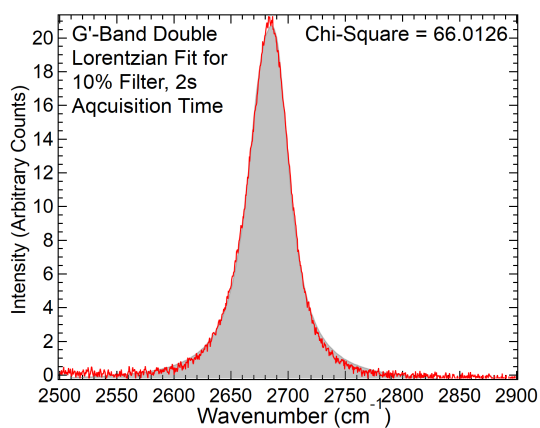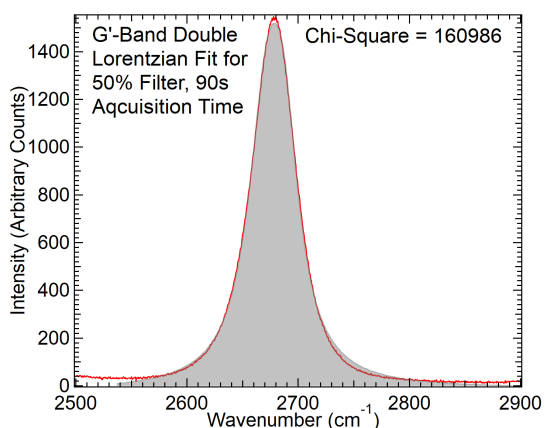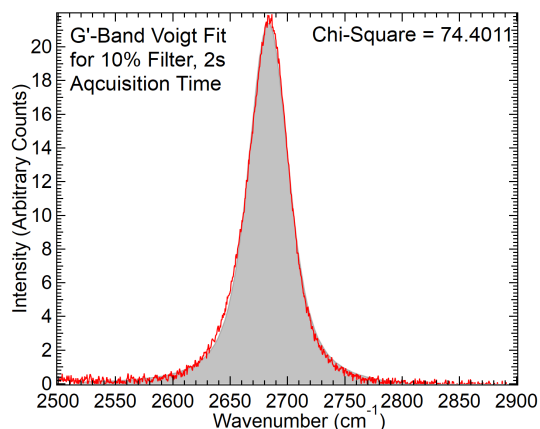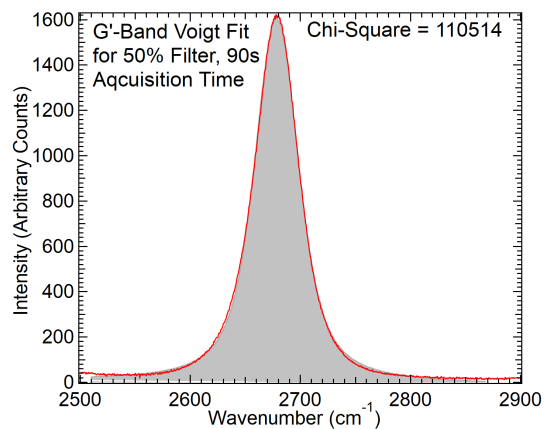
Figure 26: A figure to show various peak fitting methods of the G'-band in graphene.

Looking at these figures, it shows that the G' band is best fitted with a Voigt fitting as it is returning the smallest chi-squared value for the lowest and highest laser power. This suggests broadening of the graphene layer from the instrument. Fitting with more than one peak to the G' band is only appropriate for multi-layer graphene or graphite [14], and hence is not an appropriate fit as this graphene is not multi-layered. The final voigt fit for the G' band is shown in Figure 27.

Figure 27: An image showing an example of the G' band Voigt fit for graphene sample 1 at 45s acq. time, 50% filter. The top red line shows the residuals of the fit. The red peak in the middle y-axis shows the average, where the blue shows the Voigt fit and the bottom y-axis graph shows the final fit, with the location shown.

The D band is best fitted with a Lorentzian shown in figure 28.

Figure 28: An image showing an example of the D band Lorentzian fit for graphene sample 1 at 45s acq. time, 50% filter. The top red line shows the residuals of the fit. The red peak in the middle y-axis shows the average, where the blue shows the Lorentzian fit and the bottom y-axis graph shows the final fit, with the location shown.

To obtain full confidence in the results taken in this thesis, it is important to run statistical analyses on these results. This can be shown through convergence tests taken out on the results.

Figure 29 shows different convergence tests for the number of measurements taken of graphene in intervals of 10 with the biology parameters of 45s acquisition time, 50% filter. The standard error of the mean can be shown in figure 29 parts e and f, which is calculated in the average at increasing increments of 10 extra measurements. This graph shows that at 10 measurements, the spectra is much more susceptible to noise, with the standard error in the mean also being much greater than that of the standard error in the mean calculated at 120 measurements. It shows that as the number of measurements increase, the standard error in the mean decreases. Around the 90 measurements mark for the standard error in the mean, the spectra are stacked showing convergence at this point. This is important to understanding the statistical viability of the characterisation of the material. As CVD graphene is often defected, even if only slightly, it is vital to
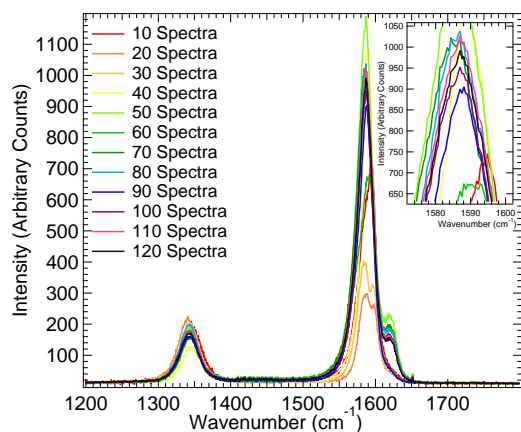
45

obtain an average spectrum that is reliable statistically, especially if being used for situations where defects could affect its application.
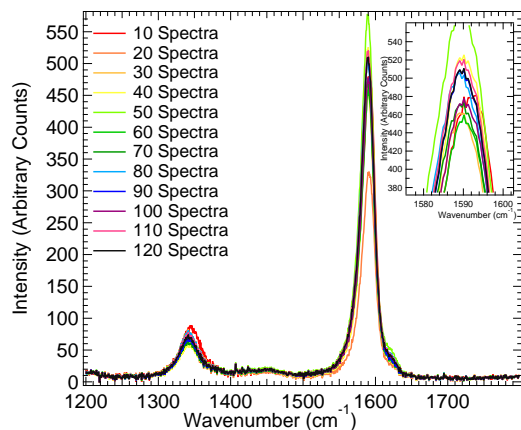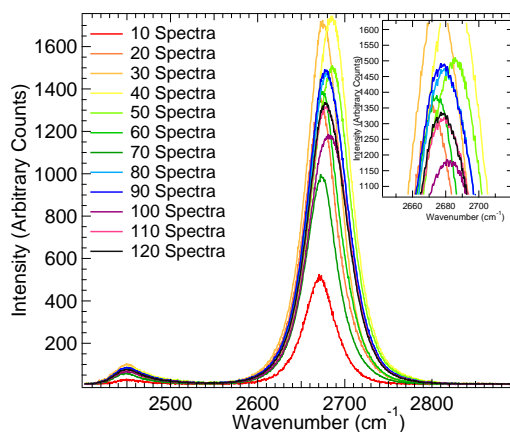
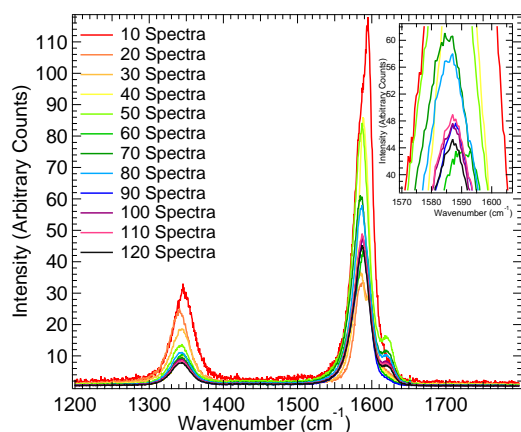(a) Sample 1 50% filter, 45s, average
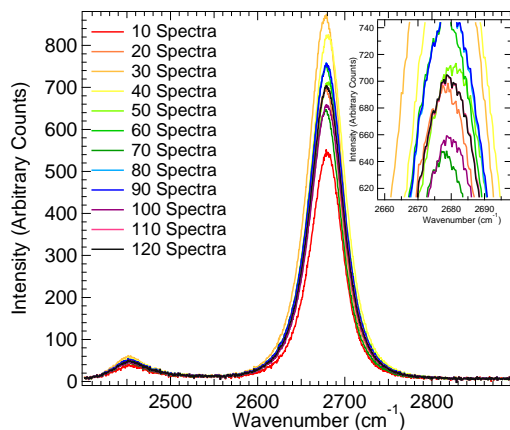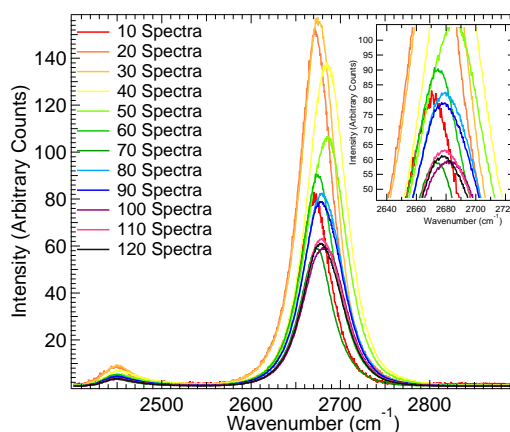
(b) Sample 1 50% filter, 45s, average

(c) Sample 1 50% filter, 45s, 2nd order sd

(d) Sample 1 50% filter, 45s, 2nd order sd

(e) Sample 1 50% filter, 45s, se

(f) Sample 1 50% filter, 45s, se

Figure 29: A figure to show the convergence tests calculated for sample 1 at 50% filter, 45s acq. time.

Looking again at figure 29 parts c and d, shows the second order standard deviation of the average calculated and plotted at intervals of increasing 10 measurements, from 10 to 120. Second order standard deviation allows us to understand the uncertainty distributions from the mean. Once again, the spectra begin to stack upon one another, this time around the 70-measurement mark, but is almost completely stacked from 90 measurements onwards. This shows that the variation in data begins to decrease at the 70-measurement mark, with barely any variation from 90 measurements onwards. This is again showing statistical viability in graphene's average spectra when there are 120 spectra used to plot its characterisation. The G-peak standard deviation shows the peak splitting, showing the asymmetry in the spectra.

Also looking at the average spectra calculated at increasing 10 measurement intervals in figure 29 parts a and b, shows the variations that can happen in increasing measurements. The first 50 measurements intervals show quite a variation in results, however from 60 measurements onwards the spectra are once again stacking. This confirms the accuracy statistically.

Once fitted with confidence, the following data was obtained (table 11) showing the average locations, and FWHM for all peaks across biology parameters (50% filter, 45s acq. time).

Average Across All 4 Samples for 50% filter, 45s acquisition time.				
Band	Location, cm^{-1}	Calculated Standard Error in Location, cm^{-1}	Full Width at Half Maximum (FWHM), cm^{-1}	Calculated Standard Error in FWHM, cm^{-1}
D Band	1341.2	±0.3	29.6	±0.5
G Band	1591.4	±0.8	14.1	±0.5
G' Band	2677.6	±0.6	44.3	±0.7

Table 3: Table to show the location, FWHM of each band in all graphene, along with their representative calculated standard errors in the mean. These values were calculated by averaging over graphene samples 1, 2, 3 (n=120) and 4 (n=111). These are the results for the biology parameters where acquisition time is equal to 45s with a 50% filter. Note that there is an instrumental error within the location and FWHM of $\pm 3cm^{-1}$.

48

The expected value for the G' FWHM is shown in table 5 and is higher than expected. This could be due to the fact the laser power at the sample is much greater than that used in the literature. Another method of understanding the homogeneity of graphene is understanding its peak intensity ratios with comparison to the literature. The average of the peak intensity ratios across all four samples are are best visualized in fig 30 and are summarised shown in table 4.

Figure 30 shows the change in peak intensity ratios across the various fits. There are greater inconsistency in the 0-peak fit to the G-band. Sample 4 also appears to have an inflated peak intensity ratio to that of the rest of the samples despite being taken under the same parameters. Sample 4 only has 111 spectra compared to the 120 spectra taken for all other 3 samples, but this shouldn't effect the results by a large amount due to the convergence test results.
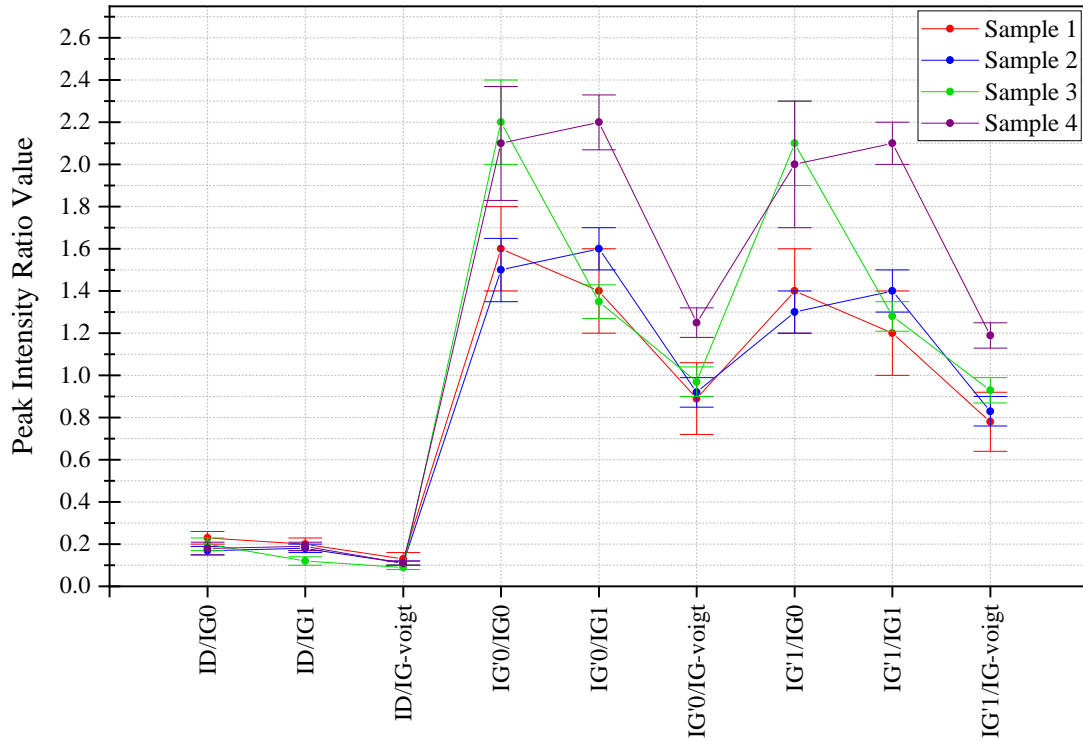
Figure 30: A figure to show the Peak Intensity Ratio of Various Fits of all four graphene samples with 45s acq, 50%filter parameter conditions. Sample number key is shown in the top right hand corner.

Figure 30 shows the difference in PIR across different parameters. Again, there is a large inconsistency with with ratio with the G-band 0-peak fit, with large error bars associated with it. This shows that the G-band 0-peak fit is not the most reliable way to obtain information about the peaks location, hence 1-peak being used for the analysis in this thesis. The I_D/I_G ratio is higher under a larger laser power. This can be due to the longer acq. time obtaining more information from the sample.
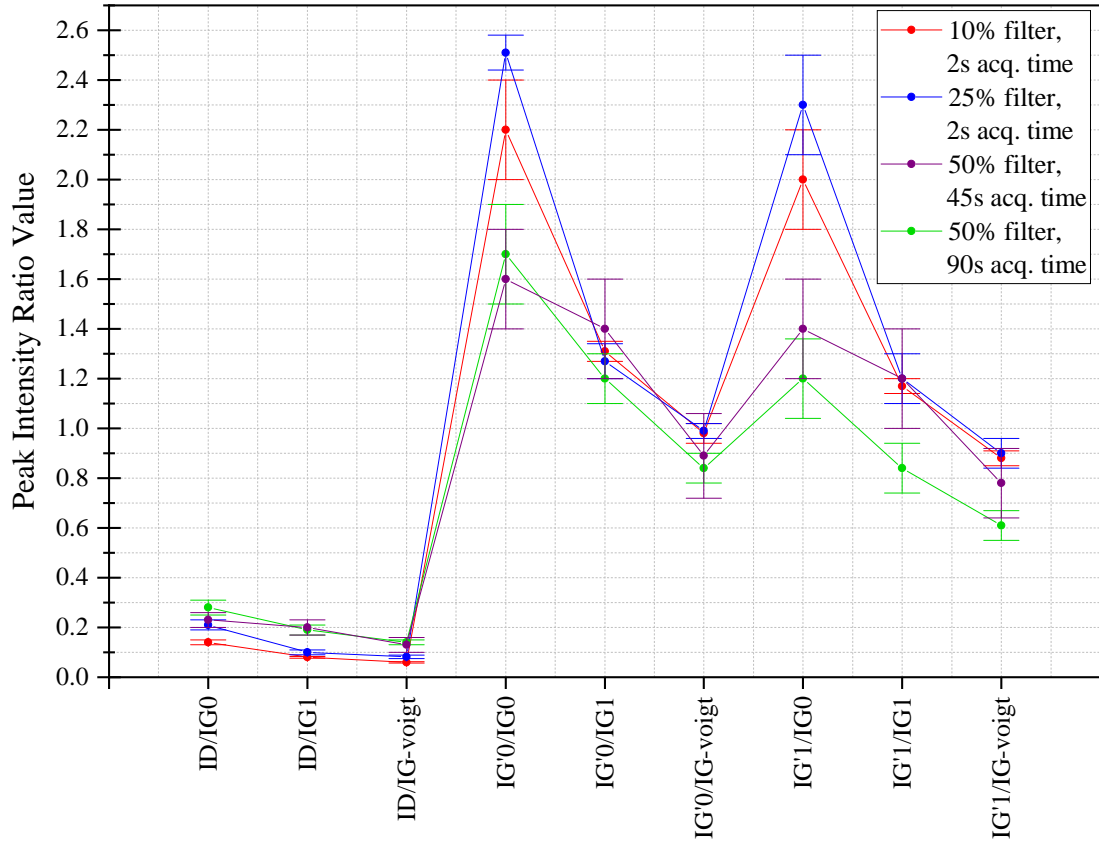
Figure 31: A figure to show the Peak Intensity Ratio of Various Fits under four seperate parameter conditions for graphene sample 1, which are shown in the key located in the top right hand corner.

These inconsistencies in the ratios show how inhomogeneous the CVD graphene samples are. These inconsistencies are worrying for biological applications, as it is unknown the outcome of these inconsistencies if they were to contact cells. There is also inconsistencies across a change in parameters, shown in figure 31. This shows that laser power can effect these results.

As discussed, the D-band is representative of the defects within the graphene. Therefore, using its intensity in a peak intensity ratio to the G-band gives an indication into the quality of the graphene sample being characterised. The G' to G intensity ratio indicates

Results for all samples for 50% filter, 45s acquisition time.			
Sample Number	Peak Intensity Ratio	Value	Standard Error in the Mean
1	I_D/I_G	0.20	± 0.03
2	I_D/I_G	0.18	± 0.02
3	I_D/I_G	0.12	± 0.02
4	I_D/I_G	0.19	± 0.02
1	$I_{G'}/I_G$	2.2	± 0.3
2	$I_{G'}/I_G$	2.4	± 0.2
3	$I_{G'}/I_G$	2.2	± 0.1
4	$I_{G'}/I_G$	3.6	± 0.2
Average of all results			
Ave.	I_D/I_G	0.17	± 0.05
Ave.	$I_{G'}/I_G$	2.6	± 0.4

Table 4: Table to show the peak intensity ratios where the G-band was fitted with two lorentzians and Peak 1 (shown in figure 24 parts c and d), G'-band is fitted with a single voigt and the D-band is fitted with a single Lorentzian. These are the results for the biology parameters where acquisition time is equal to 45s with a 50% filter.

the number of graphene layers in the sample [8]. These ratios can be compared with the literature to further understand and compare the quality of the graphene sample, which are shown in table 5. The average result for I_D/I_G is similar to that expected for CVD graphene, shown in table 5. That this result is >0 shows these are not a pristine graphene sample as expected. Although, it would be the ideal to have a complete pristine sheet of graphene, this is unachievable for the sizes of graphene sheets needed for biological applications, as previously discussed.

Graphene Type	FWHM for G' Band	I_D/I_G	$I_{G'}/I_G$	Reference
CVD	35	0.161	2.4	[65]
CVD	30	0.28	>3	[66]
CVD	33		2.7	[67]
CVD		0.05 - 0.3		[15]
CVD			>2	[17]
CVD			$\sim$3, $\sim$2.5	[16]
CVD			1.2	[68]
Suspended			3.9, 2.1	[69]
Exfoliation on SiO$_2$			6.1 $\pm$ 0.2	[70]
Exfoliation on SiO$_2$	17	0	3.4	[71]
Micromechanical Cleavage			3.2	[72]

Table 5: A table to show values of comparison of FWHM and peak intensity ratios taken from literature for graphene.

This section has successfully shown how to characterise CVD graphene sheets using various Raman Spectroscopy parameters, along with statistical analysis to understand it's inhomogenities. Understanding the inhomogenities of graphene as a substrate for biological applications is important to analyse the differences in cells lines when they are cultured on a substrate. The substrate must be homogenous so a subtraction of the substrate can be obtained to analyse the remain cell spectra. Obtaining a large number of measurements (n>100) shows statistical convergence and is promising to obtaining an average graphene spectra to subtract from P4E6 cell spectra later obtained in this thesis.

3.2 Raman Spectroscopy to Characterise Prostate Cancer Cell Lines

3.2.1 Data Taken Using CaF$_2$ as a Biological Substrate

Figure 32 shows all data of the P4E6 cells taken, with figure 33 showing the average of this data, where the grey shaded area is the the standard error in the mean envelope, calculated via Igor.

(a) Sample 1 Lower

(b) Sample 1 Upper
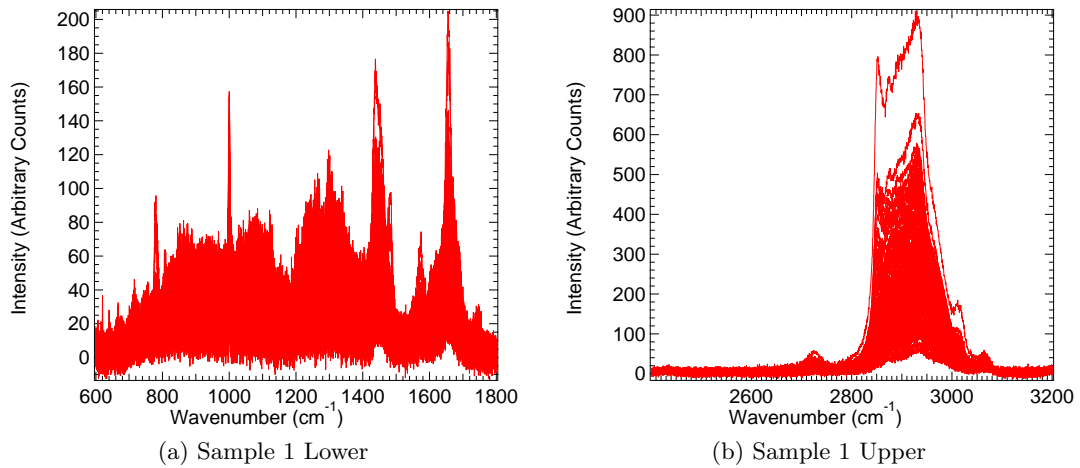
Figure 32: A figure to show all 145 data points taken of 29 seperate P4E6 cells, over 4 different samples with intensity in arbitrary counts plotted against wavenumber of the data taken across the fingerprint region. This spectra was taken using biology parameters with an acquisition time equal to 45s and a 50% filter.

There is a much weaker Raman signal for cells culture on CaF$_2$, compared to the overall intensity of graphene in section 3.1, which could lead to graphene swamping out the cell data when used as a substrate. For example, when the G' band is measured under the same instrument parameters as cells, it is measure at around 500a.u. Looking at figure 33, the most intense cell peak is around 270a.u., so the G' band is almost double that of the highest peak of cell data.
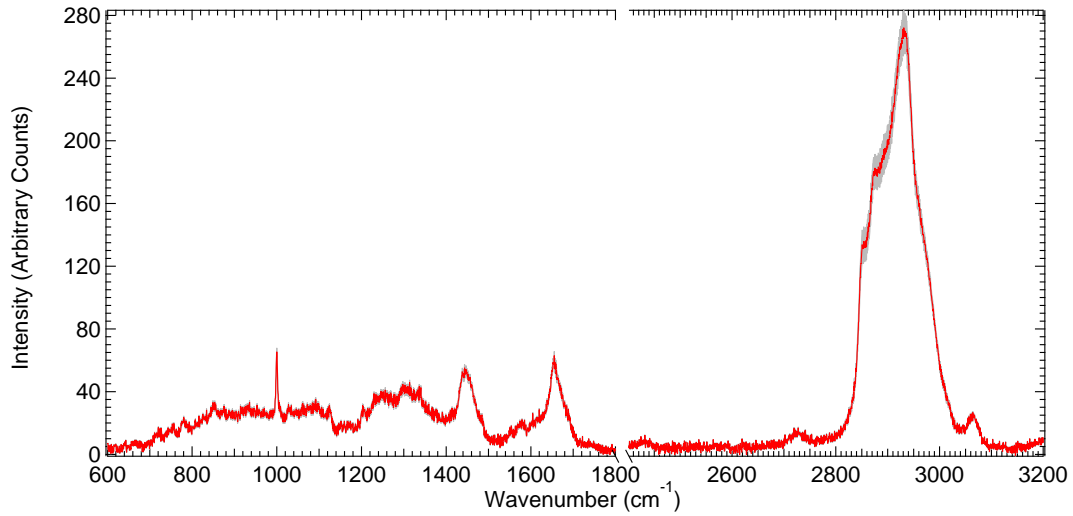
(a) P4E6 average across whole wavenumber range

Figure 33: A figure to show average intensity in arbitrary counts plotted against wavenumber of the Raman spectra data taken using a 532nm laser to analyse P4E6 cell lines. The data was taken across three different samples and an average calculated. Cells were chosen at random with five data spectra collected randomly across each cell. The red line represents the average of 145 spectra taken from cells chosen at random. The grey shaded area shows the average spectra with the standard error added or subtracted. All data was baseline subtracted using Raman Tool Set before the average spectra was calculated.

From these results, the peak location can be obtained by fitting the peaks with a Gaussian fit [73, 74, 75]. The peak positions found in the cell spectra when cultured on CaF_2 can be shown in table 6, which have an associated instrumental error of $\pm 3 cm^{-1}$.

These peaks were assigned their relative purpose, which was obtained from Movasaghi et. al [76].

The lower wavenumber results are very similar to expected from Crow et. al [44], shown previously in Figure 6. Unfortunately in this paper, there is no discussion on the higher wavenumber region which contains important information about the lipid and protein regions of the cell, and also does not use P4E6 cell lines.

However, Potcoava et. al [45] also looked at cancer cell lines using Raman spectroscopy.

55

It is difficult to make a direct comparison with this paper, as the method varied, with the main variation being the use of glass (MatTek 35 mm glass bottom dishes no. 1, poly-D-lysine coated) cover slips for cell culturing, where this thesis uses CaF_2 slides. However, there were some similar measures in peaks from this paper compared with this thesis. Comparing with table 6, Potcoava also measured peaks at $1125cm^{-1}$, $1655cm^{-1}$ (within $\pm 1cm^{-1}$ of $2874cm^{-1}$ measured in this thesis), $2873cm^{-1}$ (within $\pm 1cm^{-1}$ of $2874cm^{-1}$ measured in this thesis) and $2920cm^{-1}$ (within $\pm 2cm^{-1}$ of $2918cm^{-1}$ measured in this thesis).

Peak Location (cm^{-1})	Assignments	Reference
719	Lipids	[77]
780	DNA/RNA	[78]
826	DNA	[79]
851	Proteins (Single bond amino acide/polysaccharide stretching)	[80]
933	Proteins (Collagen, proline)	[81]
1000	Phenylalanine	[82]
1125	Proteins and Lipids	[81, 83, 84]
1204	Proteins (Collagen, Amide III), Phenylalanine	[85, 86, 87, 88]
1230	Proteins (Amide III)	[87]
1246	Proteins (Amide III)	[81]
1302	Proteins (Collagen, Amide III)	[89, 81, 83]
1337	DNA, Proteins, Lipids	[87, 83, 81]
1449	Proteins, Lipids	[90]
1553	Proteins	[89]
1575	DNA	[83]
1656	Lipids	[88]
2874	CH and CH$_2$ Stretching of Lipids and Proteins	[91]
2892	CH and CH$_2$ Stretching of Lipids and Proteins	[91]
2918	CH Stretching of Lipids and Protiens	[91]
2944	CH$_2$ Stretching	[91]
2955	CH$_3$ asymmetric stretching	[92]
2968	Lipids	[84]
3073	CH Stretching	[93]

Table 6: A table to show the peak positions and their assignment of the P4E6 sample that have been fitted to the average of the data collected within this thesis [76].

Figure 33 shows the cell convergence in increase intervals of 5 spectra, from 5 to 145 spectra. The cell data has much more variance at spectra lower than around 40 measurements, but starts to converge most around 90 spectra, where the standard error convergence lines are almost superimposed on one another from this number of spectra.

5 spectra were taken from each cell, across 29 cells over four samples. An average was taken to show the average across these samples, to give an overall picture of the P4E6 cell data taken in this thesis. Although data will change slightly from cell to cell within the same sample, especially within the lipid, protein and nucleic acid regions of the spectra, an average was calculated with along with statistical analysis including convergence tests. The variance within the average and the second order standard deviation also converges around the points of 90 spectra. This is important to have a fair and representative set of results of the P4E6 cell lines in order to understand their content.

Convergence shows confidence in the data and that an average calculated over 90 spectra gives a fair representation of the overall P4E6 data taken in this thesis, despite being over different samples.
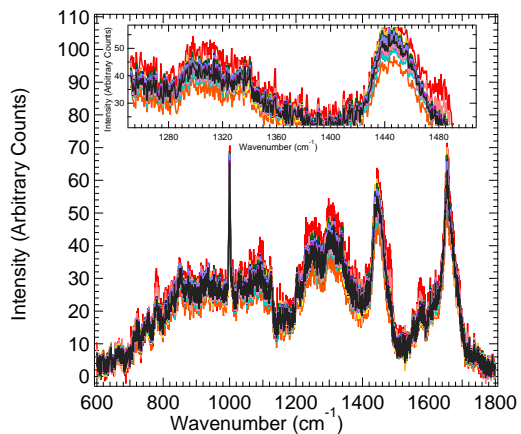
(a) Cell Average Convergence
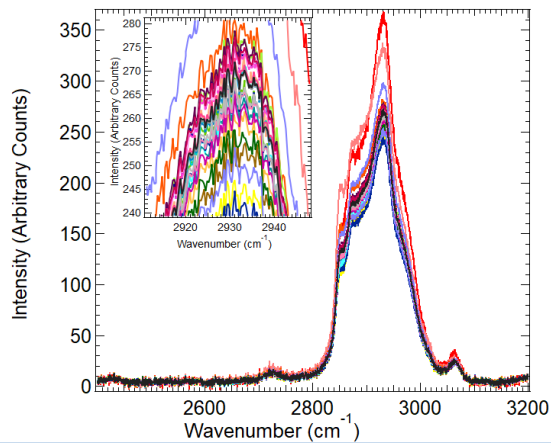
(b) Cell and Graphene Average Convergence
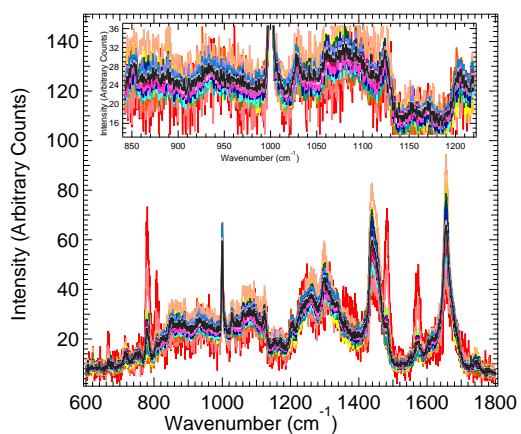
(c) Cell 2nd Order SD Convergence
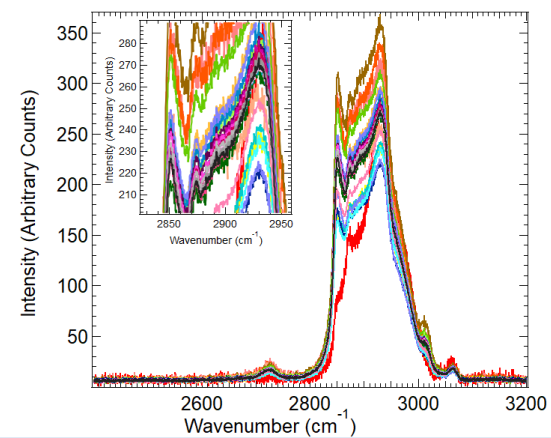
(d) Cell and Graphene 2nd Order SD Convergence
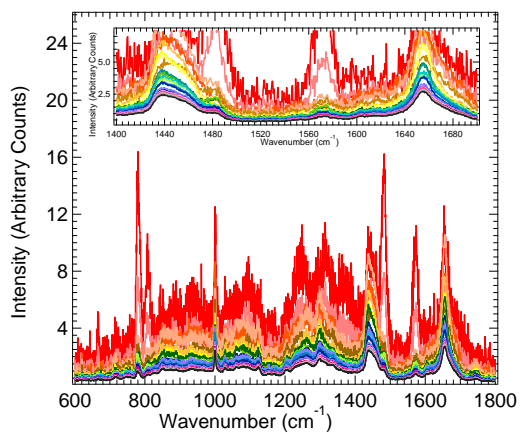
(e) Cell SE Convergence

(f) Cell and Graphene SE Convergence

59

—— 5 Spectra	
—— 10 Spectra	—— 80 Spectra
—— 15 Spectra	—— 85 Spectra
—— 20 Spectra	—— 90 Spectra
—— 25 Spectra	—— 95 Spectra
—— 30 Spectra	—— 100 Spectra
—— 35 Spectra	—— 105 Spectra
—— 40 Spectra	—— 110 Spectra
—— 45 Spectra	—— 115 Spectra
—— 50 Spectra	—— 120 Spectra
—— 55 Spectra	—— 125 Spectra
—— 60 Spectra	—— 130 Spectra
—— 65 Spectra	—— 135 Spectra
—— 70 Spectra	—— 140 Spectra
—— 75 Spectra	—— 145 Spectra
(g)	(h)
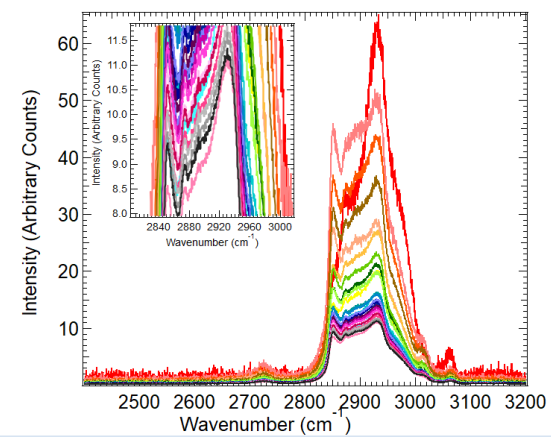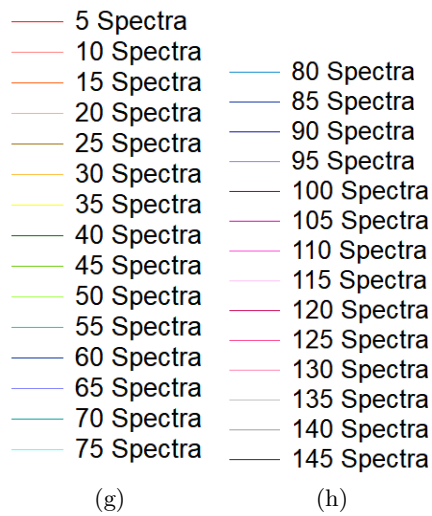
Figure 33: A figure to show the convergence tests calculated for cells cultured on calcium fluoride slides with the key to show the number of spectra.

It is important to note that having a statistically reliable spectra of P4E6 cell lines on a CaF_2 substrate will help to better understand the effects of using a graphene substrate will have upon the cell lines. This important for the next section of this thesis where a comparison of graphene, and cells cultured on a CaF_2 substrate will take place.

3.2.2 Data Taken Using CVD Graphene as a Biological Substrate

As previously discussed, graphene has a much greater Raman signal than that of the P4E6 cells used in this thesis. Figure 34 shows the average spectra of the fingerprint region, for cells cultured on graphene. This spectra was obtained over the same region as the cells in section 3.2.1, however the background from the graphene substrate swamps the biological data.
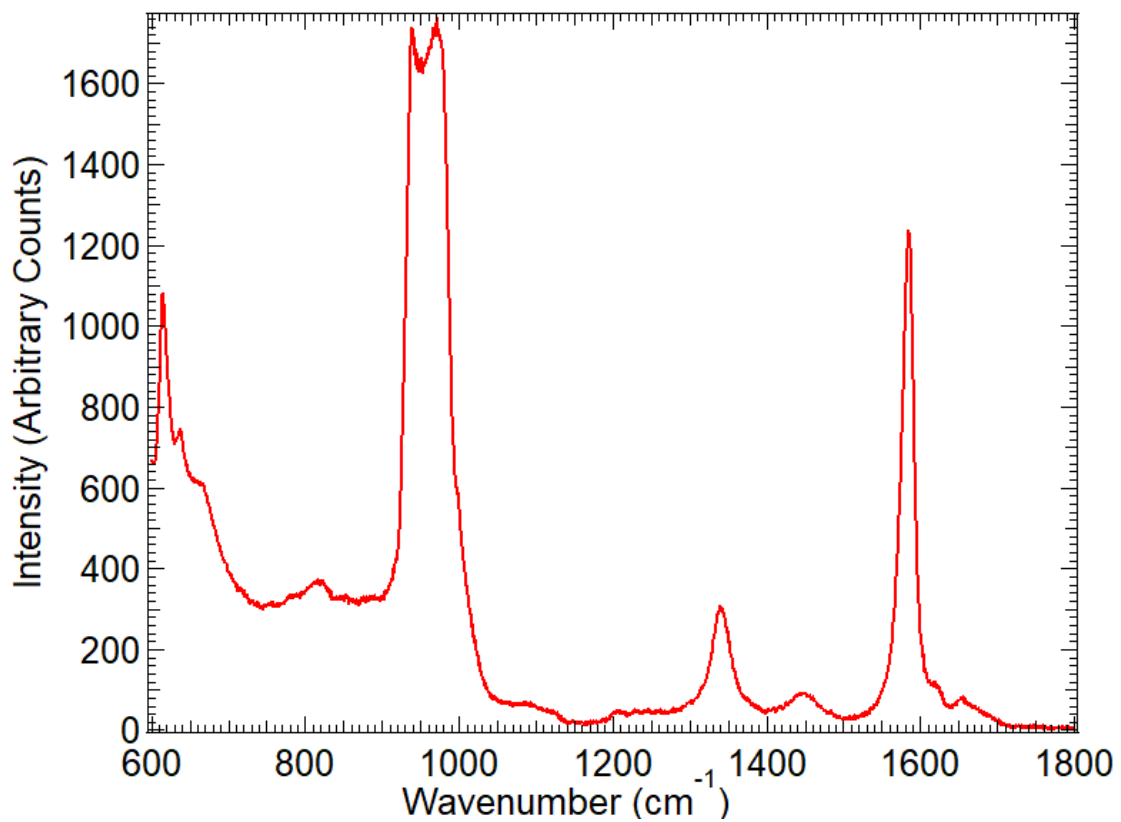
Figure 34: A figure to show the full average fingerprint region $(600 - 1800$ cm$^{-1})$ of P4E6 cells cultured on CVD graphene substrates.

The swamping of this biological signal is particularly noticable in the $600 - 1200$ cm^{-1} region and so for this section, the lower fingerprint region will be the same as

section 3.1.

As discussed when the P4E6 cell lines were cultured on CaF_2, the convergence happened around the 40 spectra point, with the cells being converged from 90 spectra upwards. Therefore, 95 spectra have been obtained of cells cultured on graphene.

The final average of all 95 spectra is outlined in Figure 35, with (a) showing the fingerprint region and (b) showing the high wavenumber region.
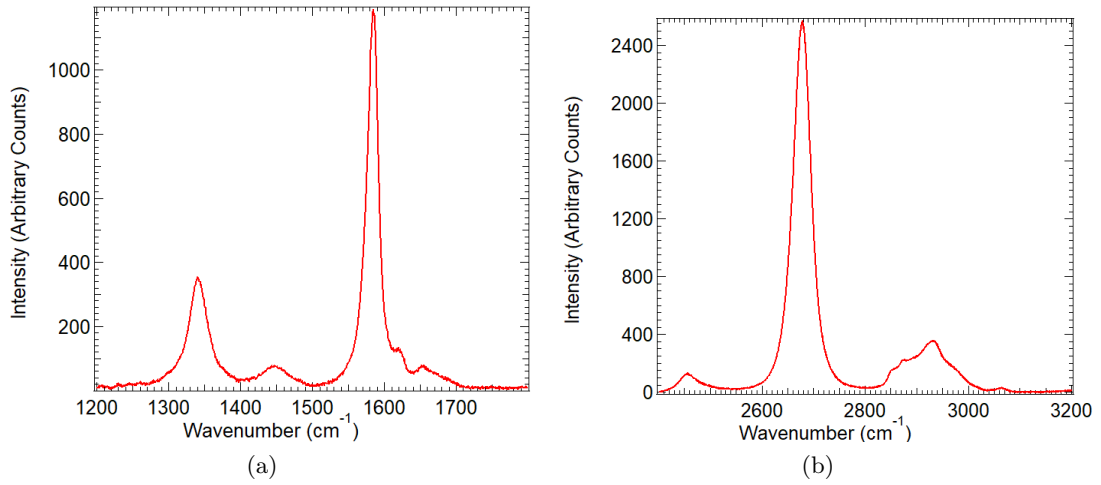
Figure 35: A figure to show the average spectra in the fingerprint region (a) and the high wavenumber region (b) of P4E6 cells cultured on CVD graphene.

As the cell data has been swamped in the lower region, it is best to look at the higher wavenumber region for the convergence tests (Fig 36).

The cell region ($2800 - 3050cm^{-1}$) of the spectra in figure 36 shows convergence of standard error in the mean at around 75 spectra, and hence shows enough spectra were obtained to have a fair statistical results.

The variance in results for the same cell region converges in the average and the second order standard deviation at around 50 spectra.
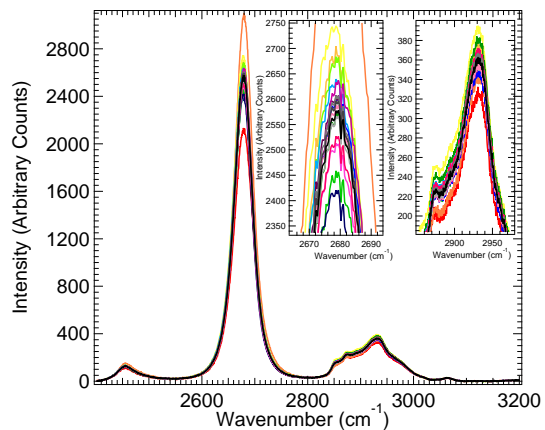
(a) Cell and Graphene Average Convergence
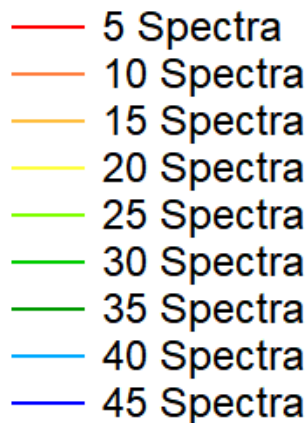
(b) Convergence Key
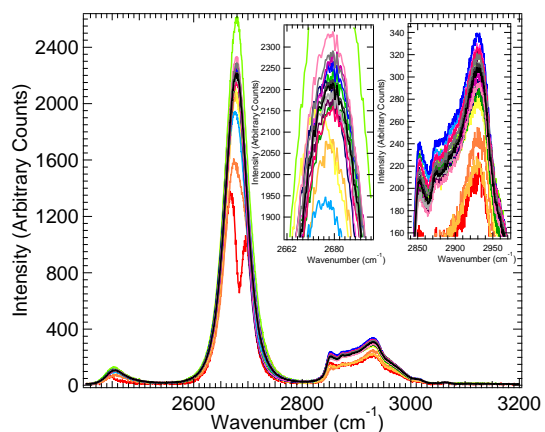
(c) Cell and Graphene 2nd Order SD Convergence
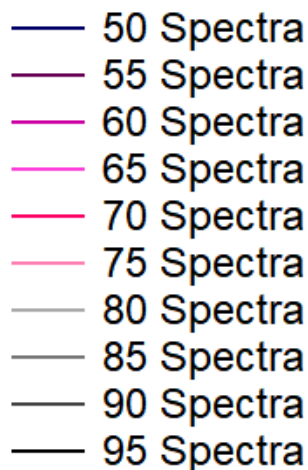
(d) Convergence Key
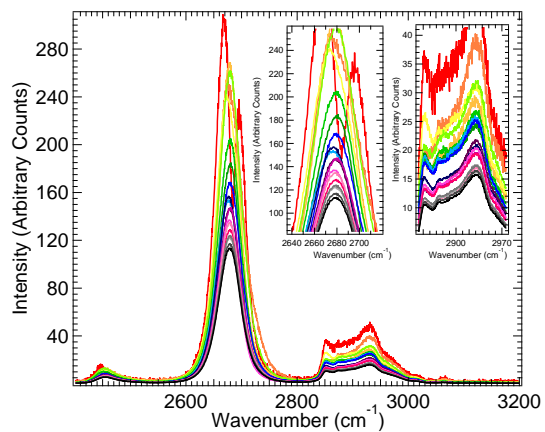
(e) Cell and Graphene SE Convergence

Figure 36: A figure to show the convergence tests calculated for cells cultured on graphene.

Despite the cell data converging at this point, it takes a larger number of graphene spectra to converge in this data set. This is due to there being an average across all three samples being taken, rather than 120 of each graphene sample as previously described in section 3.1.

The best way to have statistical confidence in the results would be to take 120 measurements of cells on each sample of graphene but this is unachievable. The main difficulties with obtaining a large sample set is the quality of the dried sample. The dried sample cannot be used for a large period of time, and is only in its optimal condition in the first 24 hours of being dried. Each spectra takes around 6 minutes to obtain and hence is difficult to obtain 120 spectra in one sitting. Therefore, 3 samples had to be cultured on graphene samples 1, 2 and 4 and an average taken.

Another way to understand the graphene now it has been cultured with P4E6 cells, can be to revisit the PIR (Fig 37).

In figure 37, there are 3 comparisons. Purple shows the results averaged across the three samples used before they were used as a biological substrate, compared to after the cells were cultured. In red, shows the cells without the defects removed, to show this obtains a higher I_D/I_G ratio. Blue shows once these defects are removed. Defected spectra were decided based on the data results, with an example shown in figure 38. The decided defected spectra were then removed from the data set, before calculating the average spectra shown in figures 34, 35, 36 and the blue data set result shown in figure 37.
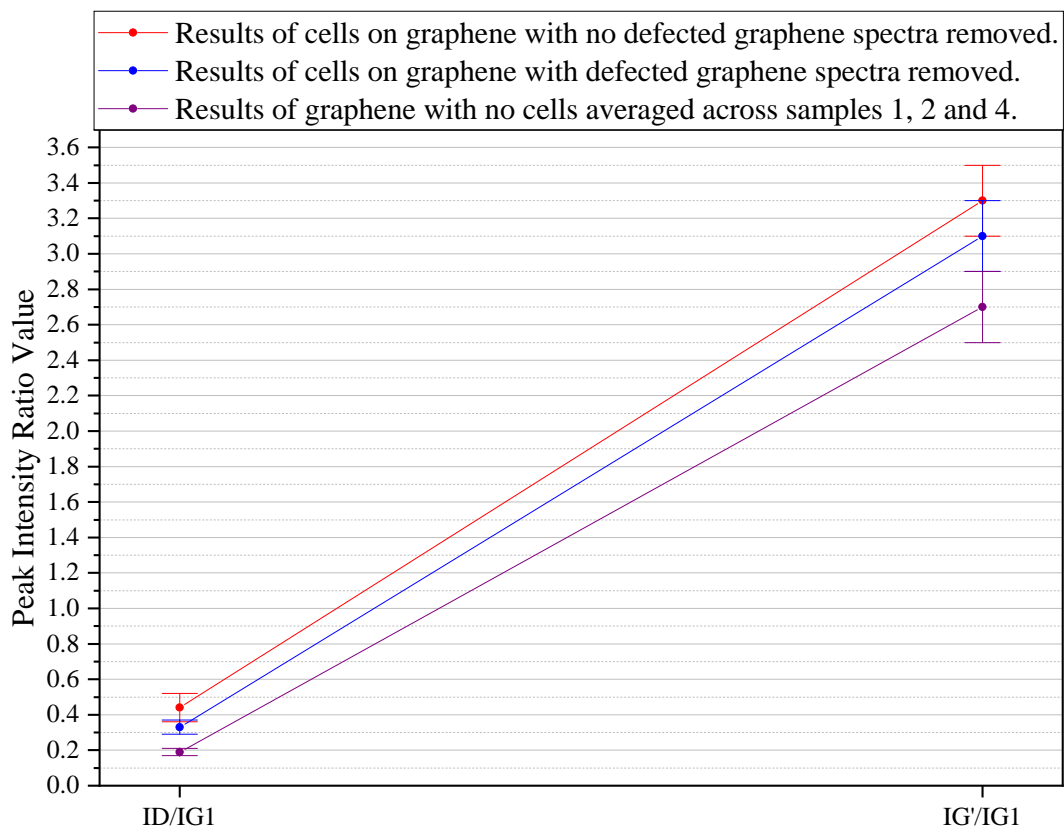
Figure 37: A figure to show the Peak Intensity Ratio for cells on graphene compared with the average values taken across samples 1, 2 and 4.
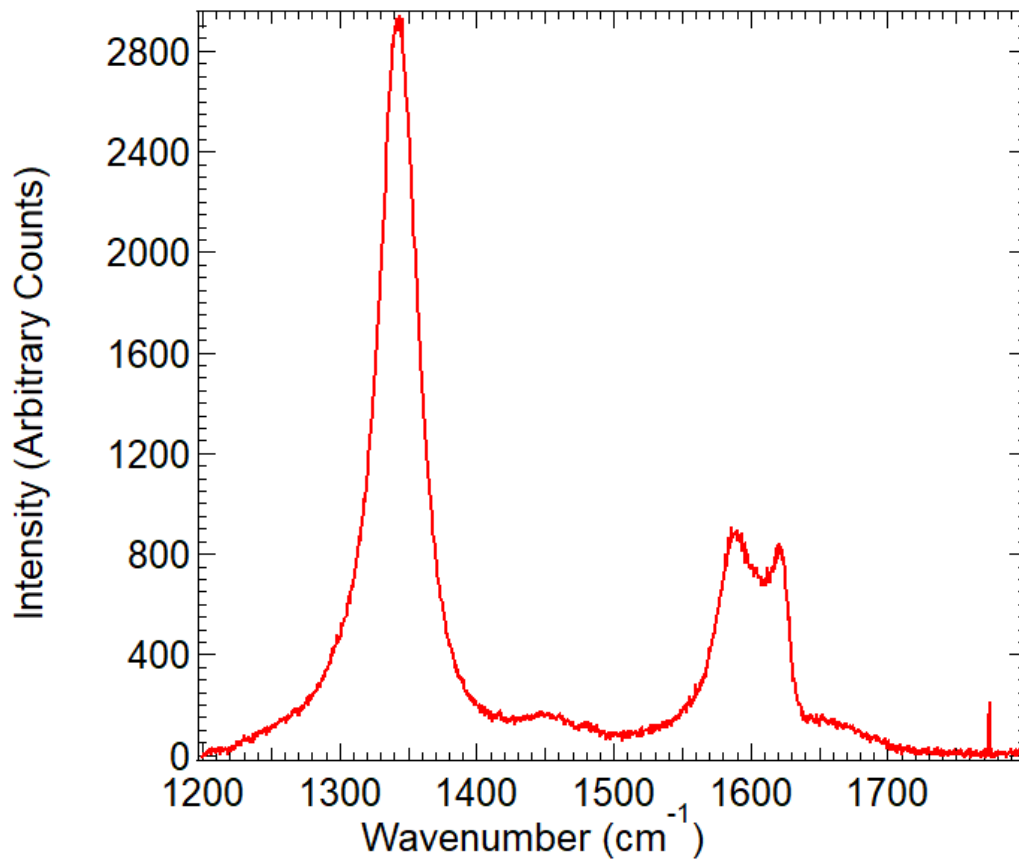
Figure 38: A figure to show a single spectra of defected graphene.

These defects can be shown in figure 38, which is not the same as the spectra expected. It shows a splitting of the G-band and an increase in intensity of the D-band. A comparison of the average spectra before the defects were removed, and after they were removed can be shown in figure 39.
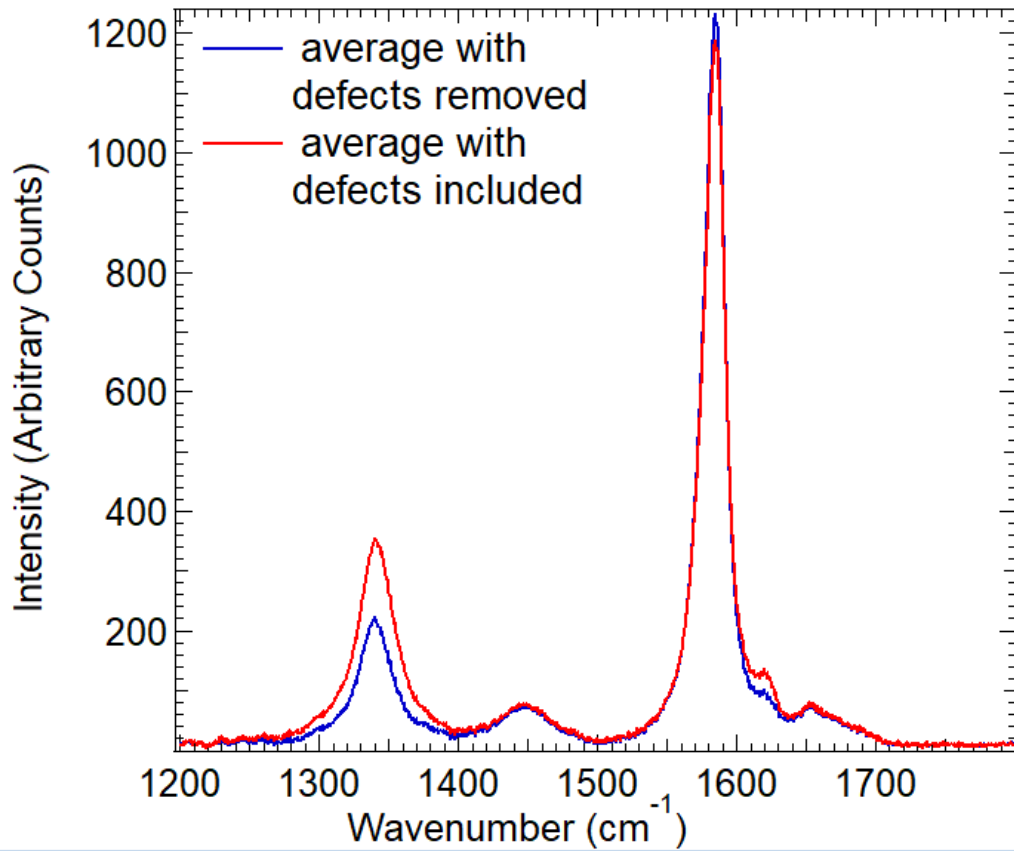
Figure 39: A figure to show the average before and after the defected samples were removed.

There is a larger I_D/I_G value when the biology has been cultured on the graphene, even after the defected spectra have been removed. This raises many uncertainties within the results of this section. This could mean that the process of culturing the biology is effecting the graphene and hence damaging it. This could also be that the biology fixes to the defected regions instead of the graphene. This could also be down to the hydrophobic aspects of the material as the cells are cultured in liquid [94].

Results for all samples of graphene markers when P4E6 is cultured on graphene				
Peak	Location (cm^{-1})	Error	FWHM (cm^{-1})	Error
D	1340.3	± 0.1	27.7	± 0.4
G_0	1579.89	± 0.03	17.7	± 0.2
G_1	1587.03	± 0.03	11.7	± 0.1
G'	2678.27	± 0.02	41.0	± 0.3
Peak Intensity Ratios				
Ratio		Peak Ratio Value		Error
I_D/I_{G_1}		0.33		± 0.04
$I_{G'}/I_{G_1}$		3.1		± 0.4

Table 7: Table to show the peak intensity ratios of graphene markers when P4E6 has been cultured on the samples. The G-band was fitted with two lorentzians and Peak 1 (shown in figure 24 parts c and d), G'-band is fitted with a single voigt and the D-band is fitted with a single Lorentzian. These are the results for the biology parameters where acquisition time is equal to 45s with a 50% filter.

Table 7 shows the graphene peak intensity ratios when cells have been cultured on them as a substrate. The I_D/I_G is much greater than it was before it was used as a substrate for biology, indicating that there is a greater defect associated when the biology has been cultured. Again, as discussed before this could be due to the lower amount of measurements taken. It could also be that the measurements, which are performed at random, could just have contained more defected spectra.

Difference in Results Graphene Samples Before and After Biology Was Cultured		
Peak	Location (cm^{-1})	FWHM (cm^{-1})
D	1.0	1.5
G	4.9	2.4
G'	0.4	3.3
Peak Intensity Ratios		
Ratio	Peak Ratio Value	
I_D/I_{G_1}	0.16	
$I_{G'}/I_{G_1}$	0.5	

Table 8: Table to show the difference in the average across 1, 2 4 samples of graphene taken with a 50% filter, 45s acq. time before biology was cultured on them, and then average of sample 1, 2 and 4 after biology was cultured on them.

Table 8 shows the difference in the results for the location, FWHM and PIR on graphene before and after it was cultured with biology. This shows a large difference in the results for the PIR, with I_D/I_G being around double to before the biology was cultured on the substrate.

These results are also larger than expected compared to the literature values outlined in table 5, with the largest I_D/I_G found in the literature equaling 0.3.

The PIR value for $I_{G'}/I_G$ is greater than most expected for CVD graphene and more in-line with graphene obtained through other methods such as exfoliation or micro-mechanical cleavage, although Kalbec et. al state $I_{G'}/I_G > 3$ [66].

This continues to confirm the variations in CVD graphene, especially as a substrate for biological applications.

Principle component analysis can also be used to further understand the variation in results for a direct comparison between the two substrates, previously being used to group data sets [95].

● Cell Lines Cultured on a Calcium Fluoride Slide
● Cell Lines Cultured on a Graphene Substrate
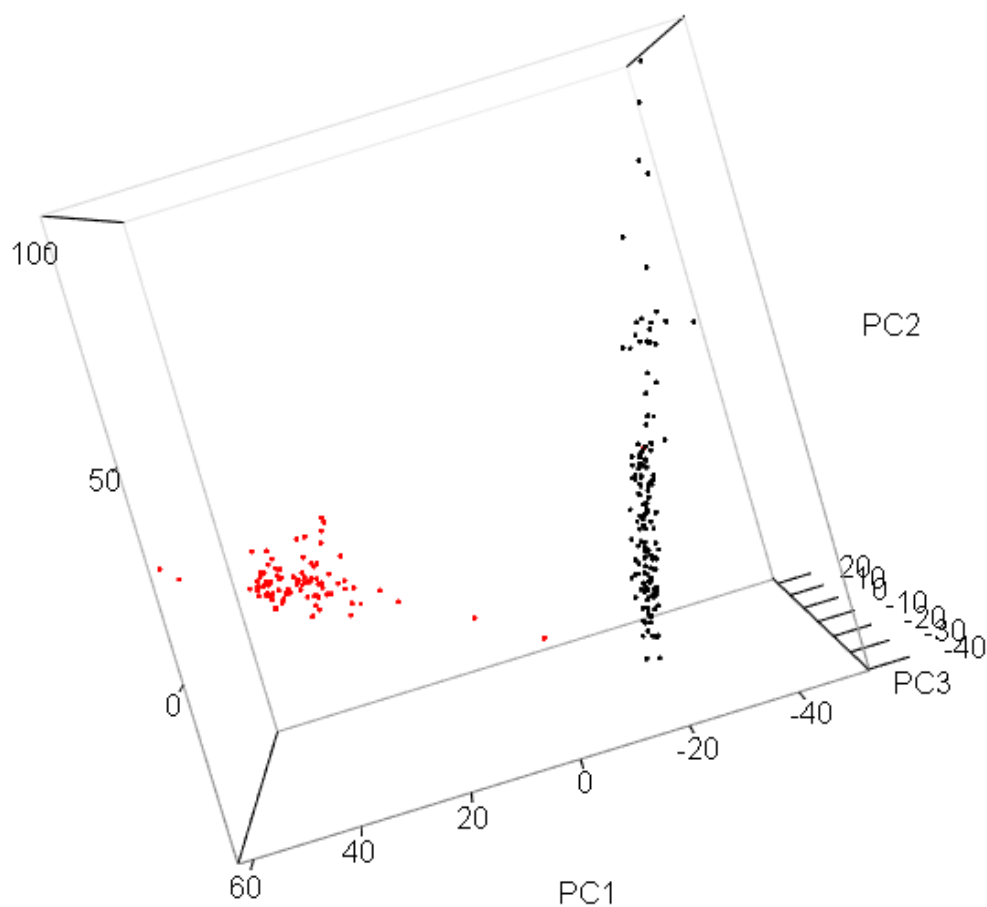
Figure 40: A figure to show principal component analysis of P4E6 cell lines cultured on calcium fluoride substrates (black) and P4E6 cell lines cultured on graphene substrates (red).

Figure 40 shows the grouping of two data sets, of cells cultured on graphene compared with their culture on CaF_2. This shows clear separation between the results and hence shows that the graphene is effecting the overall spectra to allow it to be grouped separately.
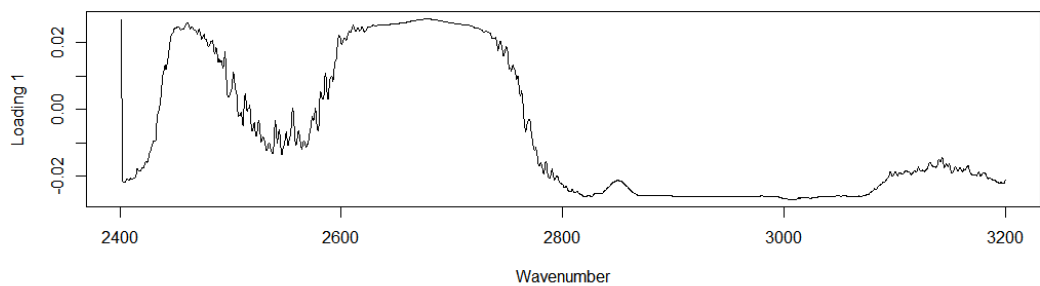
(a) Loading 1
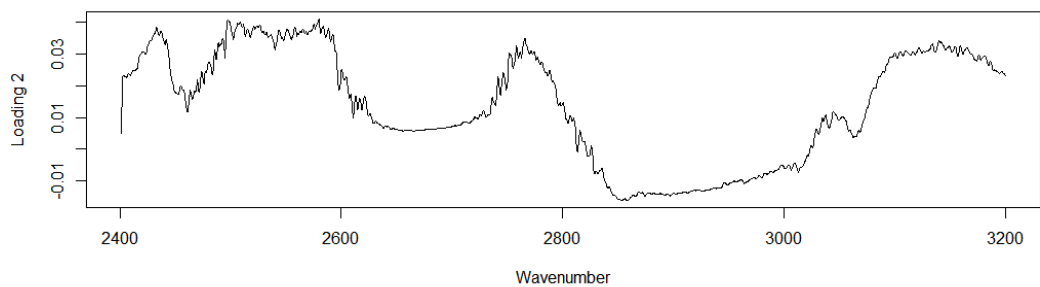
(b) Loading 2
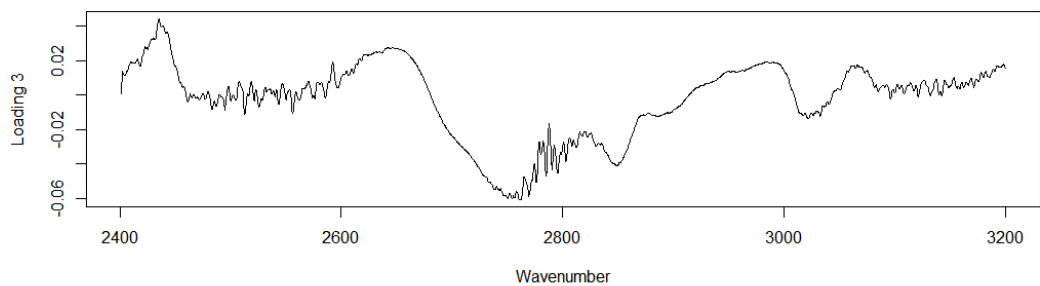
(c) Loading 3

Figure 41: A figure to show the first three PCA loading tests calculated for cells cultured on graphene compared with the CaF$_2$ substrate.

The first three loadings show much variation in the two data sets (fig 41). The 2400 – 2800 cm^{-1} region is expected to have a large variation as this is where the graphene

71

swamps the biological data and hence will show a large variance. Howevere, in the 2800 - 3000 cm^{-1} region, the cell data comes through and this can be analysed.

For graphene to be used as a substrate for biology, it should not have an effect on the results. However, the first three loadings show a variance in results, particularly in the 2890cm^{-1} peak.

This variation can be further shown in figure 42, where a direct subtraction of the results on two substrates was performed. The data was first normalised to account for the differences in relative intensities due to the varied substrates.
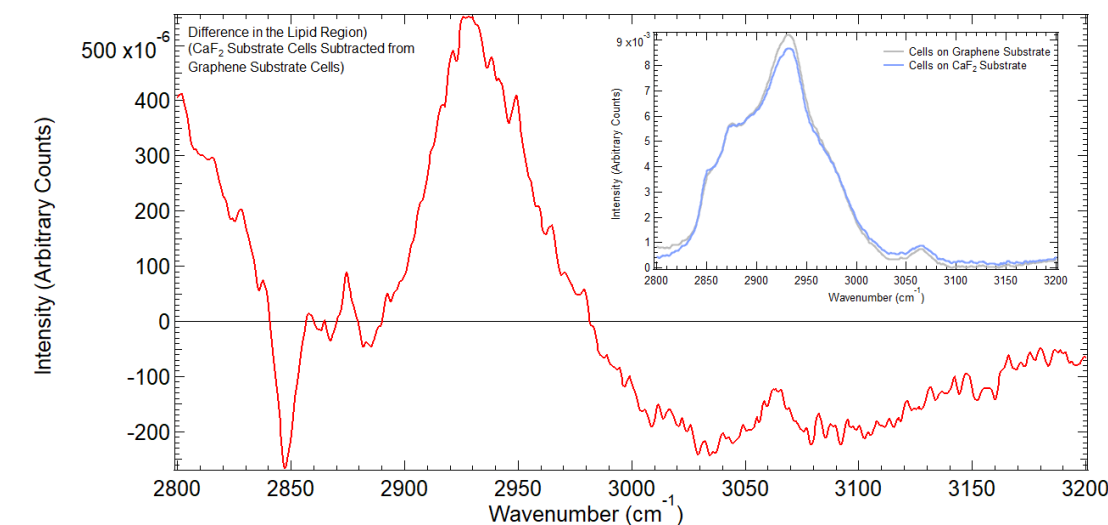
Figure 42: A figure to show the difference in the lipid and protein region of the cells when cultures on different substrates.

The red line shows the difference in the average spectra obtained, with the grey and the blue lines showing the original average.

This again shows a large variation in the results obtained from the biology. It is important to have a substrate with little variation for many reasons.

Firstly to understand that the substrate is not effecting the results or the way in which the cells are growing on the substrate and that the substrate is therefore not effecting the cells growth.

Secondly, in order to understand the cell's spectra and be able to perform proper structured analyses, it is best to have a substrate with limited variation so that it can be easily subtracted away from the cell data.

Graphene obtained through chemical vapour deposition has shown great inhomogenities throughout this section of the thesis, through each singular samples and comparatively across all separate samples.

4 Conclusion

This thesis has outlined the importance and need for a fast diagnostic method for prostate cancer cell detection and how a Raman spectrometer could be used to achieve this. Firstly this thesis discusses the pros and cons of graphene as a substrate for cell analyses through Raman spectroscopy. CVD graphene has been used as it is cheap, easy to obtain and can be used for a relatively large area compared to a pristine sheet of graphene. All these factors are important within a medical application, as a diagnosis method will need to be both cost effective and easily available.

This thesis outlined how to correctly characterise graphene using a Raman spectrometer and the various parameters that can be used. The variations between graphene samples were shown and how a difference in parameters can also effect results.

It was shown that in order to obtain statistical convergence of the graphene samples, around 90 spectra are needed.

The PIR were also obtained and were as expected from the literature. It was found that $I_D/I_G = 0.17 \pm 0.05$ for the average across all four samples when measured using biology parameters. $I_{G'}/I_G$ was also calculated to be 2.6 ± 0.4, which is also as expected within the literature. This, along with the values obtained for the location and FWHM shows the correct characterisation of CVD graphene.

Following on from this, P4E6 cell lines were characterised under the same conditions using CaF_2 as a substrate to obtain an average spectra. The use of CaF_2 is advantageous as it has no background in the range analysed in this thesis, so therefore does not effect the results. This average was calculated across 145 data points. Peak fittings to this spectra allowed a comparison to the literature to show the correct characterisation of P4E6. This data set did not require a lot of preprocessing due to the CaF_2 substrate having no effect on the analysed part of the spectra. Convergence tests ran on this data showed that around 90 spectra are needed to have statistical confidence in the data set.

This lead onto the use of graphene as a biological substrate for cancer detection using Raman Spectroscopy.

Firstly, it was shown that graphene can swamp a lot of vital information about the cell's spectra, particularly in the $600 - 1200$ cm^{-1} region, which has been shown to include the important 780cm^{-1} DNA peak, and 1000cm^{-1} phenylalanine peak, as well as information on lipids and proteins. Within the lower fingerprint region, it is difficult to distinguish what is cell data due to the large graphene intensity.

However, within the higher wavenumber region, the $2800 - 3050$ cm^{-1} lipid and protein region is clearly distinguishable.

A PIR was calculated to be I$_D$/I$_G = 0.33 \pm 0.04$, meaning there was an increase in this value when the P4E6 cell lines were characterised on graphene. This could be due to the cells measured being on defected parts of the graphene.

To conclude, it is best that CVD graphene is not used as a substrate for cell cultures being analysed with Raman spectroscopy due to its inhomogenity, however the use of a CaF$_2$ slide has shown that a Raman insturment can be used to characterise P4E6 cells and therefore, be used as a diagnostic method for prostate cancer.

Future Works

For future works, a comparison of P4E6 to non-cancerous cells such as PNT2-C2 could be looked at. Also, a sample of graphene obtained through a different method (ie, micromechanical cleavage) could be used.

It would also be advantageous to investigate the effects of the media used to grow the cells, and the material used to wash the cells had on the graphene, by adding these to the substrate and investigate how the Raman signal changes through similar analyses methods outlined in this thesis. This will truly answer if these various solutions were responsible for the defects outlined, and if so, which solutions were responsible.

It would be useful to make a direct comparison, perhaps through PCA and loading, on the differentiation between each individual cell spectra, to see if this would have a direct effect on the convergence test. This is because individual cells can differ in their make-up, and this could effect the results when calculation an average.

References

[1] A. K. Geim and K. S. Novoselov, "The rise of graphene," in *Nanoscience and Technology: A Collection of Reviews from Nature Journals*, pp. 11–19, World Scientific, 2010.

[2] M. Rahmani, R. Ismail, M. T. Ahmadi, M. J. Kiani, M. Saeidmanesh, F. Karimi, E. Akbari, and K. Rahmani, "The effect of bilayer graphene nanoribbon geometry on schottky-barrier diode performance," *Journal of Nanomaterials*, vol. 2013, p. 3, 2013.

[3] K. S. Novoselov, A. K. Geim, S. V. Morozov, D. Jiang, Y. Zhang, S. V. Dubonos, I. V. Grigorieva, and A. A. Firsov, "Electric field effect in atomically thin carbon films," *science*, vol. 306, no. 5696, pp. 666–669, 2004.

[4] Y. Wang, S. W. Tong, X. F. Xu, B. Özyilmaz, and K. P. Loh, "Interface engineering of layer-by-layer stacked graphene anodes for high-performance organic solar cells," *Advanced materials*, vol. 23, no. 13, pp. 1514–1518, 2011.

[5] R. Kurapati, K. Kostarelos, M. Prato, and A. Bianco, "Biomedical uses for 2d materials beyond graphene: current advances and challenges ahead," *Advanced Materials*, vol. 28, no. 29, pp. 6052–6074, 2016.

[6] M. J. Webb, P. Palmgren, P. Pal, O. Karis, and H. Grennberg, "A simple method to produce almost perfect graphene on highly oriented pyrolytic graphite," *Carbon*, vol. 49, no. 10, pp. 3242–3249, 2011.

[7] K. S. Kim, Y. Zhao, H. Jang, S. Y. Lee, J. M. Kim, K. S. Kim, J.-H. Ahn, P. Kim, J.-Y. Choi, and B. H. Hong, "Large-scale pattern growth of graphene films for stretchable transparent electrodes," *nature*, vol. 457, no. 7230, p. 706, 2009.

[8] A. Reina, X. Jia, J. Ho, D. Nezich, H. Son, V. Bulovic, M. S. Dresselhaus, and J. Kong, "Large area, few-layer graphene films on arbitrary substrates by chemical vapor deposition," *Nano letters*, vol. 9, no. 1, pp. 30–35, 2008.

[9] A. N. Obraztsov, "Chemical vapour deposition: making graphene on a large scale," *Nature nanotechnology*, vol. 4, no. 4, p. 212, 2009.

[10] S. Some, Y. Kim, Y. Yoon, H. Yoo, S. Lee, Y. Park, and H. Lee, "High-quality reduced graphene oxide by a dual-function chemical reduction and healing process," *Scientific reports*, vol. 3, p. 1929, 2013.

[11] K. V. Emtsev, A. Bostwick, K. Horn, J. Jobst, G. L. Kellogg, L. Ley, J. L. McChesney, T. Ohta, S. A. Reshanov, J. Röhrl, *et al.*, "Towards wafer-size graphene layers by atmospheric pressure graphitization of silicon carbide," *Nature materials*, vol. 8, no. 3, p. 203, 2009.

[12] Graphene Supermarket, "Graphene supplier." `https://graphene-supermarket.com/Two-Layers-of-CVD-Graphene-Film-On-SiO2-Si-Wafer-4-pack.html`.

[13] A. C. Ferrari and D. M. Basko, "Raman spectroscopy as a versatile tool for studying the properties of graphene," *Nature nanotechnology*, vol. 8, no. 4, p. 235, 2013.

[14] A. C. Ferrari, J. Meyer, V. Scardaci, C. Casiraghi, M. Lazzeri, F. Mauri, S. Piscanec, D. Jiang, K. Novoselov, S. Roth, *et al.*, "Raman spectrum of graphene and graphene layers," *Physical review letters*, vol. 97, no. 18, p. 187401, 2006.

[15] L. Malard, M. Pimenta, G. Dresselhaus, and M. Dresselhaus, "Raman spectroscopy in graphene," *Physics Reports*, vol. 473, no. 5-6, pp. 51–87, 2009.

[16] S. M. Hussein, I. F. Crowe, N. Clark, M. Milosevic, A. Vijayaraghavan, F. Y. Gardes, G. Z. Mashanovich, and M. P. Halsall, "Raman mapping analysis of graphene-

integrated silicon micro-ring resonators," *Nanoscale research letters*, vol. 12, no. 1, p. 600, 2017.

[17] A. Matsubayashi, Z. Zhang, J. U. Lee, and V. P. LaBella, "Microstructure fabrication process induced modulations in cvd graphene," *AIP Advances*, vol. 4, no. 12, p. 127143, 2014.

[18] A. C. Neto, F. Guinea, N. M. Peres, K. S. Novoselov, and A. K. Geim, "The electronic properties of graphene," *Reviews of modern physics*, vol. 81, no. 1, p. 109, 2009.

[19] G. Aus, J. Hugosson, and L. Norlen, "Long-term survival and mortality in prostate cancer treated with noncurative intent," *The Journal of urology*, vol. 154, no. 2, pp. 460–465, 1995.

[20] Prostate Cancer UK, "Prostate cancer uk website." `https://prostatecanceruk.org/`. [Online; accessed 18/06/2019].

[21] Cancer Research UK, "Cancer statistics 2016." `https://www.cancerresearchuk.org/health-professional/cancer-statistics/incidence/`, 2016. [Online; accessed 05/12/2019].

[22] G. Bartsch, W. Horninger, H. Klocker, A. Reissigl, W. Oberaigner, D. Schönitzer, G. Severi, C. Robertson, P. Boyle, *et al.*, "Prostate cancer mortality after introduction of prostate-specific antigen mass screening in the federal state of tyrol, austria," *Urology*, vol. 58, no. 3, pp. 417–424, 2001.

[23] J. S. Palmgren, S. S. Karavadia, and M. R. Wakefield, "Unusual and underappreciated: small cell carcinoma of the prostate," vol. 34, no. 1, pp. 22–29, 2007.

[24] L. Dickinson, H. U. Ahmed, C. Allen, J. O. Barentsz, B. Carey, J. J. Futterer, S. W. Heijmink, P. J. Hoskin, A. Kirkham, A. R. Padhani, *et al.*, "Magnetic resonance

imaging for the detection, localisation, and characterisation of prostate cancer: recommendations from a european consensus meeting," *European urology*, vol. 59, no. 4, pp. 477–494, 2011.

[25] D. Beyersdorff, K. Taymoorian, T. Knosel, D. Schnorr, R. Felix, B. Hamm, and H. Bruhn, "Mri of prostate cancer at 1.5 and 3.0 t: comparison of image quality in tumor detection and staging," *American Journal of Roentgenology*, vol. 185, no. 5, pp. 1214–1220, 2005.

[26] T. Dill, "Contraindications to magnetic resonance imaging," *Heart*, vol. 94, no. 7, pp. 943–948, 2008.

[27] B. Turkbey, P. A. Pinto, and P. L. Choyke, "Imaging techniques for prostate cancer: implications for focal therapy," *Nature Reviews Urology*, vol. 6, no. 4, p. 191, 2009.

[28] M. Golimbu, P. Morales, S. Al-Askari, and Y. Shulman, "Cat scanning in staging of prostatic cancer," *Urology*, vol. 18, no. 3, pp. 305–308, 1981.

[29] A. Afshar-Oromieh, E. Avtzi, F. L. Giesel, T. Holland-Letz, H. G. Linhart, M. Eder, M. Eisenhut, S. Boxler, B. A. Hadaschik, C. Kratochwil, *et al.*, "The diagnostic value of pet/ct imaging with the 68 ga-labelled psma ligand hbed-cc in the diagnosis of recurrent prostate cancer," *European journal of nuclear medicine and molecular imaging*, vol. 42, no. 2, pp. 197–209, 2015.

[30] E. C. Lin, "Radiation risk from medical imaging," vol. 85, no. 12, pp. 1142–1146, 2010.

[31] Prostate Conditions Education Council, "Gleason score information." https://www.prostateconditions.org/about-prostate-conditions/prostate-cancer/newly-diagnosed/gleason-score. [Online; accessed 13/06/2019].

[32] J. I. Epstein, M. J. Zelefsky, D. D. Sjoberg, J. B. Nelson, L. Egevad, C. Magi-Galluzzi, A. J. Vickers, A. V. Parwani, V. E. Reuter, S. W. Fine, *et al.*, "A contemporary prostate cancer grading system: a validated alternative to the gleason score," *European urology*, vol. 69, no. 3, pp. 428–435, 2016.

[33] P. Narayan, V. Gajendran, S. P. Taylor, A. Tewari, J. C. Presti Jr, R. Leidich, R. Lo, K. Palmer, K. Shinohara, and J. t Spaulding, "The role of transrectal ultrasound-guided biopsy-based staging, preoperative serum prostate-specific antigen, and biopsy gleason score in prediction of final pathologic diagnosis in prostate cancer," *Urology*, vol. 46, no. 2, pp. 205–212, 1995.

[34] N. J. Maitland, C. A. Macintosh, J. Hall, M. Sharrard, G. Quinn, and S. Lang, "In vitro models to study cellular differentiation and function in human prostate cancers," *Radiation research*, vol. 155, no. 1, pp. 133–142, 2001.

[35] G. Puppels, F. De Mul, C. Otto, J. Greve, M. Robert-Nicoud, D. Arndt-Jovin, and T. Jovin, "Studying single living cells and chromosomes by confocal raman microspectroscopy," *Nature*, vol. 347, no. 6290, p. 301, 1990.

[36] C. Kallaway, L. M. Almond, H. Barr, J. Wood, J. Hutchings, C. Kendall, and N. Stone, "Advances in the clinical application of raman spectroscopy for cancer diagnostics," *Photodiagnosis and photodynamic therapy*, vol. 10, no. 3, pp. 207–219, 2013.

[37] H. Lui, J. Zhao, D. I. McLean, and H. Zeng, "Real-time raman spectroscopy for in vivo skin cancer diagnosis," *Cancer research*, pp. canres–4061, 2012.

[38] A. S. Haka, K. E. Shafer-Peltier, M. Fitzmaurice, J. Crowe, R. R. Dasari, and M. S. Feld, "Diagnosing breast cancer by using raman spectroscopy," *Proceedings of the National Academy of Sciences*, vol. 102, no. 35, pp. 12371–12376, 2005.

[39] D. Lin, S. Feng, J. Pan, Y. Chen, J. Lin, G. Chen, S. Xie, H. Zeng, and R. Chen, "Colorectal cancer detection by gold nanoparticle based surface-enhanced raman spectroscopy of blood serum and statistical analysis," *Optics express*, vol. 19, no. 14, pp. 13565–13577, 2011.

[40] A. Mahadevan-Jansen, M. F. Mitchell, N. Ramanujamf, A. Malpica, S. Thomsen, U. Utzinger, and R. Richards-Kortumt, "Near-infrared raman spectroscopy for in vitro detection of cervical precancers," *Photochemistry and photobiology*, vol. 68, no. 1, pp. 123–132, 1998.

[41] Y. Zhou, C.-H. Liu, Y. Sun, Y. Pu, S. Boydston-White, Y. Liu, and R. R. Alfano, "Human brain cancer studied by resonance raman spectroscopy," *Journal of biomedical optics*, vol. 17, no. 11, p. 116021, 2012.

[42] C.-H. Liu, Y. Zhou, Y. Sun, J. Li, L. Zhou, S. Boydston-White, V. Masilamani, K. Zhu, Y. Pu, and R. Alfano, "Resonance raman and raman spectroscopy for breast cancer detection," *Technology in cancer research & treatment*, vol. 12, no. 4, pp. 371–382, 2013.

[43] L. Mavarani, D. Petersen, S. F. El-Mashtoly, A. Mosig, A. Tannapfel, C. Kötting, and K. Gerwert, "Spectral histopathology of colon cancer tissue sections by raman imaging with 532 nm excitation provides label free annotation of lymphocytes, erythrocytes and proliferating nuclei of cancer cells," *Analyst*, vol. 138, no. 14, pp. 4035–4039, 2013.

[44] P. Crow, B. Barrass, C. Kendall, M. Hart-Prieto, M. Wright, R. Persad, and N. Stone, "The use of raman spectroscopy to differentiate between different prostatic adenocarcinoma cell lines," *British journal of cancer*, vol. 92, no. 12, p. 2166, 2005.

[45] M. C. Potcoava, G. L. Futia, J. Aughenbaugh, I. R. Schlaepfer, and E. A. Gibson, "Raman and coherent anti-stokes raman scattering microscopy studies of changes in lipid content and composition in hormone-treated breast and prostate cancer cells," *Journal of Biomedical Optics*, vol. 19, no. 11, p. 111605, 2014.

[46] B. Schrader, S. Keller, T. Löchte, S. Fendel, D. Moore, A. Simon, and J. Sawatzki, "Nir ft raman spectroscopy in medical diagnosis," *Journal of molecular structure*, vol. 348, pp. 293–296, 1995.

[47] J. S. Horoszewicz, S. S. Leong, E. Kawinski, J. P. Karr, H. Rosenthal, T. M. Chu, E. A. Mirand, and G. P. Murphy, "Lncap model of human prostatic carcinoma," *Cancer research*, vol. 43, no. 4, pp. 1809–1818, 1983.

[48] W. Hu, C. Peng, W. Luo, M. Lv, X. Li, D. Li, Q. Huang, and C. Fan, "Graphene-based antibacterial paper," *ACS nano*, vol. 4, no. 7, pp. 4317–4323, 2010.

[49] O. Akhavan and E. Ghaderi, "Toxicity of graphene and graphene oxide nanowalls against bacteria," *ACS nano*, vol. 4, no. 10, pp. 5731–5736, 2010.

[50] Y. Zhang, S. F. Ali, E. Dervishi, Y. Xu, Z. Li, D. Casciano, and A. S. Biris, "Cytotoxicity effects of graphene and single-wall carbon nanotubes in neural phaeochromocytoma-derived pc12 cells," *ACS nano*, vol. 4, no. 6, pp. 3181–3186, 2010.

[51] W. Xu, X. Ling, J. Xiao, M. S. Dresselhaus, J. Kong, H. Xu, Z. Liu, and J. Zhang, "Surface enhanced raman spectroscopy on a flat graphene surface," *Proceedings of the National Academy of Sciences*, vol. 109, no. 24, pp. 9281–9286, 2012.

[52] A. Silver, H. Kitadai, H. Liu, T. Granzier-Nakajima, M. Terrones, X. Ling, and S. Huang, "Chemical and bio sensing using graphene-enhanced raman spectroscopy," *Nanomaterials*, vol. 9, no. 4, p. 516, 2019.

[53] M. Kalbacova, A. Broz, J. Kong, and M. Kalbac, "Graphene substrates promote adherence of human osteoblasts and mesenchymal stromal cells," *Carbon*, vol. 48, no. 15, pp. 4323–4329, 2010.

[54] C. V. Raman, "A new radiation," 1928.

[55] N. Colthup, *Introduction to infrared and Raman spectroscopy.* Elsevier, 2012.

[56] H. J. Bowley, D. L. Gerrard, J. D. Louden, and G. Turrell, *Practical raman spectroscopy.* Springer Science & Business Media, 2012.

[57] E. G. Brame and J. G. Grasselli, *Infrared and Raman spectroscopy.* Marcel Dekker, 1976.

[58] Horiba, "Xplora plus confocal raman spectrometer." `https://www.horiba.com/en_en/products/detail/action/show/Product/xploratm-plus-1528/`. [Online; accessed 31/03/2020].

[59] Horiba, "Labspec 6 spectroscopy suite software." `https://www.horiba.com/en_en/products/detail/action/show/Product/labspec-6-spectroscopy-suite-software-1843/`. [Online; accessed 31/03/2020].

[60] X. Li, W. Cai, J. An, S. Kim, J. Nah, D. Yang, R. Piner, A. Velamakanni, I. Jung, E. Tutuc, *et al.*, "Large-area synthesis of high-quality and uniform graphene films on copper foils," *science*, vol. 324, no. 5932, pp. 1312–1314, 2009.

[61] C. Kershaw, "Raman spectroscopy studies of prostate cancer and streptomyces bacteria." `http://etheses.whiterose.ac.uk/17906/`, 2017.

[62] Sigma-Aldrich, Inc., "Stemline keratinocyte medium ii." `https://www.sigmaaldrich.com/content/dam/sigma-aldrich/docs/Sigma/Datasheet/2/k3136dat.pdf`. [Online; accessed 24/12/2019].

[63] J. Filik and N. Stone, "Drop coating deposition raman spectroscopy of protein mixtures," *Analyst*, vol. 132, no. 6, pp. 544–550, 2007.

[64] J.-U. Lee, D. Yoon, H. Kim, S. W. Lee, and H. Cheong, "Thermal conductivity of suspended pristine graphene measured by raman spectroscopy," *Physical Review B*, vol. 83, no. 8, p. 081419, 2011.

[65] Z. Tu, Z. Liu, Y. Li, F. Yang, L. Zhang, Z. Zhao, C. Xu, S. Wu, H. Liu, H. Yang, *et al.*, "Controllable growth of 1–7 layers of graphene by chemical vapour deposition," *Carbon*, vol. 73, pp. 252–258, 2014.

[66] M. Kalbac, A. Reina-Cecco, H. Farhat, J. Kong, L. Kavan, and M. S. Dresselhaus, "The influence of strong electron and hole doping on the raman intensity of chemical vapor-deposition graphene," *Acs Nano*, vol. 4, no. 10, pp. 6055–6063, 2010.

[67] D. Boyd, W.-H. Lin, C.-C. Hsu, M. Teague, C.-C. Chen, Y.-Y. Lo, W.-Y. Chan, W.-B. Su, T.-C. Cheng, C.-S. Chang, *et al.*, "Single-step deposition of high-mobility graphene at reduced temperatures," *Nature communications*, vol. 6, p. 6620, 2015.

[68] S. Zhao, S. P. Surwade, Z. Li, and H. Liu, "Photochemical oxidation of cvd-grown single layer graphene," *Nanotechnology*, vol. 23, no. 35, p. 355703, 2012.

[69] V.-m. Liu, C.-w. Huang, B.-J. Lin, H.-Y. Lin, C.-H. Huang, F.-Y. Shih, W.-H. Wang, C.-Y. Liu, and H.-C. Chui, "Probing substrate influence on graphene by fitting raman signals with voigt profile," in *Technical Digest of the Eighteenth Microoptics Conference*, pp. 1–2, IEEE, 2013.

[70] H. Bukowska, F. Meinerzhagen, S. Akcöltekin, O. Ochedowski, M. Neubert, V. Buck, and M. Schleberger, "Raman spectra of graphene exfoliated on insulating crystalline substrates," *New Journal of Physics*, vol. 13, no. 6, p. 063018, 2011.

[71] I. Childres, L. A. Jauregui, W. Park, H. Cao, and Y. P. Chen, "Raman spectroscopy of graphene and related materials," *New developments in photon and materials research*, vol. 1, 2013.

[72] C. Stampfer, F. Molitor, D. Graf, K. Ensslin, A. Jungen, C. Hierold, and L. Wirtz, "Raman imaging of doping domains in graphene on si o 2," *Applied Physics Letters*, vol. 91, no. 24, p. 241907, 2007.

[73] Z. Huang, H. Lui, M. X. Chen, A. Alajlan, D. I. McLean, and H. Zeng, "Raman spectroscopy of in vivo cutaneous melanin," *Journal of biomedical optics*, vol. 9, no. 6, pp. 1198–1206, 2004.

[74] S. Singh and C. M. Krishna, "Raman spectroscopic studies of oral cancers: correlation of spectral and biochemical markers," *Analytical Methods*, vol. 6, no. 21, pp. 8613–8620, 2014.

[75] S. Kaminaka, T. Ito, H. Yamazaki, E. Kohda, and H.-o. Hamaguchi, "Near-infrared multichannel raman spectroscopy toward real-time in vivo cancer diagnosis," *Journal of Raman Spectroscopy*, vol. 33, no. 7, pp. 498–502, 2002.

[76] Z. Movasaghi, S. Rehman, and I. U. Rehman, "Raman spectroscopy of biological tissues," *Applied Spectroscopy Reviews*, vol. 42, no. 5, pp. 493–541, 2007.

[77] C. Krafft, L. Neudert, T. Simat, and R. Salzer, "Near infrared raman spectra of human brain lipids," *Spectrochimica Acta Part A: Molecular and Biomolecular Spectroscopy*, vol. 61, no. 7, pp. 1529–1535, 2005.

[78] S. Farquharson, C. Shende, F. E. Inscore, P. Maksymiuk, and A. Gift, "Analysis of 5-fluorouracil in saliva using surface-enhanced raman spectroscopy," *Journal of Raman Spectroscopy: An International Journal for Original Work in all Aspects of Raman Spectroscopy, Including Higher Order Processes, and also Brillouin and Rayleigh Scattering*, vol. 36, no. 3, pp. 208–212, 2005.

[79] N. Stone, C. Kendall, J. Smith, P. Crow, and H. Barr, "Raman spectroscopy for identification of epithelial cancers," *Faraday discussions*, vol. 126, pp. 141–157, 2004.

[80] M. Gniadecka, H. Wulf, N. Nymark Mortensen, O. Faurskov Nielsen, and D. H. Christensen, "Diagnosis of basal cell carcinoma by raman spectroscopy," *Journal of Raman spectroscopy*, vol. 28, no. 2-3, pp. 125–129, 1997.

[81] W.-T. Cheng, M.-T. Liu, H.-N. Liu, and S.-Y. Lin, "Micro-raman spectroscopy used to identify and grade human skin pilomatrixoma," *Microscopy research and technique*, vol. 68, no. 2, pp. 75–79, 2005.

[82] R. Malini, K. Venkatakrishna, J. Kurien, K. M. Pai, L. Rao, V. Kartha, and C. M. Krishna, "Discrimination of normal, inflammatory, premalignant, and malignant oral tissue: a raman spectroscopy study," *Biopolymers: Original Research on Biomolecules*, vol. 81, no. 3, pp. 179–193, 2006.

[83] J. W. Chan, D. S. Taylor, T. Zwerdling, S. M. Lane, K. Ihara, and T. Huser, "Micro-raman spectroscopy detects individual neoplastic and normal hematopoietic cells," *Biophysical journal*, vol. 90, no. 2, pp. 648–656, 2006.

[84] G. Shetty, C. Kendall, N. Shepherd, N. Stone, and H. Barr, "Raman spectroscopy: elucidation of biochemical changes in carcinogenesis of oesophagus," *British journal of cancer*, vol. 94, no. 10, pp. 1460–1464, 2006.

[85] G. I. Dovbeshko, N. Y. Gridina, E. B. Kruglova, and O. P. Pashchuk, "Ftir spectroscopy studies of nucleic acid damage," *Talanta*, vol. 53, no. 1, pp. 233–246, 2000.

[86] P. G. Andrus and R. D. Strickland, "Cancer grading by fourier transform infrared spectroscopy," *Biospectroscopy*, vol. 4, no. 1, pp. 37–46, 1998.

[87] I. ur Rehman, Z. Movasaghi, and S. Rehman, *Vibrational spectroscopy for tissue analysis.* CRC Press, 2012.

[88] R. J. Lakshmi, V. Kartha, C. Murali Krishna, J. R. Solomon, G. Ullas, and P. Uma Devi, "Tissue raman spectroscopy for the study of radiation damage: brain irradiation of mice," *Radiation research*, vol. 157, no. 2, pp. 175–182, 2002.

[89] Z. Huang, A. McWilliams, H. Lui, D. I. McLean, S. Lam, and H. Zeng, "Near-infrared raman spectroscopy for optical diagnosis of lung cancer," *International journal of cancer*, vol. 107, no. 6, pp. 1047–1052, 2003.

[90] I. Notingher, C. Green, C. Dyer, E. Perkins, N. Hopkins, C. Lindsay, and L. L. Hench, "Discrimination between ricin and sulphur mustard toxicity in vitro using raman spectroscopy," *Journal of the Royal Society Interface*, vol. 1, no. 1, pp. 79–90, 2004.

[91] S. Koljenović, T. B. Schut, A. Vincent, J. M. Kros, and G. J. Puppels, "Detection of meningioma in dura mater by raman spectroscopy," *Analytical chemistry*, vol. 77, no. 24, pp. 7958–7965, 2005.

[92] C. Ortiz, D. Zhang, Y. Xie, A. E. Ribbe, and D. Ben-Amotz, "Validation of the drop coating deposition raman method for protein analysis," *Analytical biochemistry*, vol. 353, no. 2, pp. 157–166, 2006.

[93] K. Kachrimanis, D. E. Braun, and U. J. Griesser, "Quantitative analysis of paracetamol polymorphs in powder mixtures by ft-raman spectroscopy and pls regression," *Journal of pharmaceutical and biomedical analysis*, vol. 43, no. 2, pp. 407–412, 2007.

[94] M. Munz, C. E. Giusca, R. L. Myers-Ward, D. K. Gaskill, and O. Kazakova, "Thickness-dependent hydrophobicity of epitaxial graphene," *Acs Nano*, vol. 9, no. 8, pp. 8401–8411, 2015.

[95] R. Sato-Berru, E. Mejía-Uriarte, C. Frausto-Reyes, M. Villagrán-Muniz, J. Saniger, *et al.*, "Application of principal component analysis and raman spectroscopy in the analysis of polycrystalline batio3 at high pressure," *Spectrochimica Acta Part A: Molecular and Biomolecular Spectroscopy*, vol. 66, no. 3, pp. 557–560, 2007.

ACKNOWLEDGMENTS

I would firstly like to thank my supervisor Dr Y. Hancock for her support throughout this year and for allowing me to be part of such an interesting project and an amazing research group. She has helped me to progress and gain skills into becoming the scientist I have always hoped of being, whilst providing constant encouragement and discussion on my project.

I would also like to thank my group in the Cancer Research Unit in the Biology Department here at York, especially Dr. Fiona Frame for her help and patience in the culturing of my cells through my projects.

I would also like to thank my research group, especially Jennifer Ferguson and Marcus Cameron for their help during my time here at York, and the wider physics community of research students in the department, who have helped me to settle into a new place and welcomed me.

A big appreciation needs to be mentioned to all my friends, whom are all over World doing amazing things, but continue constantly to support me and keep me on track - many of them have helped me through my time here despite the distance and I treasure all of them for taking time out of their busy schedules to check in with a phone call.

I would like to also give a massive thank you to my family, who will never understand the appreciation I have for their constant encouragement and support throughout my time in University, whether its a brief visit for a Sunday roast or driving up to help me move house, I treasure their constant guidance.

Lastly, I would like to dedicate this thesis to family members who I have lost to his disease. Unfortunately during my write-up, I received the bad news that my grandad is living with prostate cancer. However, it gives me comfort knowing that I am contributing to the research in this field to help thousands of men like him, to achieve a way in which to live longer and healthier lives through earlier diagnosis. Although this paper may be a raindrop in an ocean that is the fight against one of the deadliest diseases to face current medicine, I am proud to be part of the wave of research hoping to help in this battle to a lower mortality rate or the possibility of a cure for cancer and I could not have achieved this without the support system around me, which I am very grateful for.

Appendices
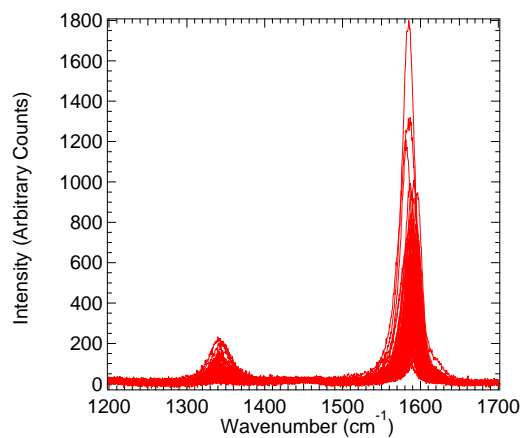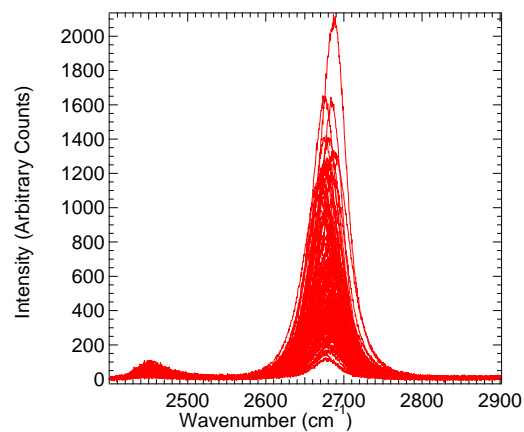
(a) All 120 Graphene Spectra Data for Sample 2.   (b) All 120 Graphene Spectra Data for Sample 2.
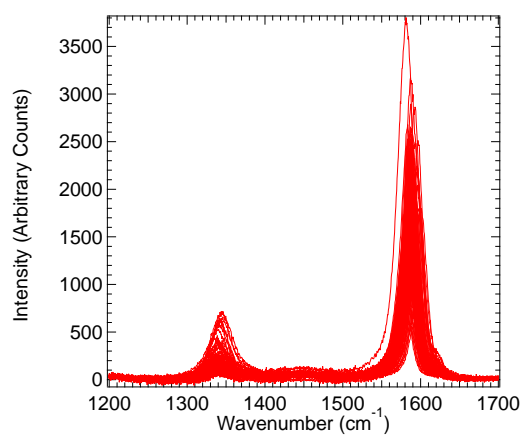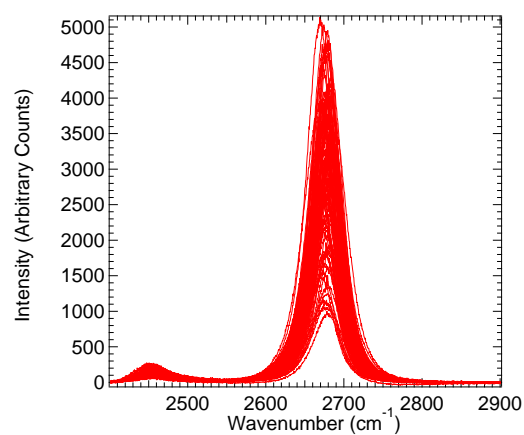
(c) All 111 Graphene Spectra Data for Sample 4.   (d) All 111 Graphene Spectra Data for Sample 4.

Figure 43: A figure to show all spectra taken across random points of each graphene sample at 45s acq. time, 50% filter.
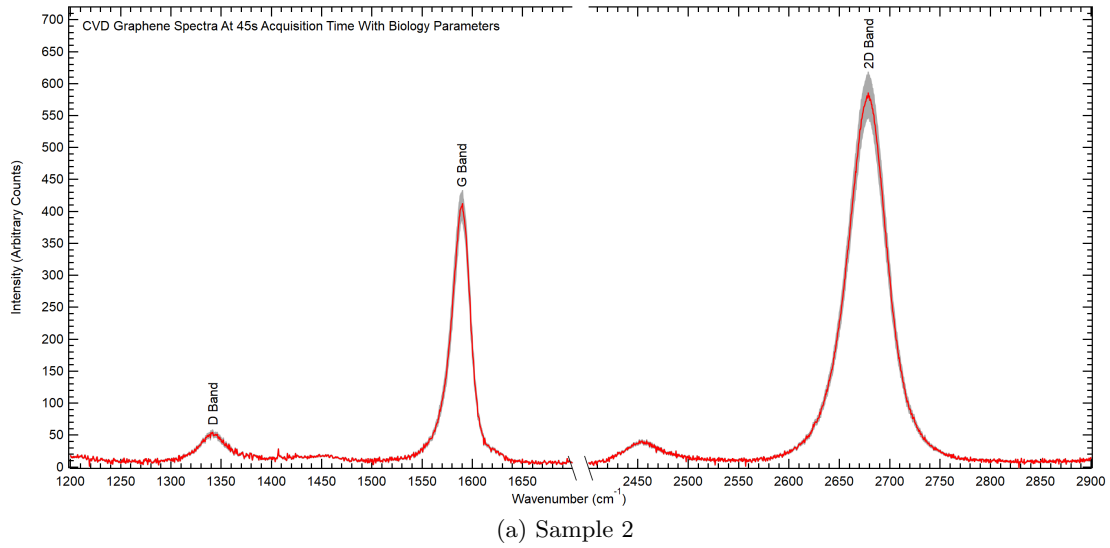
(a) Sample 2

Figure 44: Graph to show intensity in arbitrary counts plotted against wavenumber of the Raman spectra data taken using a 532nm laser to analyse three seperate samples of graphene. 120 data points were chosen at random across each sample. The red line represents the average of 120 spectra taken from each sample. The grey shaded area shows the average spectra with the standard error added or subtracted. All data was baseline subtracted using Raman Tool Set before the average spectra was calculated. These measurements were taken using biology parameters with an acquisition time equal to 45s and a 50% filter.

(a) Sample 2 50% filter, 45s, average
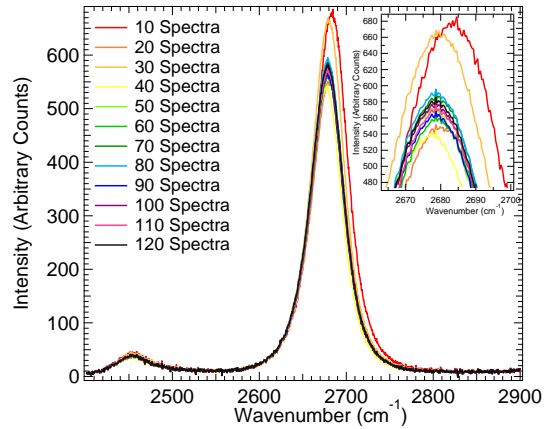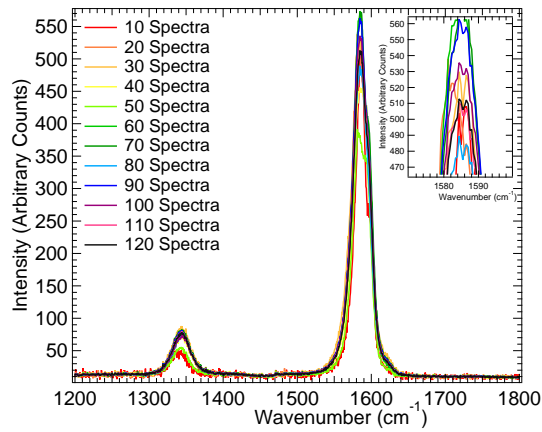
(b) Sample 2 50% filter, 45s, average

(c) Sample 2 50% filter, 45s, 2nd order sd
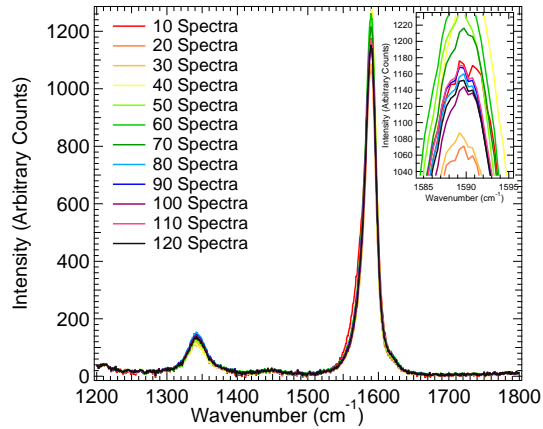
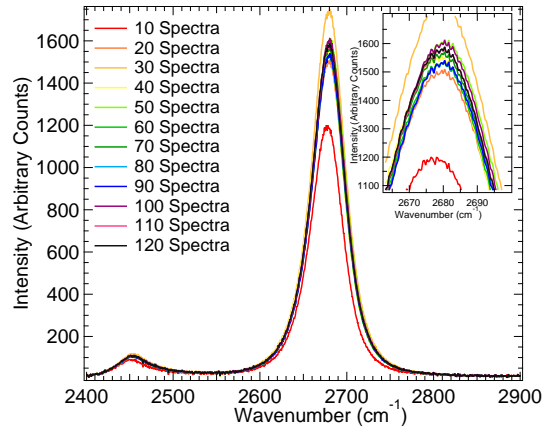(d) Sample 2 50% filter, 45s, 2nd order sd

(e) Sample 2 50% filter, 45s, se

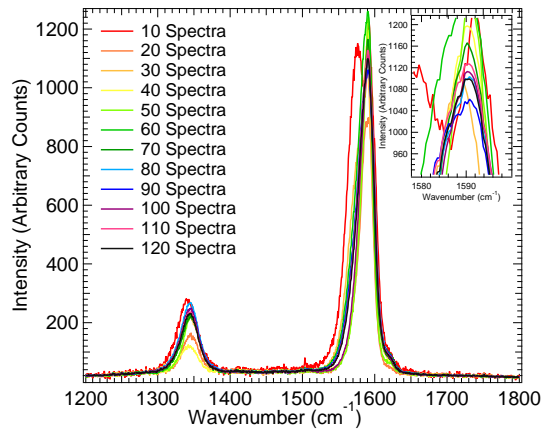(f) Sample 2 50% filter, 45s, se

Figure 45: A figure to show the convergence tests calculated for sample 2 at 50% filter, 45s acq. time.
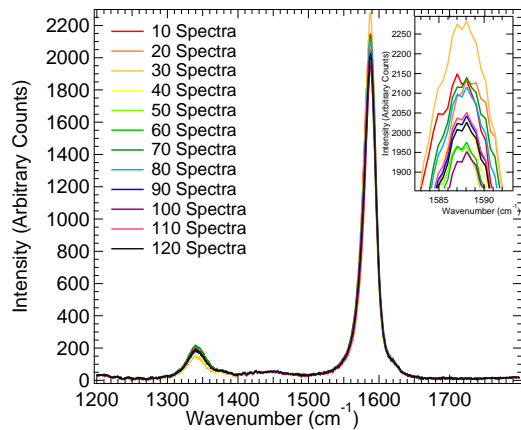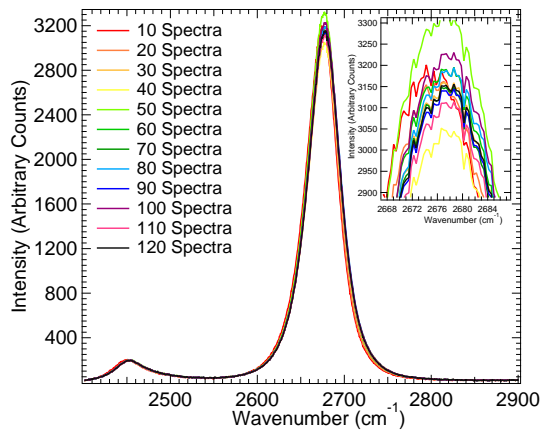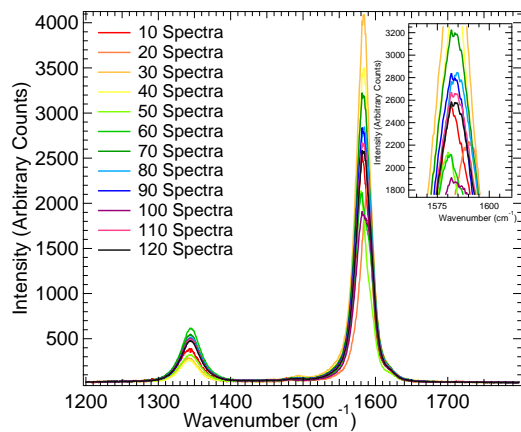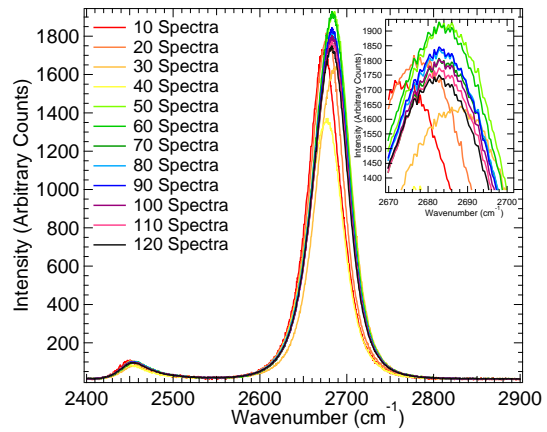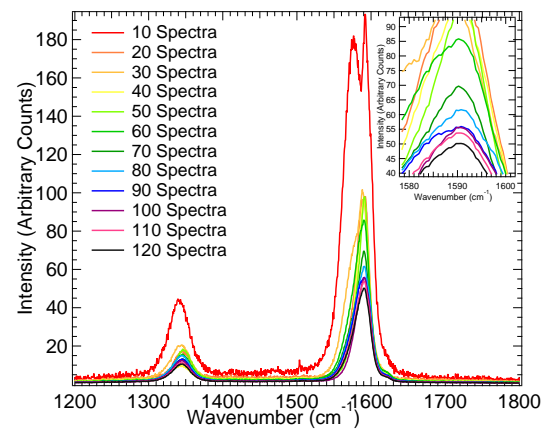
(a) Sample 3 50% filter, 45s, average

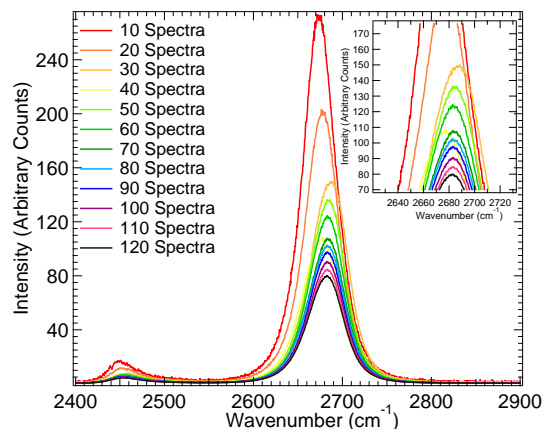(b) Sample 3 50% filter, 45s, average

(c) Sample 3 50% filter, 45s, 2nd order sd
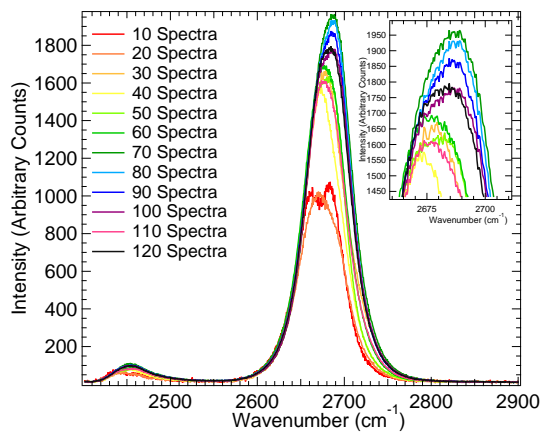
(d) Sample 3 50% filter, 45s, 2nd order sd
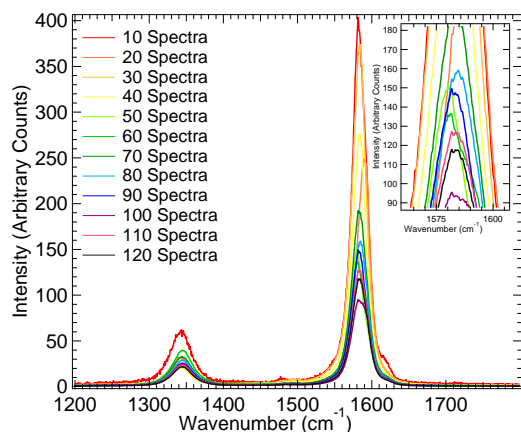
(e) Sample 3 50% filter, 45s, se
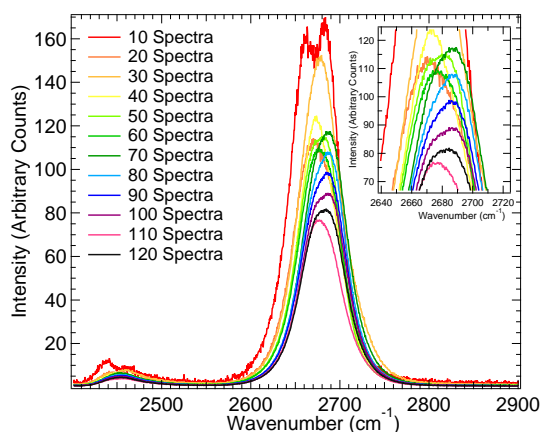
(f) Sample 3 50% filter, 45s, se

Figure 46: A figure to show the convergence tests calculated for sample 3 at 50% filter, 45s acq. time.
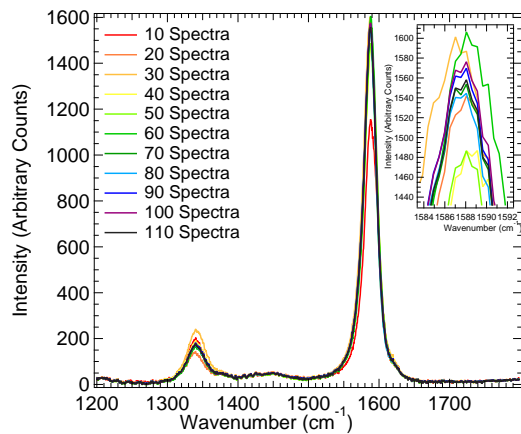
(a) Sample 4 50% filter, 45s, average
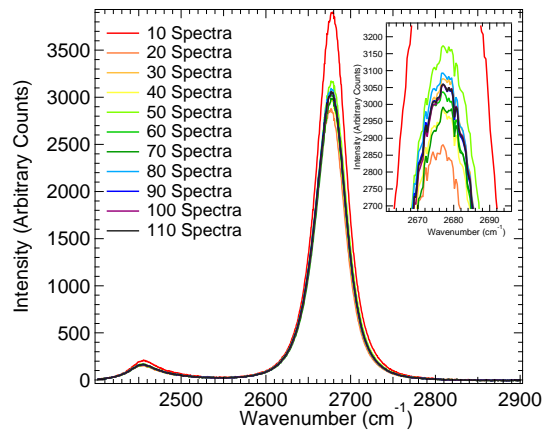
(b) Sample 4 50% filter, 45s, average
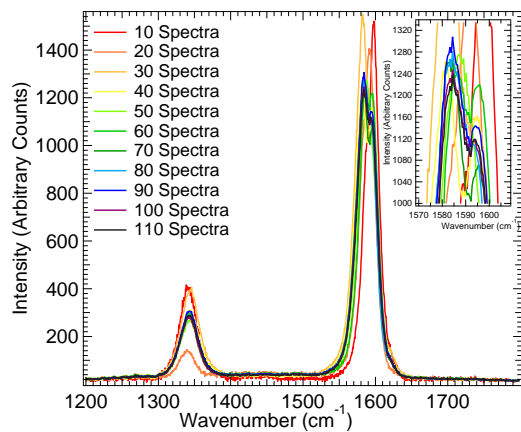
(c) Sample 4 50% filter, 45s, 2nd order sd
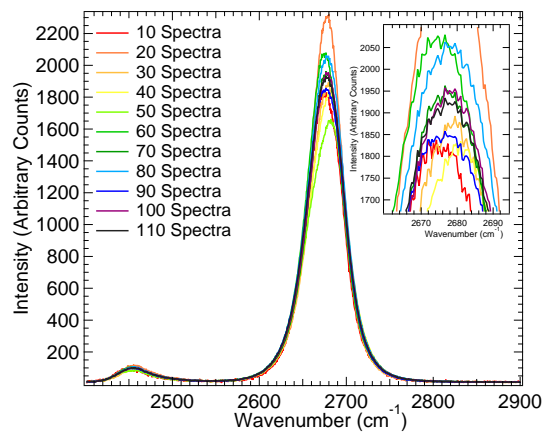
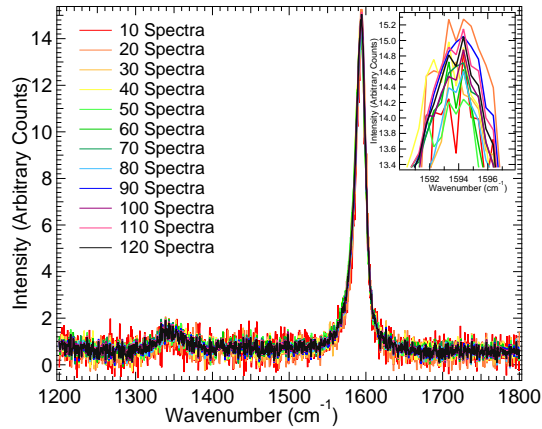(d) Sample 4 50% filter, 45s, 2nd order sd
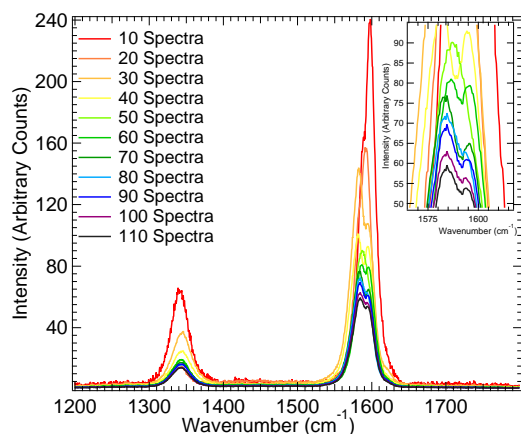
(e) Sample 4 50% filter, 45s, se
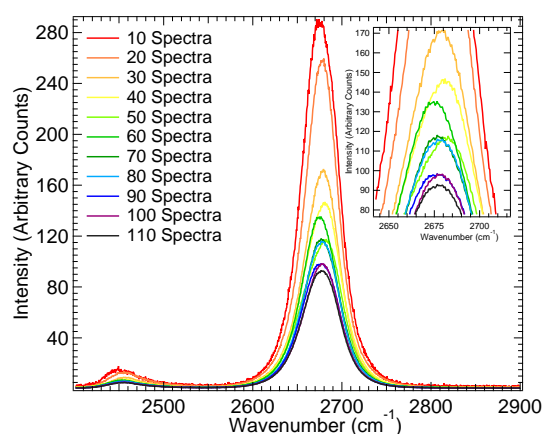
(f) Sample 4 50% filter, 45s, se

Figure 47: A figure to show the convergence tests calculated for sample 4 at 50% filter, 45s acq. time.
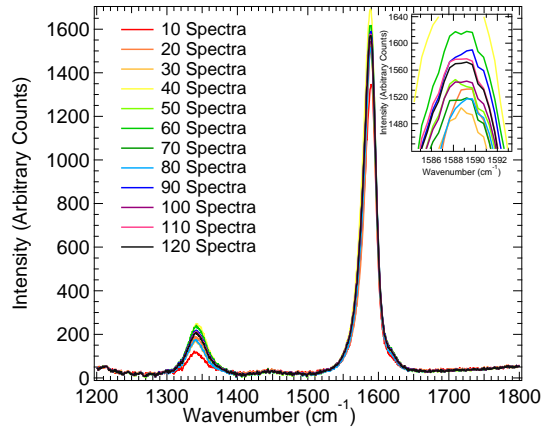
(a) Sample 2 50% filter, 90s, average
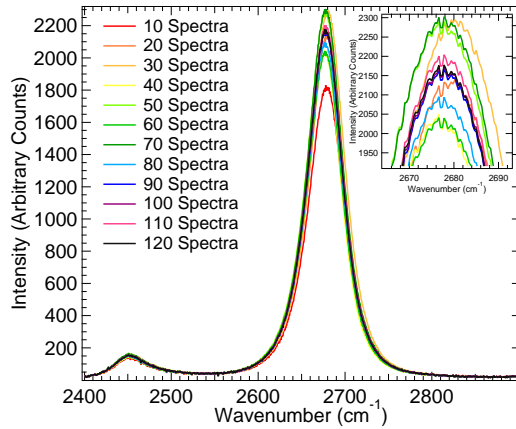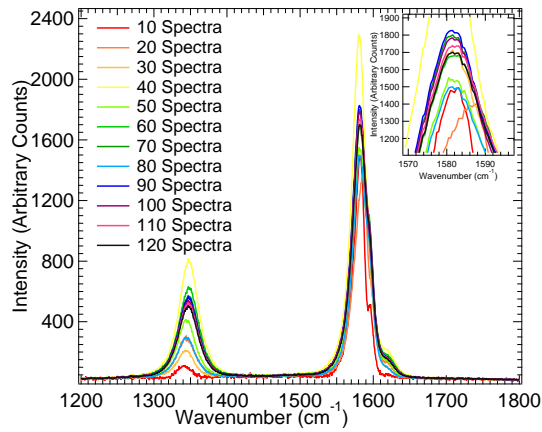
(b) Sample 2 50% filter, 90s, average

(c) Sample 2 50% filter, 90s, 2nd order sd
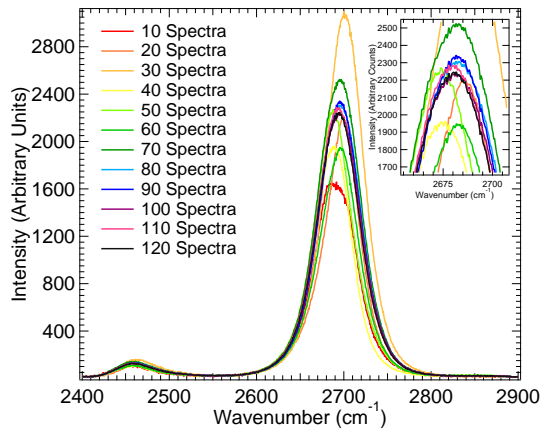
(d) Sample 2 50% filter, 90s, 2nd order sd
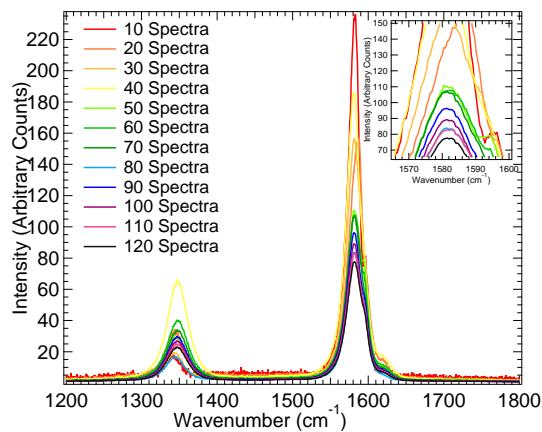
(e) Sample 2 50% filter, 90s, se
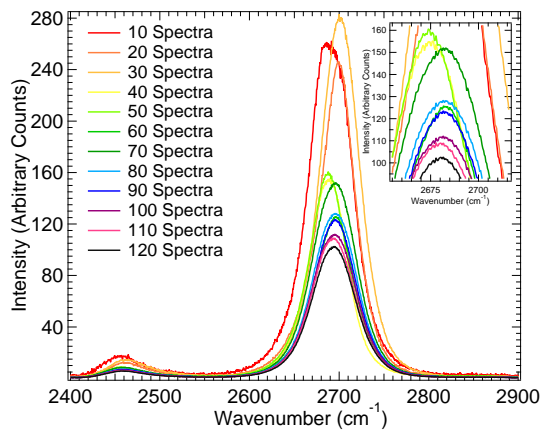
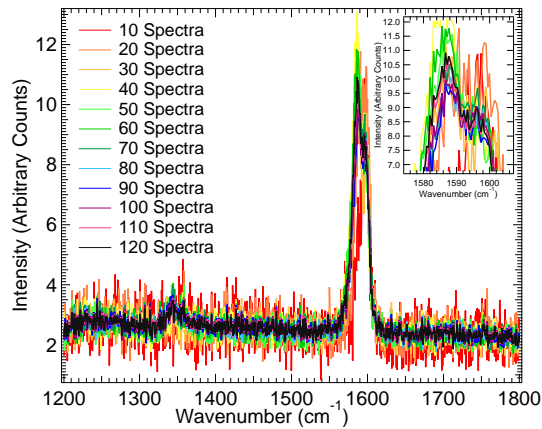(f) Sample 2 50% filter, 90s, se

Figure 48: A figure to show the convergence tests calculated for sample 2 at 50% filter, 90s acq. time.
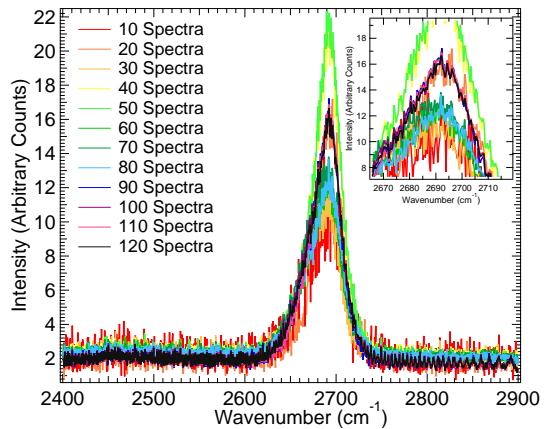
(a) Sample 3 50% filter, 90s, average

(b) Sample 3 50% filter, 90s, average

(c) Sample 3 50% filter, 90s, 2nd order sd

(d) Sample 3 50% filter, 90s, 2nd order sd

(e) Sample 3 50% filter, 90s, se

(f) Sample 3 50% filter, 90s, se

Figure 49: A figure to show the convergence tests calculated for sample 3 at 50% filter, 90s acq. time.
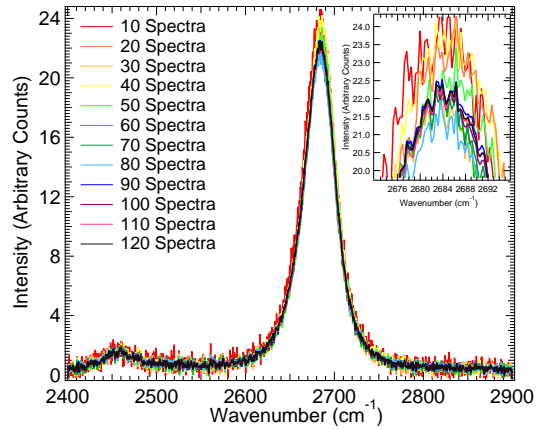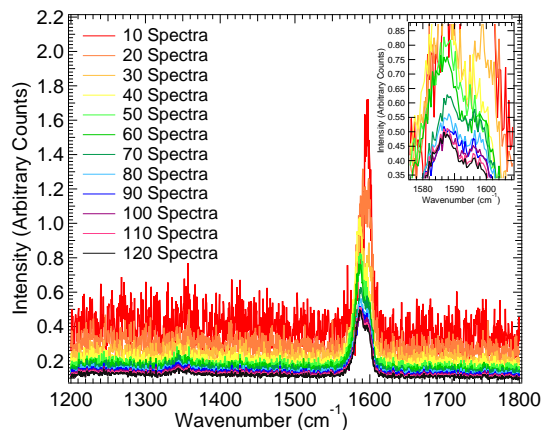
(a) Sample 1 10% filter, 2s, average
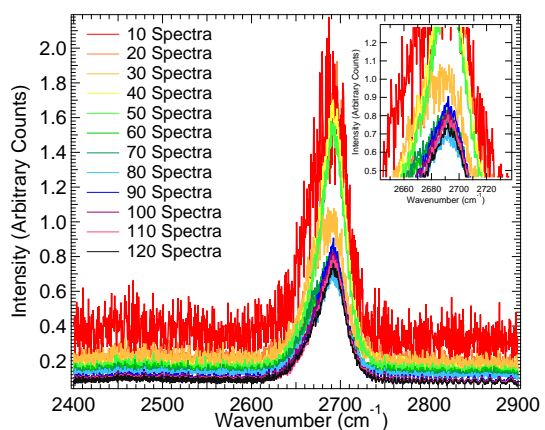(b) Sample 1 10% filter, 2s, average

(c) Sample 1 10% filter, 2s, 2nd order sd
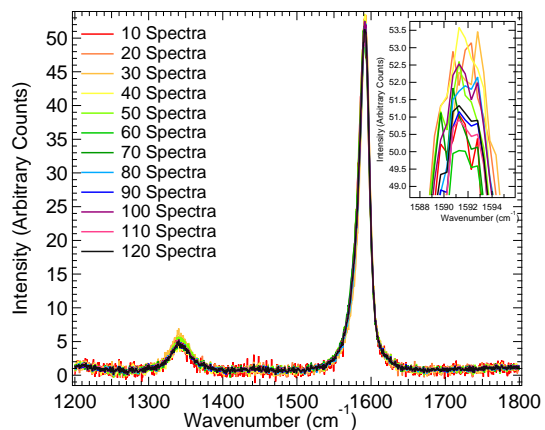(d) Sample 1 10% filter, 2s, 2nd order sd
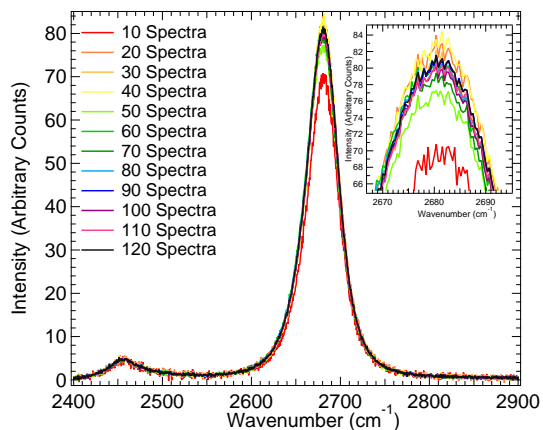
(e) Sample 1 10% filter, 2s, se
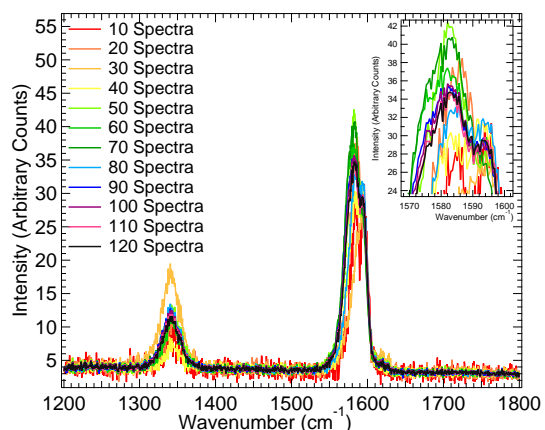(f) Sample 1 10% filter, 2s, se

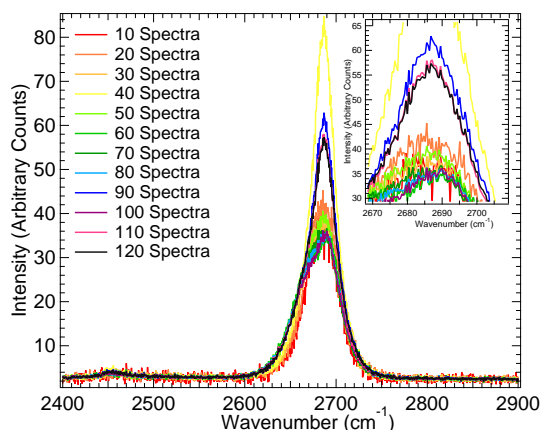Figure 50: A figure to show the convergence tests calculated for sample 1 at 10% filter.

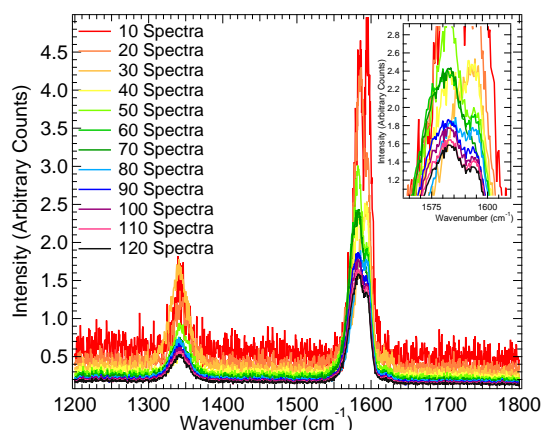(a) Sample 1 25% filter, 2s, average

(b) Sample 1 25% filter, 2s, average

(c) Sample 1 25% filter, 2s, 2nd order sd

(d) Sample 1 25% filter, 2s, 2nd order sd

(e) Sample 1 25% filter, 2s, se

(f) Sample 1 25% filter, 2s, se

Figure 51: A figure to show the convergence tests calculated for sample 1 at 25% filter.

(a) Sample 1 50% filter, 90s, average
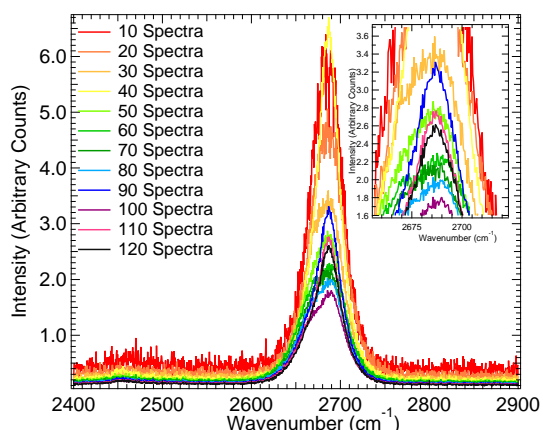
(b) Sample 1 50% filter, 90s, average

(c) Sample 1 50% filter, 90s, 2nd order sd
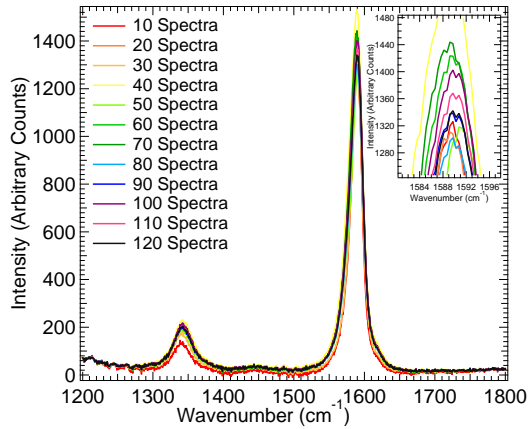
(d) Sample 1 50% filter, 90s, 2nd order sd
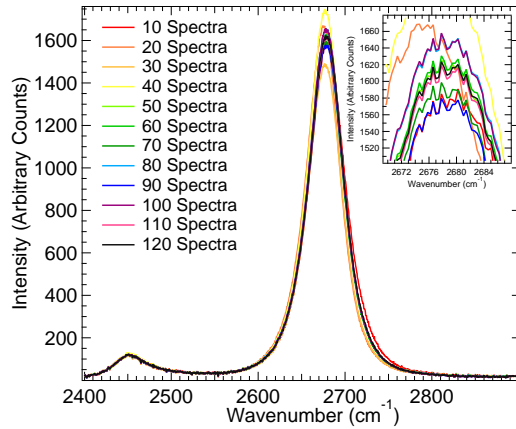
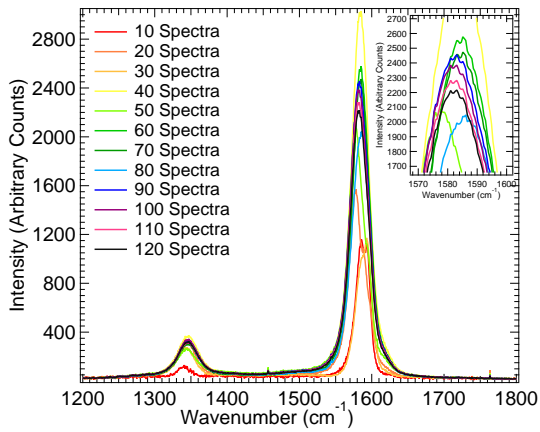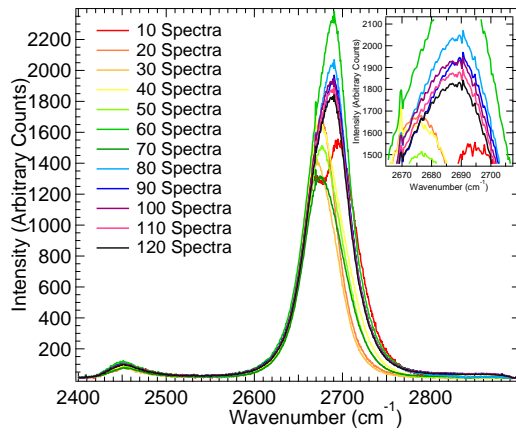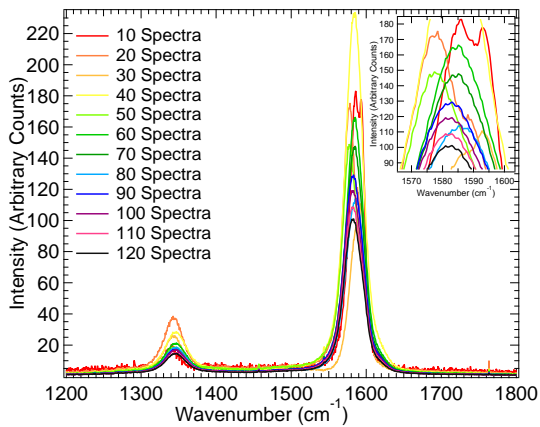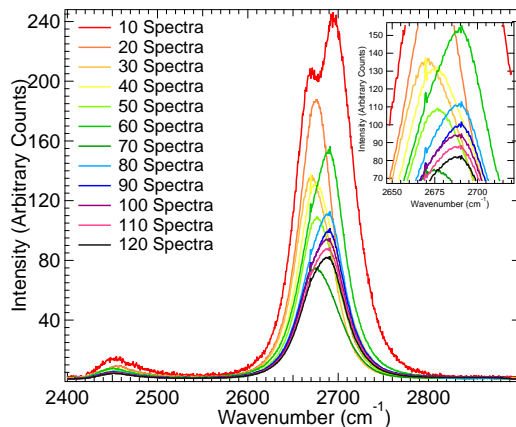(e) Sample 1 50% filter, 90s, se

(f) Sample 1 50% filter, 90s, se

Figure 52: A figure to show the convergence tests calculated for sample 1 at 50% filter, 90s acq. time.

Results for Sample 2 for 50% filter, 45s acquisition time.				
Band	Location, cm^{-1}	Calculated Standard Error in Location, cm^{-1}	Full Width at Half Maximum (FWHM), cm^{-1}	Calculated Standard Error in FWHM, cm^{-1}
D Band	1341.5	±0.2	28.8	±1.6
G Band	1592.6	±0.1	13.1	±0.1
G' Band	2677.9	±0.1	45.0	±0.3

Table 9: Table to show the location, FWHM of each band in graphene sample 2, along with their representative calculated standard errors. These values were calculated by fitting peaks to the data shown. These are the results for the biology parameters where acquisition time is equal to 45s with a 50% filter. Note that there is an instrumental error within the location and FWHM of ±3cm^{-1}.

Results for Sample 3 for 50% filter, 45s acquisition time.				
Band	Location, cm^{-1}	Calculated Standard Error in Location, cm^{-1}	Full Width at Half Maximum (FWHM), cm^{-1}	Calculated Standard Error in FWHM, cm^{-1}
D Band	1341.1	±0.4	30.8	±0.5
G Band	1589.6	±0.0	14.1	±0.2
G' Band	2676.8	±0.1	44.2	±0.4

Table 10: Table to show the location, FWHM of each band in graphene sample 3, along with their representative calculated standard errors. These values were calculated by fitting peaks to the data shown. These are the results for the biology parameters where acquisition time is equal to 45s with a 50% filter. Note that there is an instrumental error within the location and FWHM of ±3cm^{-1}.

Results for Sample 4 for 50% filter, 45s acquisition time.				
Band	Location, cm^{-1}	Calculated Standard Error in Location, cm^{-1}	Full Width at Half Maximum (FWHM), cm^{-1}	Calculated Standard Error in FWHM, cm^{-1}
D Band	1340.4	±0.2	28.9	±1.0
G Band	1590.6	±0.4	15.4	±0.2
G' Band	2676.5	±0.0	42.5	±0.2

Table 11: Table to show the location, FWHM of each band in graphene sample 4, along with their representative calculated standard errors. These values were calculated by fitting peaks to the data shown. These are the results for the biology parameters where acquisition time is equal to 45s with a 50% filter. Note that there is an instrumental error within the location and FWHM of ±3cm^{-1}, with only 111 spectra.

Results for Sample 2 for 50% filter, 90s acquisition time.				
Band	Location, cm^{-1}	Calculated Standard Error in Location, cm^{-1}	Full Width at Half Maximum (FWHM), cm^{-1}	Calculated Standard Error in FWHM, cm^{-1}
D Band	1342.4	±0.6	30.4	±1.0
G Band	1590.6	±0.0	13.6	±0.2
G' Band	2690.6	±0.2	47.2	±0.5

Table 12: Table to show the location, FWHM of each band in graphene sample 2, along with their representative calculated standard errors. These values were calculated by fitting peaks to the data shown. These are the results for the biology parameters where acquisition time is equal to 90s with a 50% filter. Note that there is an instrumental error within the location and FWHM of ±3cm^{-1}.

Results for Sample 3 for 50% filter, 90s acquisition time.				
Band	Location, cm^{-1}	Calculated Standard Error in Location, cm^{-1}	Full Width at Half Maximum (FWHM), cm^{-1}	Calculated Standard Error in FWHM, cm^{-1}
D Band	1342.6	±0.1	30.1	±0.6
G Band	1591.2	±0.1	13.1	±0.2
G' Band	2692.2	±0.1	44.6	±0.2

Table 13: Table to show the location, FWHM of each band in graphene sample 3, along with their representative calculated standard errors. These values were calculated by fitting peaks to the data shown. These are the results for the biology parameters where acquisition time is equal to 90s with a 50% filter. Note that there is an instrumental error within the location and FWHM of ±3cm^{-1}.

Results for Sample 1 for 25% filter, 2s acquisition time.				
Band	Location, cm^{-1}	Calculated Standard Error in Location, cm^{-1}	Full Width at Half Maximum (FWHM), cm^{-1}	Calculated Standard Error in FWHM, cm^{-1}
D Band	1342.6	±0.2	31.5	±1.3
G Band	1592.6	±0.1	11.5	±0.2
G' Band	2679.8	±0.2	42.70	±0.05

Table 14: Table to show the location, FWHM of each band in graphene sample 1, along with their representitive calculated standard errors. These values were calculated by fitting peaks to the data shown. These are the results where acquisition time is equal to 2s with a 25% filter. Note that there is an instrumental error within the location and FWHM of ±3cm^{-1}.

Results for Sample 1 for 50% filter, 45s acquisition time.				
Band	Location, cm^{-1}	Calculated Standard Error in Location, cm^{-1}	Full Width at Half Maximum (FWHM), cm^{-1}	Calculated Standard Error in FWHM, cm^{-1}
D Band	1341.9	±0.1	29.8	±0.5
G Band	1592.7	±0.2	13.9	±0.4
G' Band	2679.3	±0.1	45.5	±0.5

Table 15: Table to show the location, FWHM of each band in graphene sample 1, along with their representative calculated standard errors. These values were calculated by fitting peaks to the data shown. These are the results for the biology parameters where acquisition time is equal to 45s with a 50% filter. Note that there is an instrumental error within the location and FWHM of ±3cm^{-1}.

Results for Sample 1 for 50% filter, 90s acquisition time.				
Band	Location, cm^{-1}	Calculated Standard Error in Location, cm^{-1}	Full Width at Half Maximum (FWHM), cm^{-1}	Calculated Standard Error in FWHM, cm^{-1}
D Band	1342.5	±0.3	32.1	±0.4
G Band	1591.6	±0.2	14.2	±0.5
G' Band	2678.3	±0.3	47.5	±0.5

Table 16: Table to show the location, FWHM of each band in graphene sample 1, along with their representative calculated standard errors. These values were calculated by fitting peaks to the data shown. These are the results for the biology parameters where acquisition time is equal to 90s with a 50% filter. Note that there is an instrumental error within the location and FWHM of ±3cm^{-1}.

Results for Sample 1 for 10% filter, 2s acquisition time.				
Band	Location, cm^{-1}	Calculated Standard Error in Location, cm^{-1}	Full Width at Half Maximum (FWHM), cm^{-1}	Calculated Standard Error in FWHM, cm^{-1}
D Band	1345.0	±0.5	34.6	±2.4
G Band	1594.8	±0.1	10.5	±0.1
G' Band	2683.4	±0.2	41.7	±0.2

Table 17: Table to show the location, FWHM of each band in graphene sample 1, along with their representitive calculated standard errors. These values were calculated by fitting peaks to the data shown. These are the results where acquisition time is equal to 2s with a 10% filter. Note that there is an instrumental error within the location and FWHM of ±3cm^{-1}.